

Document Version

Final published version

Citation (APA)

Isaakidou, A. (2026). *Washing away the sile: Cochlear implants for local drug delivery*. [Dissertation (TU Delft), Delft University of Technology]. <https://doi.org/10.4233/uuid:9c7d5871-ae98-4ad5-9db9-ef98982b2e98>

Important note

To cite this publication, please use the final published version (if applicable).
Please check the document version above.

Copyright

In case the licence states "Dutch Copyright Act (Article 25fa)", this publication was made available Green Open Access via the TU Delft Institutional Repository pursuant to Dutch Copyright Act (Article 25fa, the Taverne amendment). This provision does not affect copyright ownership.
Unless copyright is transferred by contract or statute, it remains with the copyright holder.

Sharing and reuse

Other than for strictly personal use, it is not permitted to download, forward or distribute the text or part of it, without the consent of the author(s) and/or copyright holder(s), unless the work is under an open content license such as Creative Commons.

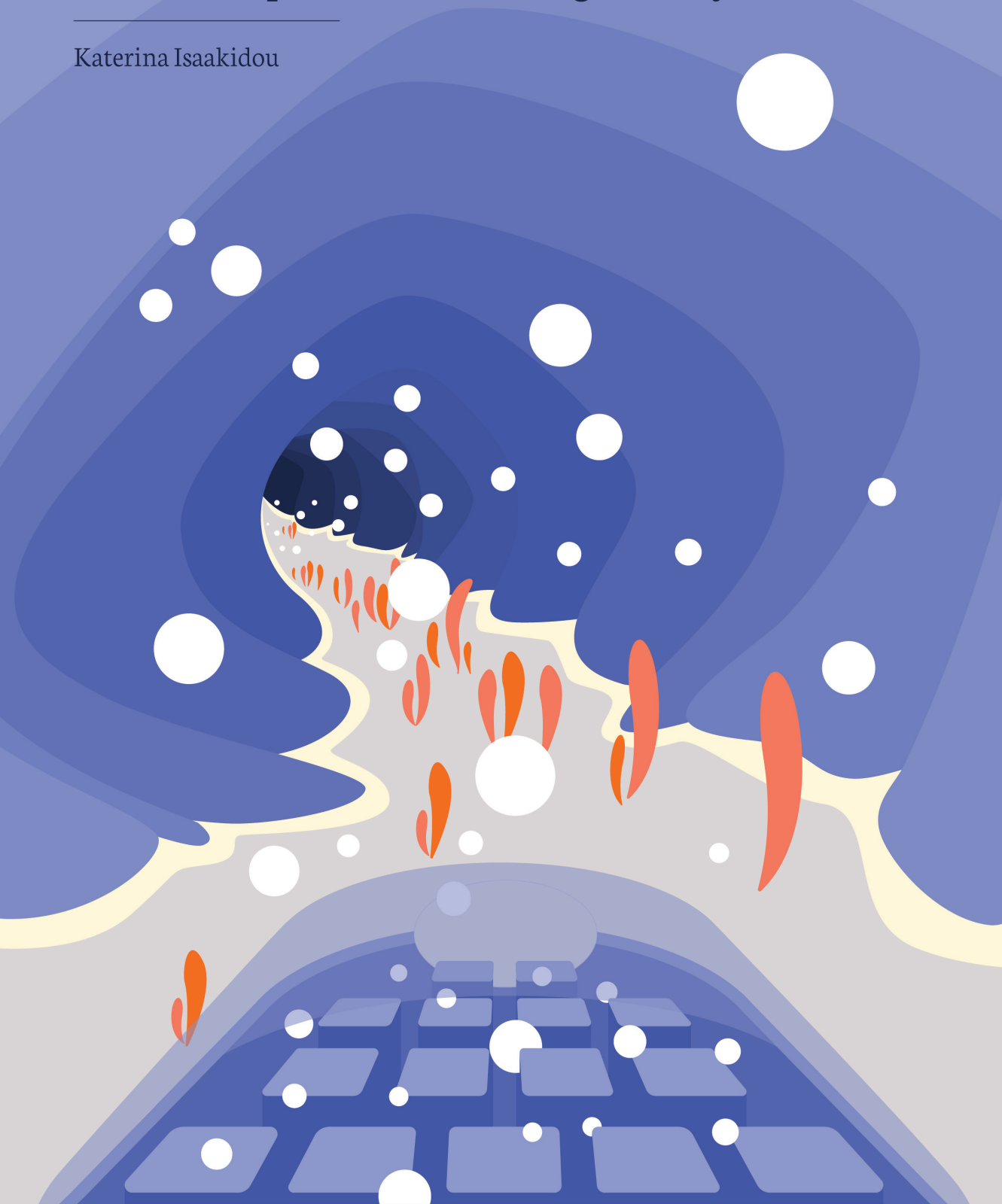
Takedown policy

Please contact us and provide details if you believe this document breaches copyrights.
We will remove access to the work immediately and investigate your claim.

Washing away the silence

Cochlear implants for local drug delivery

Katerina Isaakidou



PROPOSITIONS

accompanying the dissertation

Washing away the silence Cochlear implants for local drug delivery

By

Aikaterini Isaakidou

1. While 2PP enables high-resolution fabrication, discrepancies in component fidelity and mechanical behavior challenge the notion of straightforward scalability. (this thesis)
2. Drug loading into a porous cochlear implant is the only real barrier to delivering a drug to the inner ear. (this thesis)
3. Fine-tuning a laser is easy; predicting its impact on the strength of the printed microstructure is not. (this thesis)
4. The future of hearing restoration lies beyond cochlear implants. (this thesis)
5. The number of authors influences both the duration of the research and the potential bias in its execution.
6. The measure of intelligence is the ability to understand each other.
7. Doing your best should suffice for any job.
8. Ignoring our ignorance is the only way to publish a scientific paper.
9. The human capacity of imagination is superior to the human capacity of implementation.
10. Doctoral degrees should only be awarded to individuals who acknowledge the significance of politics and history.

These propositions are opposable and defensible and have been approved as such by the promotor Prof. dr. A.A. Zadpoor and copromotors Dr. ir. E.L. Fratila-Apachitei and Dr. ir. I. Apachitei.

Washing away the silence

Cochlear implants for local drug delivery

Aikaterini Isaakidou

Washing away the silence

Cochlear implants for local drug delivery

Proefschrift

ter verkrijging van de graad van doctor
aan de Technische Universiteit Delft,
op gezag van de Rector Magnificus, Prof. dr. ir. H. Bijl,
voorzitter van het College voor Promoties,
in het openbaar te verdedigen op
vrijdag, 20 februari 2026 om 10:00 uur.

door

Aikaterini ISAAKIDOU

Master of Science in Biomedical Engineering,
Technische Universiteit Delft, the Netherlands,
geboren te Kavala, Griekenland.

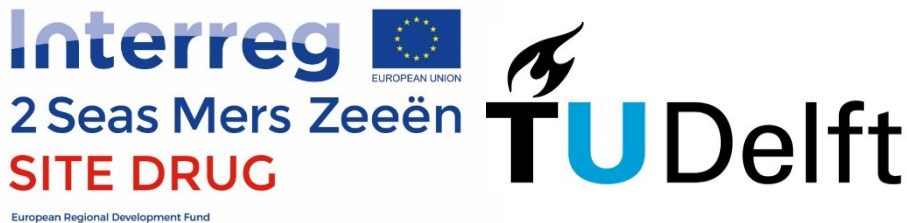
Dit proefschrift is goedgekeurd door de promotor en copromotoren.

Samenstelling promotiecommissie bestaat uit:

Rector magnificus	Voorzitter
Prof.dr. A.A. Zadpoor	Technische Universiteit Delft, promotor
Dr.ir. E.L. Fratila-Apachitei	Technische Universiteit Delft, copromotor
Dr.ir. I. Apachitei	Technische Universiteit Delft, copromotor

Onafhankelijke leden:

Prof.dr. U. Staufer	Technische Universiteit Delft
Prof.dr. ing. F.J.H Gijzen	Technische Universiteit Delft
Prof.dr. A. Basit	University College London
Prof.dr. J.J.C. Arts	Maastricht University Medical Center+, Eindhoven University of Technology
Prof.dr.ir. A.C. Schouten	Technische Universiteit Delft, reserve lid



This project has received funding from the Interreg 2 Seas programme 2014-2020 co-funded by the European Regional Development Fund under subsidy contract “Site Drug 2S07-033”.

Keywords: 3D printing, Cochlear implants, Drug delivery systems

Cover design: The Daydreamer’s Tale | Samantha Aves Martinho

Printed by: Ridderprint | www.ridderprint.nl

Copyright © 2026 by A. Isaakidou

powder
flows
crystallizes
dissolves

disciplined by
the predetermined path

it washes away
the silence

— **Katerina Isaakidou, A machine for hearing**

To my grandparents

Marianthi and Periklis

CONTENTS

SUMMARY	xv
SAMENVATTING	xviii
1. INTRODUCTION	22
1.1. BACKGROUND	22
1.2. DRUG DELIVERY TO THE INNER EAR	22
1.3. FABRICATION OF A COCHLEAR DRUG DELIVERY SYSTEM	23
1.4. MAIN GOAL AND THESIS OUTLINE	24
REFERENCES	26
2. DESIGN & FABRICATION OF COCHLEAR IMPLANTS	30
2.1. INTRODUCTION	31
2.2. MATERIALS AND METHODS	34
2.2.1. IMPLANT DESIGN.....	34
2.2.2. PRELIMINARY STUDY: 3D PRINTING OF TEST STRUCTURES.....	36
2.2.3. 3D PRINTING OF COCHLEAR IMPLANTS.....	38
2.2.4. 3D PRINTING OF SAMPLES FOR IP-Q CHARACTERIZATION.....	39
2.2.5. MORPHOLOGICAL CHARACTERIZATION.....	39
2.2.6. SURFACE TOPOGRAPHY	39
2.2.7. CHEMICAL CHARACTERIZATION	40
2.2.8. WETTABILITY AND SURFACE FREE ENERGY	40
2.2.9. CYTOTOXICITY	41
2.2.10. IMAGE ANALYSIS.....	41
2.2.11. STATISTICAL ANALYSIS.....	42
2.3. RESULTS	42
2.3.1. 3D PRINTING OF PILLAR ARRAYS	42

2.3.2. 3D PRINTING OF CUBIC UNIT CELLS AND HOLLOW CYLINDRICAL STRUCTURES.....	43
2.3.3. 3D PRINTING OF THE COCHLEAR IMPLANTS.....	46
2.3.4. MORPHOLOGICAL CHARACTERIZATION.....	48
2.3.5. SURFACE TOPOGRAPHY.....	48
2.3.6. CHEMICAL CHARACTERIZATION.....	50
2.3.7. WETTABILITY AND SURFACE FREE ENERGY.....	50
2.3.8. CYTOTOXICITY.....	50
2.4. DISCUSSION.....	50
2.4.1. IMPLANT DESIGN AND FABRICATION.....	51
2.4.2. CHARACTERIZATION.....	53
2.4.3. OUTLOOK AND CHALLENGES.....	54
2.5. CONCLUSION.....	55
REFERENCES.....	56
3. MICROMECHANICS AND MANUFACTURABILITY OF 3D PRINTED MICROSTRUCTURES.....	66
3.1. INTRODUCTION.....	67
3.2. MATERIALS AND METHODS.....	70
3.2.1. 2PP PRINTING OF MICROSCALE STRUCTURES USING IP-Q, IP-S, AND IP-PDMS.....	70
3.2.2. 2PP PRINTING OF MICROPILLARS USING IP-Q.....	71
3.2.3. MORPHOLOGICAL CHARACTERIZATION OF MICROSCALE STRUCTURES AND MICROPILLARS.....	72
3.2.4. CHEMICAL CHARACTERIZATION OF IP-Q, IP-S, AND IP-PDMS.....	72
3.2.6. STATISTICAL ANALYSIS.....	74
3.3. RESULTS.....	74

3.3.1. MORPHOLOGICAL CHARACTERIZATION OF MICROSCALE STRUCTURES	74
3.3.2. MORPHOLOGICAL CHARACTERIZATION OF MICROPILLARS	76
3.3.3. CHEMICAL CHARACTERIZATION OF IP-Q, IP-S, AND IP-PDMS	79
3.3.4. MECHANICAL CHARACTERIZATION OF MICROSCALE STRUCTURES AND MICROPILLARS.....	82
3.4. DISCUSSION	85
3.4.1. STIFFNESS RETENTION IN POROUS MICROSCALE STRUCTURES.....	85
3.4.2. THE INFLUENCE OF THE PRINTING PARAMETERS ON THE MORPHOLOGY AND MECHANICAL PROPERTIES OF THE IP-Q MICROPILLARS.....	88
3.4.3. INFLUENCE OF PHYSICAL EXPOSURE PARAMETERS ON POLYMERIZATION, MECHANICS AND SUITABILITY FOR BIOMEDICAL APPLICATIONS.....	89
3.5. CONCLUSION	91
REFERENCES	93
3.6. SUPPORTING INFORMATION	97
3.6.1. STATISTICAL EXPLORATION AND ANALYSIS.....	97
3.6.2. CALCULATION OF THE THEORETICAL (DESIGNED) POROSITY AND RELATIVE DENSITY OF THE MICROSTRUCTURES	97
3.6.3. GEOMETRY (DIAMETER, HEIGHT) OF THE 2PP-PRINTED MICROPILLARS AND CALCULATION OF THE DEVIATION WITH RESPECT TO THE DESIGNED GEOMETRY	98
3.6.4. CHEMICAL COMPOSITION OF IP-Q, IP-S, IP-PDMS.....	98
3.6.5. EXPOSURE CONDITIONS AND CALCULATED PHYSICAL PARAMETERS	
98	
4. MECHANICS OF POROUS COCHLEAR IMPLANTS	110
4.1. INTRODUCTION	111
4.2. MATERIALS AND METHODS	114

4.2.1. FABRICATION OF THE SPECIMENS FOR COMPRESSION TESTING	114
4.2.2. FABRICATION OF ENLARGED 3D PRINTED IMPLANTS FOR TORSION TESTING	115
4.2.3. <i>IN SILICO</i> INVESTIGATION OF TORSION SPECIMENS AND COCHLEAR IMPLANTS.....	118
4.2.4. <i>EX SILICO</i> MECHANICAL CHARACTERIZATION.....	118
4.2.5. FRACTOGRAPHY	120
4.2.6. RAMAN SPECTROSCOPY	121
4.2.7. STATISTICAL ANALYSIS	121
4.3. RESULTS	121
4.3.1. COMPRESSION OF THE IP-Q (2PP) AND GREY RESIN (SLA) PILLARS	121
4.3.2. TORSION TESTING	123
4.3.3. RAMAN SPECTROSCOPY	130
4.4. DISCUSSION	132
4.4.1. EFFECT OF LAYER THICKNESS AND PRINT ORIENTATION ON THE YOUNG'S MODULUS OF GREY RESIN.....	132
4.4.2. FAILURE MODE ANALYSIS OF GREY RESIN.....	133
4.4.3. COMPARATIVE ANALYSIS OF EXPERIMENTAL AND FEA TORSION TESTING RESULTS.....	134
4.4.4. ANALYSIS OF FEA MODELING: GREY RESIN VS. IP-Q.....	136
4.4.5. FEA OF MECHANICAL BEHAVIOR: R VS. C IMPLANT DESIGNS.....	136
4.4.6. POLYMERIZATION OF IP-Q AND GREY RESIN DURING 2PP AND SLA PRINTING	137
4.5. CONCLUSION	138
REFERENCES	140
4.6. SUPPORTING INFORMATION	144
5. COCHLEAR IMPLANT DRUG LOADING AND RELEASE	152

5.1. INTRODUCTION	153
5.2. MATERIALS AND METHODS	154
5.2.1. IMPLANT DESIGN AND FABRICATION	154
5.2.2. PREPARATION OF DRUG-LOADED IMPLANTS	155
5.2.3. IBUPROFEN RELEASE MEASUREMENTS	157
5.2.4. MICRO-COMPUTED TOMOGRAPHY OF THE IMPLANTS	157
5.2.5. THERMAL ANALYSIS OF THE DRUG AND IMPLANTS	158
5.2.6. MACROPHAGE CULTURE WITH IBUPROFEN-RICH MEDIUM	159
5.2.7. STATISTICAL ANALYSIS	160
5.3. RESULTS	160
5.3.1. IBUPROFEN LOADING, CRYSTALLINITY, AND DISTRIBUTION INSIDE THE COCHLEAR IMPLANTS	160
5.3.2. EFFECT OF IMPLANT ARCHITECTURE AND pH ON THE RELEASE OF IBUPROFEN	162
5.3.3. MACROPHAGE VIABILITY AND GENE EXPRESSION PROFILE IN RESPONSE TO IBUPROFEN TREATMENT	163
5.4. DISCUSSION	165
5.4.1. IBUPROFEN LOADING AND RELEASE	165
5.4.2. MACROPHAGE RESPONSE TO THE RELEASED IBUPROFEN	166
5.5. CONCLUSION	168
REFERENCES	170
5.6. SUPPORTING INFORMATION	174
6. CONCLUDING REMARKS	178
6.1 MAIN FINDINGS	178
6.2. GENERAL DISCUSSION	178
6.2.1. TWO-PHOTON POLYMERIZATION	178
6.2.2. MATERIAL PROPERTIES	179

6.2.3. MECHANICAL TESTING CONSTRAINTS	180
6.2.4. DRUG DELIVERY	180
6.2.5. TOWARD A MODULAR COCHLEAR DRUG DELIVERY SYSTEM	181
6.3. FUTURE OUTLOOK	181
6.3.1. COCHLEAR IMPLANT DESIGN AND FABRICATION.....	182
6.3.2. DRUG LOADING AND RELEASE.....	182
6.3.3. BIOLOGICAL STUDIES	183
6.3.4. CLINICAL TRANSLATION	184
CONCLUDING REMARK	184
REFERENCES	185
ACKNOWLEDGEMENTS	187
CURRICULUM VITAE	191
LIST OF PUBLICATIONS	192

SUMMARY

Drug delivery to anatomically complex and physiologically protected regions of the body remains a major challenge in pharmaceutical science. In the inner ear, the blood-labyrinth barrier significantly limits the efficacy of systemically administered drugs. As a result, conditions such as sensorineural hearing loss, Ménière's disease, and tinnitus are often treated suboptimally due to poor drug bioavailability and the side effects of high systemic doses. Localized drug delivery systems present a promising alternative, offering targeted and sustained release directly at the site of pathology. Recent advances in 3D printing technologies have accelerated the development of such systems by enabling the fabrication of drug delivery platforms with customizable geometries and controlled release profiles. While the fabrication of these systems has become increasingly accessible, challenges remain in ensuring their functional performance, drug compatibility, and reproducibility. Many studies have aimed to harness the resolution and precision of additive manufacturing (AM) to fine-tune pharmacokinetics, but limitations persist, particularly regarding the low rates of drug release and insufficient material characterization. Among the emerging AM techniques, two-photon polymerization (2PP) stands out for its ability to produce microscale structures with sub-micron resolution. This capability allows for the fabrication of platforms that, in principle, can accommodate a wide range of pharmaceutical compounds, opening new possibilities for site-specific therapies in the inner ear. This thesis addresses a critical clinical need by exploring the potential of 2PP for the fabrication of cochlea-specific drug delivery systems.

Part I of the thesis (**Chapter 2**) focuses on the design and fabrication of cochlear implants using the IP-Q photoresist and 2PP. Multiple implant designs were developed by combining two macro-geometries (cylindrical and rectangular) with two levels of internal porosity (20 μm and 60 μm). The implants were fabricated with high fidelity and reproducibility, achieving pore dimensions within 10% of the design values. Characterization included assessments of morphology, surface roughness, water contact angle, and degree of polymerization. Importantly, cytocompatibility

was validated using murine macrophages, confirming the suitability of the printed materials for biomedical use.

Part II (Chapter 3 and 4) investigates the mechanical properties of the printed implants and related microscale structures. **Chapter 3** presents a comparative analysis of solid and porous microstructures (approximately seven times smaller than the cochlear implants in **Part I**) fabricated using three commercial resins: IP-Q, IP-S, and IP-PDMS. Mechanical and chemical testing explored the influence of material choice and porosity on stiffness and degree of polymerization. The results highlighted the mechanisms affecting polymerization and demonstrated the impact of scale on material behavior. A systematic resin characterization enabled the definition of optimal printing parameters for microscale porous architectures. **Chapter 4** addresses the challenge of testing real-size implants by developing a hybrid computational-experimental approach. Scaled-up implant models were printed using stereolithography and subjected to torsion testing, while finite element simulations predicted the mechanical behavior of real-sized 2PP implants. This approach revealed the mechanical superiority of the cylindrical geometry, regardless of internal pore size, emphasizing the dominant influence of global shape over internal architecture on structural performance.

Part III (Chapter 5), investigates the drug delivery functionality of the fabricated implants. Through experimental studies, this chapter demonstrates the feasibility of creating anatomically relevant, microporous cochlear implants with customizable geometries and porosities, enabling finely tuned drug release while maintaining structural integrity and cytocompatibility. Two designs, the cylindrical implant with 60 μm pores and a hollow variation, were loaded with ibuprofen and subjected to *in vitro* release studies under both physiological and acidic conditions. Results showed the potential for sustained drug release over 84 days and revealed pH-responsive behavior. Micro-computed tomography enabled analysis of ibuprofen spatial distribution, revealing deviations in release profiles and highlighting the need for improved or alternative drug-loading strategies. Lastly, gene expression analysis of macrophages exposed to ibuprofen provided preliminary insights into the platform's potential for inflammatory suppression.

This thesis provides a proof-of-concept for customizable, biocompatible, and mechanically robust cochlear implants capable of long-term drug delivery. The use of 2PP enables precise control over architecture, particularly porosity, which influences both mechanical and pharmacokinetic behavior. The work contributes to the methodological foundation for future cochlear implant development, characterization, and evaluation. More broadly, it demonstrates the transformative potential at the intersection of high-resolution AM and pharmaceutical science. By offering a modular platform for inner ear drug delivery, this research opens the door to more effective, patient-tailored treatments for hearing loss and other inner ear disorders.

SAMENVATTING

Geneesmiddeltoediening aan anatomisch complexe en fysiologisch afgeschermd regio's van het lichaam blijft een grote uitdaging binnen de farmaceutische wetenschappen. In het binnenoor beperkt de bloed-labyrintbarrière de effectiviteit van systemisch toegediende geneesmiddelen aanzienlijk. Hierdoor worden aandoeningen zoals perceptiedoofheid, de ziekte van Ménière en tinnitus vaak niet optimaal behandeld, zowel vanwege de lage biologische beschikbaarheid van geneesmiddelen als vanwege de bijwerkingen die gepaard gaan met hoge systemische doseringen. Gelokaliseerde geneesmiddeltoedieningssystemen bieden een veelbelovend alternatief, doordat zij een gerichte en langdurige afgifte mogelijk maken direct ter plaatse van de pathologie. Recente ontwikkelingen in 3D-printtechnologieën hebben de totstandkoming van dergelijke systemen versneld door de vervaardiging van geneesmiddelplatforms met aanpasbare geometrieën en gecontroleerde afgifteprofielen mogelijk te maken. Hoewel de technische toegankelijkheid van deze methoden is toegenomen, blijven uitdagingen bestaan ten aanzien van functionele prestaties, geneesmiddelcompatibiliteit en reproduceerbaarheid. Vele studies hebben gepoogd de resolutie en precisie van additieve productie (AM) te benutten om farmacokinetische parameters te optimaliseren, maar beperkingen blijven bestaan, met name met betrekking tot lage afgiftesnelheden en onvoldoende materiaalkarakterisering. Onder de opkomende AM-technieken onderscheidt twee-fotonpolymerisatie (2PP) zich door het vermogen microstructuren met submicronresolutie te vervaardigen. Deze techniek maakt de productie van platforms mogelijk die, in principe, een breed scala aan farmaceutische verbindingen kunnen huisvesten, waarmee nieuwe perspectieven voor locatiespecifieke therapieën in het binnenoor worden geopend. Dit proefschrift richt zich op deze klinische behoefte door het potentieel van 2PP voor de vervaardiging van cochleair-specifieke geneesmiddeltoedieningssystemen te onderzoeken.

Deel I van dit proefschrift (**Hoofdstuk 2**) behandelt het ontwerp en de vervaardiging van cochleaire implantaten met behulp van de IP-Q-fotoresist en 2PP. Diverse implantaatontwerpen werden ontwikkeld door twee macrogeometrieën (cilindrisch

en rechthoekig) te combineren met twee niveaus van interne porositeit (20 μm en 60 μm). De implantaten werden met hoge nauwkeurigheid en reproduceerbaarheid vervaardigd, waarbij de gerealiseerde poriedimensies binnen 10% van de ontwerpwaarden bleven. De karakterisering omvatte analyses van morfologie, oppervlakteruwheid, watercontacthoek en polymerisatiegraad. Daarnaast werd de cytocompatibiliteit bevestigd met behulp van muriene macrofagen, waarmee de geschiktheid van de vervaardigde materialen voor biomedisch gebruik werd aangetoond.

Deel II (Hoofdstuk 3 en 4) onderzoekt de mechanische eigenschappen van de vervaardigde implantaten en gerelateerde microstructuren. **Hoofdstuk 3** presenteert een vergelijkende analyse van dichte en poreuze microstructuren (ongeveer zevenmaal kleiner dan de cochleaire implantaten in **Deel I**), vervaardigd uit drie commerciële harsen: IP-Q, IP-S en IP-PDMS. Mechanische en chemische karakterisering werd uitgevoerd om de invloed van materiaalkeuze en porositeit op stijfheid en polymerisatiegraad vast te stellen. De resultaten benadrukten de mechanismen die de polymerisatie beïnvloeden en toonden de impact van schaalgrootte op materiaalgedrag aan. Systematische harskarakterisering maakte het mogelijk optimale printparameters voor microporeuze architecturen te definiëren. In **Hoofdstuk 4** wordt de uitdaging van het testen van implantaten op ware grootte aangepakt via een hybride rekenkundig-experimentele benadering. Vergrote implantaatmodellen werden vervaardigd door stereolithografie en onderworpen aan torsietesten, terwijl eindige-elementensimulaties het mechanische gedrag van 2PP-implantaten op werkelijke schaal voorspelden. Deze benadering wees op de mechanische superioriteit van de cilindrische geometrie, ongeacht de interne poriegrootte, en onderstreepte de dominante invloed van de globale vorm boven de interne architectuur op de structurele prestaties.

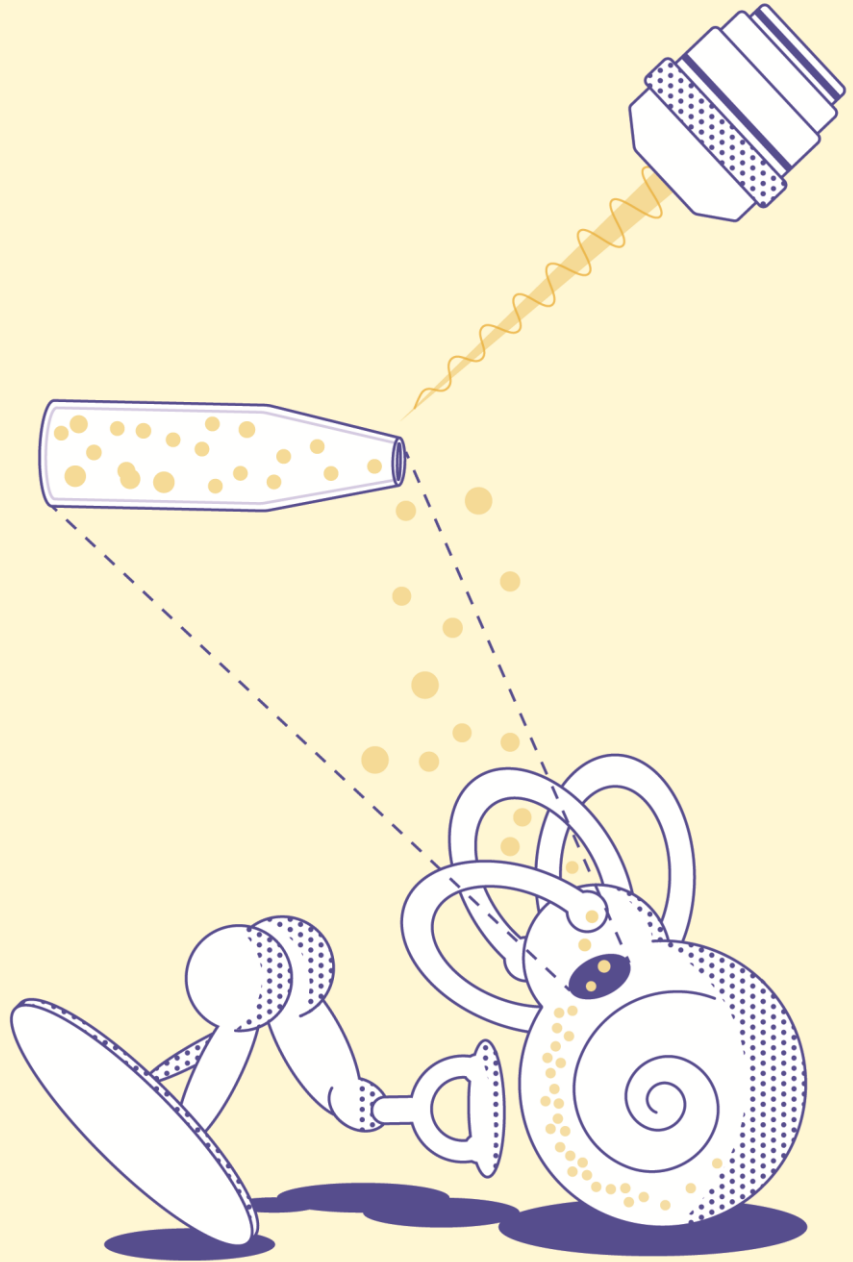
Deel III (Hoofdstuk 5), richt zich op de geneesmiddelafgiftefunctionaliteit van de vervaardigde implantaten. Op basis van experimentele en rekenkundige studies wordt de haalbaarheid aangetoond van het vervaardigen van anatomisch relevante, microporeuze cochleaire implantaten met aanpasbare geometrieën en porositeiten, die een gecontroleerde geneesmiddelafgifte mogelijk maken bij behoud van

structurele integriteit en cytocompatibiliteit. Twee ontwerpen - het cilindrische implantaat met 60 μm poriën en een holle variant - werden beladen met ibuprofen en onderworpen aan *in vitro* afgifteonderzoeken onder zowel fysiologische als zure omstandigheden. De resultaten toonden het potentieel voor langdurige geneesmiddelafgifte over een periode van 84 dagen en onthulden pH-afhankelijk gedrag. Micro-computertomografie maakte ruimtelijke analyse van de ibuprofenverdeling mogelijk, waarbij afwijkingen in de afgifteprofielen zichtbaar werden en de noodzaak van verbeterde of alternatieve ladingsstrategieën werd benadrukt. Voorts leverde genexpressieanalyse van macrofagen blootgesteld aan ibuprofen voorlopige aanwijzingen voor het ontstekingsremmende potentieel van het platform.

Dit proefschrift levert een conceptbewijs voor aanpasbare, biocompatibele en mechanisch robuuste cochleaire implantaten die in staat zijn tot langdurige geneesmiddelafgifte. Het gebruik van 2PP maakt een nauwkeurige controle van architecturale parameters, in het bijzonder porositeit, mogelijk, hetgeen zowel het mechanische als farmacokinetische gedrag beïnvloedt. Het gepresenteerde werk draagt bij aan de methodologische basis voor toekomstige ontwikkeling, karakterisering en evaluatie van cochleaire implantaten. Breder beschouwd toont dit onderzoek het transformerende potentieel aan van de kruisbestuiving tussen hoge-resolutie additieve productie en farmaceutische wetenschappen. Door een modulair platform te bieden voor geneesmiddeltoediening in het binnenoor opent dit werk de weg naar effectievere, patiëntspecifieke therapieën voor gehoorverlies en andere binnenooraandoeningen.

Chapter 01

Introduction



1. INTRODUCTION

1.1. BACKGROUND

For nearly 100 years, pursuing increasingly effective drug formulations has driven medicine, drug discovery, and pharmaceuticals [1]. A persistent challenge in modern drug development is creating systems that precisely target diseases while minimizing off-target effects [2]. Achieving this balance is intricate and intriguing, partially due to the inherent biological complexity of the human body [3]. Factors such as enzymatic activity, pH, vascularization, and physiological barriers significantly influence drug absorption, while patient-specific variables further impact pharmacokinetics and pharmacodynamics [4,5]. Despite considerable advancements and a deeper understanding of biological pathways and gene expression, most treatments still rely on systemic drug distribution [6]. This widespread approach often results in suboptimal therapeutic efficacy and severe side effects, which account for approximately 200000 deaths annually in Europe alone [7].

1.2. DRUG DELIVERY TO THE INNER EAR

The inner ear presents a unique and challenging target for drug delivery due to its delicate anatomy and physiological barriers, such as the round and oval windows, which limit access to its internal structures. Traditional systemic drug delivery approaches are often ineffective for inner ear disorders because they fail to achieve therapeutic concentrations within the cochlea while minimizing systemic side effects. This inefficiency arises from the protective barriers surrounding the inner ear, such as the blood-labyrinth barrier, which is analogous to the blood-brain barrier and restricts the entry of many therapeutic agents.

To overcome these challenges, localized drug delivery to the inner ear has gained significant attention. This approach ensures the delivery of therapeutic agents directly to the cochlea, bypassing systemic pathways and allowing for higher drug concentrations at the site of action that are infeasible to achieve through systemic delivery. Intratympanic injections, for instance, deliver drugs into the middle ear cavity, where diffusion through the round window membrane facilitates entry into

the inner ear. However, this method often results in inconsistent drug diffusion and a lack of control over release rates, leading to variable therapeutic outcomes [8-10].

Researchers have explored the potential of drug delivery systems (DDS) designed specifically for the cochlea to address these limitations. These systems offer a controlled and sustained release of drugs, ensuring therapeutic efficacy over an extended period while reducing the frequency of administration. Additionally, DDS allow for the incorporation of targeted delivery strategies, such as drug-loaded scaffolds or microscale implants, tailored to the inner ear's anatomy.

Despite advancements in cochlear DDS development, there is a critical need for high-resolution fabrication techniques that can produce precise, customizable delivery vehicles. These systems must not only overcome the anatomical and physiological challenges of the cochlea but also provide tunable drug release profiles suitable for treating diverse inner ear disorders.

1.3. FABRICATION OF A COCHLEAR DRUG DELIVERY SYSTEM

Additive manufacturing (AM) technologies have demonstrated suitability in fabricating DDS across various organs [11-14]. Current methods involve embedding therapeutic agents directly within the 3D printed material (single-step fabrication) or adding them post-printing in a multi-step fabrication process. In single-step fabrication, the dosage can be fine-tuned by adjusting the size of the DDS, offering a scalable solution for personalized medicine. In two-step fabrication, the dosage can be fine-tuned either by adjusting the size of the DDS or adjusting the amount of the therapeutic agent. This approach relies on a particular material-drug combination, limiting the versatility required for broader therapeutic applications.

Among AM technologies, two-photon polymerization (2PP) stands [15-18] out because of its capability to produce high-resolution structures and offers unmatched printing quality, allowing precise control over the geometry and dimensions. These characteristics are particularly suited for addressing the complex anatomical and therapeutic challenges of inner ear disorders. While AM has been extensively applied to drug delivery in other organs, its potential for cochlear applications remains unexplored.

A yet unexplored opportunity exists to use AM to create a DDS tailored for the cochlea. 2PP allows for the incorporation of porosity in the design in an attempt to control drug release and adaptability for a variety of drugs. By adopting a two-step process (i.e., fabricating the DDS and loading it with therapeutic agents), it could be possible to create and study the effect of the porosity in the drug release and the mechanical properties of this modular drug-releasing platform. Such a strategy could allow for the standardization of DDS production while enabling customizable release profiles tailored to different therapeutic agents and individual patient needs. Exploring this field could lead to the development of the first additively manufactured cochlea-specific DDS, enabling precise and effective drug delivery to the inner ear.

1.4. MAIN GOAL AND THESIS OUTLINE

With a focus on the development of drug delivery systems targeted to the cochlea, this thesis aims:

To design and fabricate an additively manufactured, cochlea-specific drug delivery system capable of controlling drug release.

The approach to this goal is to exploit the unique characteristics of 2PP to achieve fabrication of cochlea-specific DDS that incorporate multiple porous structures. The study's objectives are, thus, as follows:

1. To design and fabricate an anatomically relevant, porous cochlear DDS using 2PP.
2. To characterize the fabricated cochlear DDS in terms of its mechanical, physical, and chemical properties.
3. To investigate drug loading into the cochlear DDS and to evaluate the role of porosity in controlling and tailoring drug release profiles.
4. To investigate the effects of the released drug on immune cell responses.

The thesis consists of five chapters split into three parts (**Figure 1.1**).

Part I (Chapter 2), in which we dive into the design and fabrication of cochlear implants using 2PP. We design different types of cochlear implants that incorporate various types of internal pores, and we study the printing quality to determine the

best printing parameters. We assess the chemical and physical properties of the implants and the cytotoxicity of the material on macrophages. In **Part II (Chapters 3 and 4)**, we delve into the mechanical characterization of different scales of cochlear implants made from various materials. **Part III (Chapter 5)** explores the possibility of incorporating a therapeutic agent into our DDS and evaluates the resultant drug-release profile. The information on the released amount of the drug is then used to test the response of macrophages *in vitro*. **Chapter 6** summarizes and discusses the findings of the work presented in the earlier chapters and proposes future research directions for the development of DDS for the cochlea.

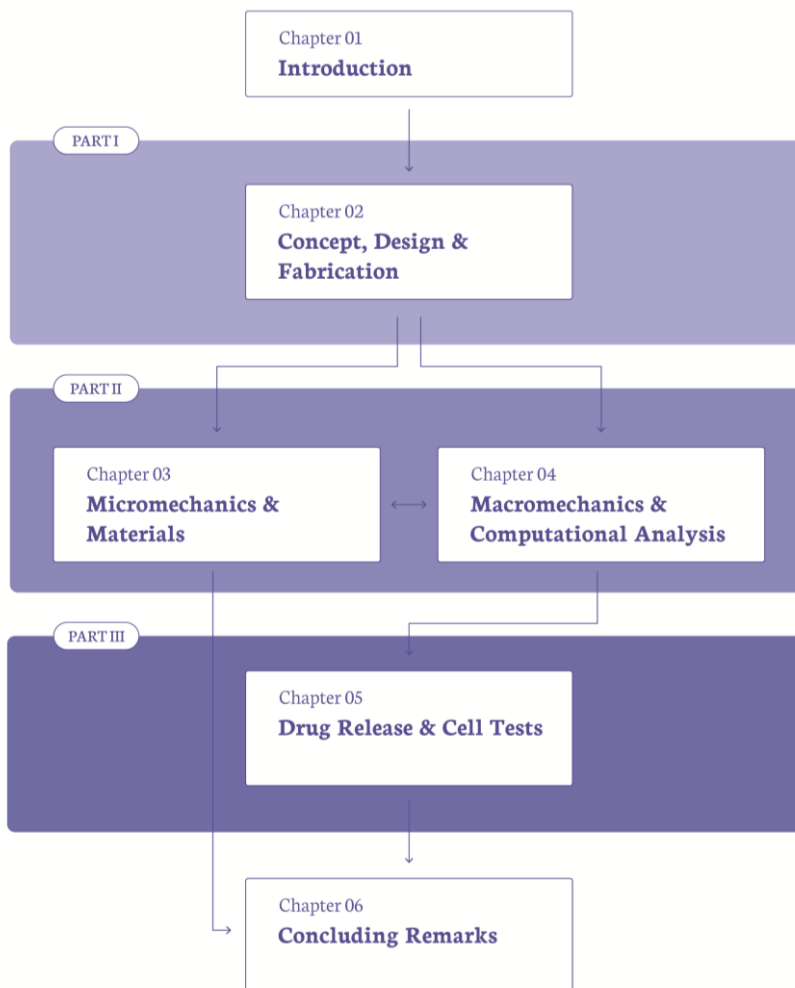


Figure 1.1. Outline of this thesis.

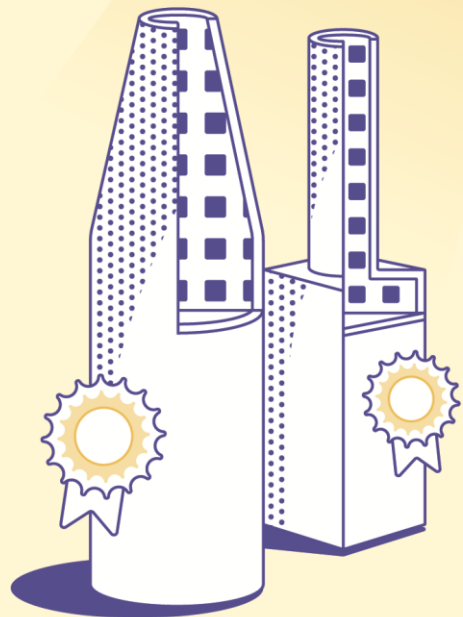
REFERENCES

- [1] J. Drews, Drug Discovery: A Historical Perspective, *Science* (1979) 287 (2000) 1960–1964. <https://doi.org/10.1126/science.287.5460.1960>.
- [2] S. Sinha, D. Vohora, Drug Discovery and Development, in: *Pharmaceutical Medicine and Translational Clinical Research*, Elsevier, 2018: pp. 19–32. <https://doi.org/10.1016/B978-0-12-802103-3.00002-X>.
- [3] P. Imming, C. Sinning, A. Meyer, Drugs, their targets and the nature and number of drug targets, *Nat Rev Drug Discov* 5 (2006) 821–834. <https://doi.org/10.1038/nrd2132>.
- [4] P.S. Burton, J.T. Goodwin, T.J. Vidmar, B.M. Amore, Predicting Drug Absorption: How Nature Made It a Difficult Problem, *Journal of Pharmacology and Experimental Therapeutics* 303 (2002) 889–895. <https://doi.org/10.1124/jpet.102.035006>.
- [5] A.A. Alagga, M. V. Pellegrini, V. Gupta, Drug absorption, (2024). <https://www.ncbi.nlm.nih.gov/books/NBK557405/>.
- [6] K.K. Jain, An Overview of Drug Delivery Systems, in: 2020: pp. 1–54. https://doi.org/10.1007/978-1-4939-9798-5_1.
- [7] J.C. Bouvy, M.L. De Bruin, M.A. Koopmanschap, Epidemiology of Adverse Drug Reactions in Europe: A Review of Recent Observational Studies, *Drug Saf* 38 (2015) 437–453. <https://doi.org/10.1007/s40264-015-0281-0>.
- [8] U. Chavkin, J. Pitaro, H. Gavriel, A. Taha, L. Muallem Kalmovich, S. Shilo, O. Handzel, N. Muhanna, A. Warshavsky, G. Horowitz, O.J. Ungar, The impact of eustachian tube function on intra-tympanic steroid administration, *European Archives of Oto-Rhino-Laryngology* 280 (2023) 143–149. <https://doi.org/10.1007/s00405-022-07475-8>.
- [9] S. Kanzaki, M. Fujioka, A. Yasuda, S. Shibata, M. Nakamura, H.J. Okano, K. Ogawa, H. Okano, Novel In Vivo Imaging Analysis of an Inner Ear Drug Delivery System in Mice: Comparison of Inner Ear Drug Concentrations over Time after Transtympanic and Systemic Injections, *PLoS One* 7 (2012) e48480. <https://doi.org/10.1371/journal.pone.0048480>.
- [10] J.J. Lee, J.H. Jang, O. Choo, H.J. Lim, Y. Choung, Steroid intracochlear distribution differs by administration method: Systemic versus intratympanic injection, *Laryngoscope* 128 (2018) 189–194. <https://doi.org/10.1002/lary.26562>.
- [11] U. Bozuyuk, O. Yasa, I.C. Yasa, H. Ceylan, S. Kizilel, M. Sitti, Light-Triggered Drug Release from 3D-Printed Magnetic Chitosan Microswimmers, *ACS Nano* 12 (2018) 9617–9625. <https://doi.org/10.1021/acsnano.8b05997>.
- [12] Y. Huang, W. Wu, H. Liu, Y. Chen, B. Li, Z. Gou, X. Li, M. Gou, 3D printing of functional nerve guide conduits, *Burns Trauma* 9 (2021). <https://doi.org/10.1093/burnst/tkab011>.

- [13] C.P.P. Pere, S.N. Economidou, G. Lall, C. Ziraud, J.S. Boateng, B.D. Alexander, D.A. Lamprou, D. Douroumis, 3D printed microneedles for insulin skin delivery, *Int J Pharm* 544 (2018) 425-432. <https://doi.org/10.1016/j.ijpharm.2018.03.031>.
- [14] Y.-T. Wen, N.-T. Dai, S. Hsu, Biodegradable water-based polyurethane scaffolds with a sequential release function for cell-free cartilage tissue engineering, *Acta Biomater* 88 (2019) 301-313. <https://doi.org/10.1016/j.actbio.2019.02.044>.
- [15] C. LaFratta, T. Baldacchini, Two-Photon Polymerization Metrology: Characterization Methods of Mechanisms and Microstructures, *Micromachines (Basel)* 8 (2017) 101. <https://doi.org/10.3390/mi8040101>.
- [16] S. Kawata, H.-B. Sun, Two-photon photopolymerization as a tool for making micro-devices, *Appl Surf Sci* 208-209 (2003) 153-158. [https://doi.org/10.1016/S0169-4332\(02\)01358-2](https://doi.org/10.1016/S0169-4332(02)01358-2).
- [17] A. Jaiswal, C.K. Rastogi, S. Rani, G.P. Singh, S. Saxena, S. Shukla, Two decades of two-photon lithography: Materials science perspective for additive manufacturing of 2D/3D nano-microstructures, *IScience* 26 (2023) 106374. <https://doi.org/10.1016/j.isci.2023.106374>.
- [18] S. O'Halloran, A. Pandit, A. Heise, A. Kellett, Two-Photon Polymerization: Fundamentals, Materials, and Chemical Modification Strategies, *Advanced Science* 10 (2023). <https://doi.org/10.1002/advs.202204072>.

PART I - Chapter 02

Concept, Design & Fabrication



2. DESIGN & FABRICATION OF COCHLEAR IMPLANTS

Abstract

2

Hearing loss is a highly prevalent multifactorial disorder affecting 20% of the global population. Current treatments using the systemic administration of drugs are therapeutically ineffective due to the anatomy of the cochlea and the existing blood-labyrinth barrier. Local drug delivery systems can ensure therapeutic drug concentrations locally while preventing adverse effects caused by high dosages of systemically administered drugs. Here, we aimed to design, fabricate, and characterize a local drug delivery system for the human cochlea. The design was relevant to the size of the human ear, included two different shapes, and incorporated two different microporous structures acting as reservoirs for drug loading and release. The four cochlear implant designs were printed using the two-photon polymerization (2PP) technique and the IP-Q photoresist. The optimized 2PP process enabled the fabrication of the cochlear implants with great reproducibility and shape fidelity. Rectangular and cylindrical implants featuring cylindrical and tapered tips, respectively, were successfully printed. Their outer dimensions were $0.6 \times 0.6 \times 2.4 \text{ mm}^3$ (L \times W \times H). They incorporated internal porous networks that were printed with high accuracy, yielding pore sizes of $17.88 \pm 0.95 \text{ }\mu\text{m}$ and $58.15 \pm 1.62 \text{ }\mu\text{m}$ for the designed values of $20 \text{ }\mu\text{m}$ and $60 \text{ }\mu\text{m}$, respectively. The average surface roughness was $1.67 \pm 0.24 \text{ }\mu\text{m}$, and the water contact angle was $72.3 \pm 3.0^\circ$. A high degree of polymerization ($\sim 90\%$) of the IP-Q was identified after printing, and the printed material was cytocompatible with murine macrophages. The cochlear implants designed and 3D printed in this study, featuring relevant sizes for the human ear and tunable internal microporosity, represent a novel approach for personalized treatment of hearing loss through local drug delivery.

Isaakidou A., Apachitei I., Fratila-Apachitei L.E. and Zadpoor A.A. High-precision 3D printing of microporous cochlear implants for personalized local drug delivery. *Journal of Functional Biomaterials* 2023. 14(10): 494. [10.3390/jfb14100494](https://doi.org/10.3390/jfb14100494)

2.1. INTRODUCTION

Hearing loss is a globally prevalent clinical condition that can be caused by aging (*i.e.*, presbycusis), untreated chronic infections of the inner ear, autoimmune inner ear disease (AIED), conductive hearing loss (CHL), sensorineural hearing loss (SNHL), and noise-induced hearing loss (NIHL) [1]. It currently affects more than 1.5 billion people, representing approximately 20% of the world's population, and is expected to affect over 2.5 billion people by 2030 [2,3]. Auditory dysfunctions require different types of treatments depending on the site of malfunction (*e.g.*, ossicular chain, sensory hair cells, auditory nerve). The traditional approach to restoring presbycusis, for example, involves the use of hearing aid devices that amplify sound waves to enhance perception by the patient. However, incomplete hearing restoration and background noise amplification lead to discomfort and long adjustment periods for the patients [4]. Another example is the use of cochlear implants to treat SNHL. The procedure involves the implantation of an electrode to stimulate the cochlear nerve (internal component) as well as the fixation of a wearable device to the skull behind the ear (external component) that communicates with the nerve stimulator. The use of cochlear implants is shown to improve auditory function and language skills in both adults and children [5]. Nonetheless, the invasiveness of the implantation procedure remains a limitation. Despite progress in electrode positioning techniques, the hearing outcome can vary significantly between patients [6]. Moreover, there is a risk of trauma and loss of residual hearing [5]. The systemic administration of drugs, on the other hand, has been clinically practiced in the treatment of vertigo, SNHL, noise hearing loss, and Meniere's disease [7-9]. However, insufficient bioavailability of the drug in the inner ear presents a major challenge. High drug clearance rates from the circulation and minimal uptake through the anterior vestibular artery may result in limited to no hearing enhancement while also creating the risk of organ failure [1]. Local delivery of therapeutic agents (*e.g.*, corticosteroids, antibiotics, aminoglycosides, calcineurin) to the inner ear is, therefore, desirable for the efficient treatment of such conditions and for preventing permanent hearing loss. Nevertheless, the anatomy of the ear hampers the accessibility and controlled release of therapeutics due to the various ear barriers (*i.e.*, the tympanic membrane, the oval

and round window, and the blood-labyrinth barrier) that constitute challenges for the delivery of small molecules to the inner ear [3-7]. Current research strategies for local drug delivery include intracochlear infusion of therapeutic agents after cochleostomy, which are promising in terms of sustained long-term drug delivery to the cochlea [10]. In general, intracochlear approaches are highly invasive, and the trade-off between the therapeutic effect and the risks involved (*e.g.*, traumatic electrode placement, loss of residual hearing, and electrode translocation) may not always be favorable [5,6]. Other approaches focus on perforating the natural barrier of the round window membrane to directly reach the intracochlear space [11-13]. Related to the latter, dexamethasone-loaded poly(lactic-co-glycolic acid) (PLGA) rod-like extrudates have showcased the possibility of delivering dexamethasone through the round window membrane under *in vitro* conditions for up to 84 days [13,14]. Silicone microdevices featuring a tip that can be fixed at the round window membrane [12] have been tested *in vitro* and are shown to be capable of delivering dexamethasone to the inner ear. Nevertheless, drug release rates are limited due to the limited mobility and solubility of the drug in the silicone matrix. Investigations of diffusional mass transport both *in vitro* and *in vivo* from silicon-based cochlear implants loaded with dexamethasone showed that drug saturation in the cochlea plays a crucial role in the release rate [15,16].

As is clear from this literature review, there is a need for a local drug delivery system (DDS) to the inner ear that addresses the existing anatomical and functional challenges and limitations. An ideal DDS for the inner ear should (1) increase the bioavailability of the drug in the cochlea, (2) deliver the optimum dose of the drug to the cochlea with the appropriate kinetics, (3) exhibit anatomically relevant sizes and possess suitable mechanical properties, (4) be customizable and be fabricated on-demand to accommodate the patient's needs, (5) enable the combination of multiple therapeutic agents, (6) decrease the surgical risk and be less invasive than the existing therapies, and (7) be cost-effective.

Recent progress in additive manufacturing (AM) techniques has enabled researchers and pharmaceutical companies to fabricate DDS with tailored properties, such as intricate geometries at scales relevant to various clinical applications combined with

a range of therapeutics [17-21]. For example, stereolithography (SLA), fused deposition modeling (FDM), selective laser sintering (SLS), and binder jetting (BJ) have enabled the fabrication of dosage forms in various shapes, sizes, colors, and flavors [22-25] with customizable release profiles, a combination of therapeutic agents [26], and pH-responsive drug release behavior [27]. As an ultrahigh-resolution AM technique, two-photon polymerization (2PP) has enabled the fabrication of magnetic steerable helical micro-swimmers for the delivery of cell differentiation factors and neural stimulation [28] and light-responsive micro-swimmers for on-demand local delivery of chemotherapeutic agents [29]. However, AM techniques have not yet been applied for the 3D printing of DDS for the inner ear.

A high-resolution 3D printing technique enabling the fabrication of millimeter-sized structures is needed to produce implants for the inner ear. Two-photon polymerization is an ultrahigh-resolution AM technique, which is also known and referred to as dip-in laser lithography (DiLL), multiphoton polymerization (MPP), 3D laser lithography, and femtosecond laser writing, and is an appropriate choice for this task [30]. Two-photon polymerization involves a nonlinear optical process that takes advantage of the simultaneous absorption of two photons by a molecule [30]. More specifically, a femtosecond laser pulse (100–200 fs) with a mean wavelength in the near-infrared spectrum (~780 nm) provides a high photon density to enable simultaneous absorption of two photons by a photo-initiating molecule within the photosensitive resin, which is transparent in the infrared range [31]. Photosensitive resins contain photoinitiators that are excited from their ground state and initiate polymerization [32]. Excitation of the photoinitiators occurs around the focus of the laser beam, where the photon density is highest, and subsequent diffusion of reactive species can lead to polymerization within a localized volume, commonly referred to as the voxel. This process enables the fabrication of features as small as ~25 nm [33,34]. The intended structure is built by overlapping voxels in a layer-by-layer manner (**Figure 2.1A**). Recently, this AM technique has been widely studied for biomedical applications (*e.g.*, scaffolds for tissue engineering, microneedles for drug delivery, and 3D micro- and nanotopographies for *in vitro* systematic studies of cellular processes) [30,35-38].

Porosity can be used as a storage reservoir for drugs as well as for controlled drug release without the use of additional materials [21,39]. This is of relevance for local drug delivery in various tissues, as it may provide a safer and easier-to-control system compared to the use of biodegradable drug carriers incorporated in the devices. Furthermore, when the location in the tissue is difficult to reach and/or drug bioavailability is limited due to inherent barriers, as in the case of cochlear implants, such systems need to be fabricated with high precision and suitable length scales taking into account the complex anatomy of the site. Therefore, in this study, we investigated for the first time the possibility of designing and fabricating a local DDS for human cochlea featuring internal microporous structures and clinically relevant sizes. To this aim, several different designs have been proposed for the DDS, and 2PP was explored as a method of fabrication. Following optimization of the 2PP conditions to reproducibly and accurately print the designed implants, these were characterized with regard to their morphology, chemistry, surface topography, and wettability. In addition, the cytocompatibility of the printed material was assessed using *in vitro* assays and immune cells (*i.e.*, murine macrophages).

2.2. MATERIALS AND METHODS

2.2.1. IMPLANT DESIGN

The implants were designed through a workflow that combined two software suites: SolidWorks 2021 (Dassault Systèmes SE, France) and nTopology 2.6 (nTopology Inc., New York, NY, USA). SolidWorks was used to design the outer geometry of the implants, while nTopology was applied to design their inner porous geometry. The final design was assembled in nTopology, where both designs were merged and prepared for printing. The output file was exported as a standard tessellation language (STL) file, which is suitable for 3D printing. The implant design (outer and inner geometries and dimensions) considered the functional requirements and anatomy of the human inner ear (round window). To increase the bioavailability of the locally administered drug and to effectively deliver the drug directly to the cochlea, the design included a main body that serves as a drug reservoir and a tip that penetrates the cochlea through the round window (**Figure 2.1B**). Two different implant shapes

2. DESIGN & FABRICATION OF COCHLEAR IMPLANTS

were considered, namely rectangular implants (R) with a cylindrical tip and cylindrical implants (C) with a tapered tip. The outer designed dimensions of the cochlear implants were $2.4 \times 0.6 \times 0.6 \text{ mm}^3$ ($L \times W \times H$).

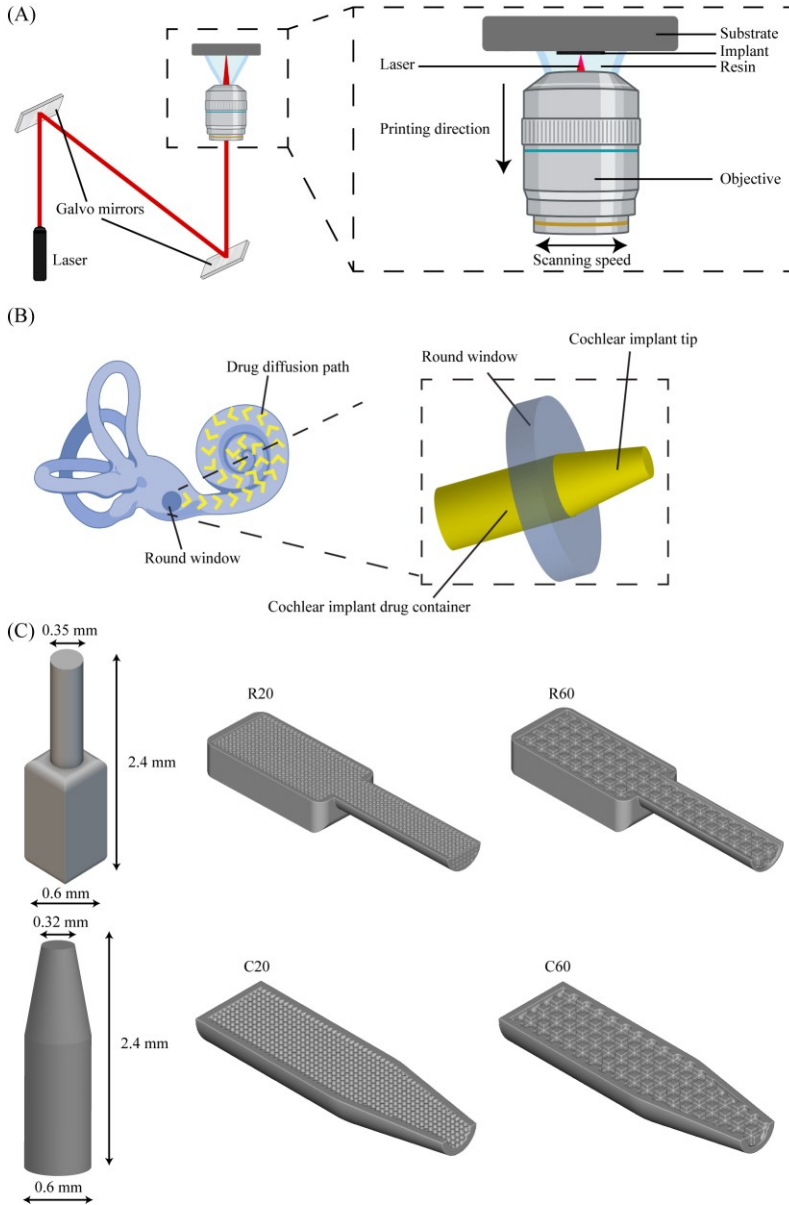


Figure 2.1. (A) The working principle of the 2PP 3D-printing setup, (B) a schematic representation of the implant and its positioning in the cochlea, and (C) cochlear implant designs and dimensions.

An internal porous structure was designed to control the drug release, which consisted of an interconnected network of square pores. Two different pore sizes were included for each shape, namely, 20 and 60 μm , resulting in four different implant designs (*i.e.*, R20, R60, C20, and C60) (**Figure 2.1C**). The pore size was chosen based on the results of a preliminary study (as detailed below) and in line with the existing literature on DDS [40].

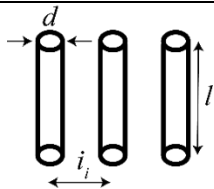
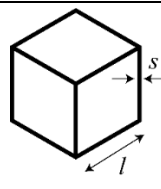
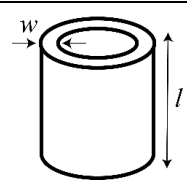
2.2.2. PRELIMINARY STUDY: 3D PRINTING OF TEST STRUCTURES

The printing process for the cochlear implants began with a preliminary study in which test structures were printed to determine the printing conditions and their relationships with the dimensions of the outer and inner shapes and the porous structure. The test structures included the following: (a) arrays of pillars that were used to determine the printing conditions of high aspect ratio features considering the residual polymerization and its effect on neighboring printed features, (b) cubic unit cells that were used to determine the pore size, and (c) hollow cylindrical structures that enabled us to determine the wall thickness of the cylindrical implants (type C) and the cylindrical tip diameter for the rectangular implants (type R) (**Table 2.1**). The results of this preliminary study were then used to define a suitable set of printing parameters for the final designs.

Arrays of 17 pillars with a diameter of $d_i = 5 \mu\text{m}$, a length of $l = 80 \mu\text{m}$, and an ascending interspace ranging between $i_i = 5 \mu\text{m}$ and $20 \mu\text{m}$ were designed and printed. The aspect ratio, $AR = 16$, was chosen according to the manufacturer's instructions for the solution set for large features to determine suitable printing parameters and to ensure the printability of a complete cochlear implant. The pillar arrays were designed in nTopology (nTopology Inc., New York, NY, USA) and were meshed and imported as an STL file into the proprietary job preparation software of the 2PP printer (*i.e.*, Describe, Nanoscribe, Eggenstein-Leopoldshafen, Germany), where they were prepared for printing. The arrays were printed from the IP-Q resin (Nanoscribe GmbH, Eggenstein-Leopoldshafen, Germany) in the dip-in-laser lithography (DiLL) mode using the microscope z-drive scanning method of the Photonic Professional GT laser lithography system (Nanoscribe GmbH, Eggenstein-Leopoldshafen, Germany) with a scanning speed (v) of $150,000 \mu\text{m/s}$, a slicing distance (s) of $5 \mu\text{m}$, and a

hatching distance (h) of $1 \mu\text{m}$. The effects of three different laser powers ($LP_1 = 25 \text{ mW}$, $LP_2 = 40 \text{ mW}$, and $LP_3 = 50 \text{ mW}$) on the morphology and interspace of the printed pillars were determined. The arrays of pillars were gold sputtered (gold layer thickness $\sim 5 \text{ nm}$) using a sputter coater (JFC-1300, JEOL, Akishima, Japan) and were subsequently imaged using a scanning electron microscope (SEM) (JSMIT100, JEOL, Akishima, Japan).

Table 2.1. The geometry, dimensions, and printing settings used for the fabrication of the test structures, including pillar arrays, cubic unit cells, and hollow cylindrical structures.

	Pillar Array	Cubic Unit Cell	Hollow Cylinder
			
Geometrical characteristics	$l = 80 \mu\text{m}$ $d = 5 \mu\text{m}$ $i_n = 5 \mu\text{m} + (n - 1)$, for $1 \leq n \leq 16$	$l = 240 \mu\text{m}$ $s = 20, 30, 40, 50 \mu\text{m}$	$l = 240 \mu\text{m}$ $w = 20, 30, 40, 50, 75, 100 \mu\text{m}$ $AR = 1$
2PP printing parameters		$LP = 25, 40, 50 \text{ mW}$ $v = 150000 \mu\text{m/s}$ $s = 5 \mu\text{m}$ $h = 1 \mu\text{m}$	

Cubic unit cells with an edge length of $l = 240 \mu\text{m}$ and strut widths of $s_1 = 20 \mu\text{m}$, $s_2 = 30 \mu\text{m}$, $s_3 = 40 \mu\text{m}$, and $s_4 = 50 \mu\text{m}$ were designed using SolidWorks. The geometries were then meshed and imported as an STL file into Describe, where they were prepared for printing. We then printed these with IP-Q resin in the DiLL mode and using the microscope z-drive scanning method and the same 2PP equipment. Three different laser powers of $LP_1 = 25 \text{ mW}$, $LP_2 = 40 \text{ mW}$, and $LP_3 = 50 \text{ mW}$ were used together with a constant scanning speed of $v = 150,000 \mu\text{m/s}$, a slicing distance of $s = 5 \mu\text{m}$, and a hatching distance of $h = 1 \mu\text{m}$. Similarly, hollow cylinders with a length of $l = 240 \mu\text{m}$, $AR=1$, and wall thicknesses of $w_1 = 100 \mu\text{m}$, $w_2 = 75 \mu\text{m}$, $w_3 = 50 \mu\text{m}$, $w_4 = 40 \mu\text{m}$, $w_5 = 30 \mu\text{m}$, and $w_6 = 20 \mu\text{m}$ were designed using the same software and were processed and printed under the same printing conditions as described above. The effects of the three different laser powers on the morphology and shape fidelity of the

structures were assessed. Following 3D printing, the structures were imaged with the same SEM equipment. All materials and reagents were used as received unless otherwise specified.

2.2.3. 3D PRINTING OF COCHLEAR IMPLANTS

The implants were fabricated using the above-described 2PP equipment from the IP-Q photoresist. The 2PP system uses a femtosecond fiber laser with a center wavelength of 780 nm, operating at 80 MHz with a pulse duration of 100 fs. All designs were meshed in nTopology (nTopology Inc., New York, NY, USA) and were imported as an STL file into Describe, where a general writing language (GWL) file was produced for printing. The implants were prepared for printing at 2 orientation angles, namely 0° and 90°.

First, square silicon wafer chip substrates ($25 \times 25 \times 0.725 \text{ mm}^3$) were wiped with acetone (Sigma-Aldrich, Darmstadt, Germany), followed by isopropyl alcohol (IPA) (Sigma-Aldrich, Darmstadt, Germany). Then, they were activated with oxygen plasma for 15 min, followed by silanization for 1 h in a 2% 3-(trimethoxysilyl)propyl methacrylate (Sigma-Aldrich, Darmstadt, Germany) solution in ethanol. Finally, they were rinsed in acetone (Sigma-Aldrich, Darmstadt, Germany) and demineralized water, followed by blow-drying with compressed air.

The galvo writing mode and the dip-in configuration (DiLL) were used to fabricate the samples. Therefore, a droplet of IP-Q photoresist was placed on top of the previously silanized silicon substrates. While printing, the laser beam was focused within the resin through a 10× objective lens with a numerical aperture (NA) of 0.3. The cochlear implants were fabricated with a laser power of $LP = 50 \text{ mW}$ based on the results of the preliminary study on the test structures. The other parameters were as follows: $v = 150000 \text{ } \mu\text{m/s}$, $s = 5 \text{ } \mu\text{m}$, and $h = 1 \text{ } \mu\text{m}$. After printing, the samples were immersed in 1,2-propanediol monomethyl ether acetate (PGMEA) (Sigma-Aldrich, Darmstadt, Germany) for 25 min and then in methoxy-nonafluorobutane $\text{C}_4\text{F}_9\text{OCH}_3$ (Novec 7100) (Sigma-Aldrich, Darmstadt, Germany) for 30 s. Finally, the samples were dried by blow-drying with compressed air.

2.2.4. 3D PRINTING OF SAMPLES FOR IP-Q CHARACTERIZATION

To study the chemical composition, wettability, and cytotoxicity of the printed photocurable IP-Q resin, square blocks of $2.0 \times 2.0 \times 0.5 \text{ mm}^3$ (L \times W \times H) were printed under similar conditions as reported for the implants. Since the size of these samples exceeded the printing field of the 10 \times objective (*i.e.*, $\varnothing 1000 \mu\text{m}$), they were printed in 9 blocks of $705 \times 705 \times 500 \mu\text{m}^3$ (L \times W \times H) with a block shear angle of 15° and a block overlap distance of $5 \mu\text{m}$ in the xy-plane. After printing, the samples were processed following the same steps described above for the implants.

2.2.5. MORPHOLOGICAL CHARACTERIZATION

The morphology of the printed cochlear implants was evaluated using SEM. The specimens were, therefore, gold coated using a sputter coater (JFC-1300, JEOL, Akishima, Japan) and imaged under different tilt angles and magnifications with the same SEM equipment as mentioned above. The theoretical porosity, φ , of the four implant types was calculated from the digital designs as follows (**Table 2.2**):

$$\varphi = (V_I - V_L) / (V_S - V_I) \times 100\% \quad (\text{Eq. 2.1})$$

where V_I is the volume of the solid insert (mm^3), V_L is the volume of the lattice (mm^3), V_S is the volume of the implant shell (mm^3), and φ is the porosity of the insert lattice volume (%).

Table 2.2. The theoretical porosity φ of the implants based on **Eq. 2.1**.

	R20	R60	C20	C60
Volume of the implant shell, V_S (mm^3)	0.15	0.15	0.19	0.19
Volume of the solid insert, V_I (mm^3)	0.41	0.41	0.33	0.33
Volume of the lattice, V_L (mm^3)	0.22	0.20	0.16	0.16
Porosity, φ (%)	46	52	50	50

2.2.6. SURFACE TOPOGRAPHY

The topography of the outer surfaces of the implants was characterized using a non-contact optical profilometer (Profil3D[®], Filmetrics Inc., San Diego, CA, USA). The arithmetical mean height (S_a) was determined using the proprietary Filmetrics processing software (ProfilOnline, San Diego, CA, USA). Each sample was scanned at a minimum of 3 different areas. The mean of the roughness readings corresponded to the areal roughness of that specimen. In total, 3 samples per implant type (*i.e.*, R, C)

were scanned. Moreover, line profiles were acquired to determine the average surface roughness (R_a).

2.2.7. CHEMICAL CHARACTERIZATION

The surface chemistry of the square samples after 2PP was assessed using X-ray photoelectron spectroscopy (XPS, Thermo Fisher K-Alpha, Rockford, IL, USA). Three scans were acquired for each square block with an energy step of 0.6 eV using an Al K α source gun with a spot size of 400 μm^2 in the standard lens mode. Another 3 scans were acquired from points near the square blocks to account for the adventitious carbon contamination on the silicon samples and were used as a charge reference for the XPS spectra correction of IP-Q.

Fourier transform infrared spectroscopy (FTIR) was also performed to identify the functional groups of the IP-Q photoresist before and after printing, allowing the assessment of the effect of the 2PP printing on the functional groups. The FTIR measurements were conducted using a Nicolet FTIR spectrometer 6700 (Thermo Fisher Scientific, Waltham, MA, USA). The spectra were acquired in the range of 4000–650 cm^{-1} using the attenuated total reflection (ATR) element.

2.2.8. WETTABILITY AND SURFACE FREE ENERGY

The wettability of 2PP printed blocks ($5 \times 5 \times 0.5 \text{ mm}^3$) was measured using a drop shape analyzer (DSA 100, Kruss, Hamburg, Germany). Droplets (2 μL) of deionized water and diiodomethane (2 μL) were placed on the specimens, and the right and left contact angles of the droplet formed on the substrate were recorded for 2 s at a rate of 5 fps at room temperature (20 °C). The mean contact angle was used in further calculations. The measurements were repeated 5 times. The wettability was expressed as the water contact angle.

The surface free energy was calculated using Young's equation [41]:

$$\sigma_{SV} = \sigma_{SL} + \sigma_{LV} \times \cos\theta \quad (\text{Eq. 2.2})$$

where σ_{SV} is the interfacial free energy of the solid and the vapor, σ_{SL} is the interfacial tension between the solid and liquid, and σ_{LV} is the interfacial free energy of the liquid and the vapor.

The total surface free energy (SFE) was calculated according to the Owens, Wendt, Rabel and Kaelble (OWRK) method and following the equation [42]:

$$\sigma_S = \sigma_S^P + \sigma_S^D \quad (\text{Eq. 2.3})$$

where σ_S^P is the polar component of the surface energy of the solid, and σ_S^D is the dispersive component of the surface energy of the solid [42-44].

2.2.9. CYTOTOXICITY

Murine macrophages (J774A.1, Merck KGaA, Hamburg, Germany) at passage 14 were pre-cultured in 75 cm² flasks (Greiner Bio-One GmbH, Kremsmünster, Austria) at a concentration of 7×10^5 cells per mL with 20 mL of Dulbecco's Modified Eagle's medium at 37 °C and 5.0% CO₂ for 3 days. The 2PP block samples were sterilized in 70% ethanol (Sigma-Aldrich, Hamburg, Germany) (3× for 2 min each) and then rinsed with PBS (10×) (3× for 2 min each). Subsequently, the specimens were seeded with 2.5×10^4 cells per mL in 24-well cell culture plates.

Macrophage viability was investigated using a live/dead assay with calcein acetoxymethyl (AM) and ethidium homodimer-1 (EthD-1) (ThermoFisher Scientific, Waltham, MA, USA) after 48 h of culture. The cells were rinsed with PBS (10×) and PBS (1×) and were incubated at room temperature in a solution of 0.1 μL/mL calcein AM/PBS (1×) and 1.5 μL/mL EthD-1/PBS (1×) for 30 s. Afterward, the solution was replaced with PBS 1×, and the cells were imaged with a fluorescent microscope (ZOE Fluorescent Cell Imager, BioRad, Hercules, CA, USA). The experiment was performed in triplicate. Cells cultured directly on the well plates and not exposed to the specimens served as the positive controls.

2.2.10. IMAGE ANALYSIS

Both SEM and fluorescent images were processed with ImageJ 1.47 [45]. In the SEM images, the geometrical characteristics of interest were measured using the Measure command. The fluorescent images were converted to grayscale, followed by a local thresholding step. The cell area was quantified using the Analyze Particle command for both live and dead cells, and the ratio of the dead to the live cells was calculated. Cell viability was calculated as follows:

$$\text{Cell viability} = \left(1 - \frac{\text{Area of dead cells}}{\text{Area of living cells}} \right) \times 100\% \quad (\text{Eq. 2.4})$$

2.2.1.1. STATISTICAL ANALYSIS

The data are presented as mean \pm standard deviation (SD). A Tukey's multiple comparisons test was performed on the resulting pillar diameter of pillars printed in different conditions. An unpaired t-test with Welch's correction ($p < 0.05$) was used to compare the positive control with the treated group to test macrophage viability on the 2PP printed material. The analyses were performed using Prism 9.5.1 (GraphPad Software, San Diego, CA, USA).

2

2.3. RESULTS

2.3.1. 3D PRINTING OF PILLAR ARRAYS

The SEM images (**Figure 2.2A**) showed that, at LP = 25 mW, the resulting pillar diameter was $d = 4.89 \pm 1.10 \mu\text{m}$, which is close to the designed value. The actual pillar diameter was larger than the designed one (*i.e.*, $d_d = 5 \mu\text{m}$) for LP = 40 and 50 mW, namely, $d = 7.27 \pm 0.83 \mu\text{m}$ and $d = 8.10 \pm 1.03 \mu\text{m}$, respectively (**Figure 2.2B**). The diameter of the pillars, therefore, increased with the laser power. The differences observed in the printed pillar diameter amongst these 3 different groups printed at 3 different LPs were statistically significant ($p < 0.001$) (**Figure 2.2B**). At LP = 25 mW, all the pillars collapsed. At LP = 40 mW, the tips of the pillars appeared bent and fused, even for the larger values of interspacing. However, at LP = 50 mW, the pillars were bent and fused only for the smaller interspacing values. For the same LP (50 mW), the minimum interspace needed for two adjacent pillars to be printed without fusing was $i = 3.80 \pm 0.68 \mu\text{m}$, which is, on average, 25% smaller than the smallest designed interspace of $i_l = 5 \mu\text{m}$ (**Figure 2.2C**). No minimum interspacing value could be identified for LP = 40 mW and 25 mW since the pillars were either evenly fused for the largest interspacing values or were not printed and appeared collapsed. Altogether, structurally strong and intact pillars of $d = 8.10 \pm 1.03 \mu\text{m}$ with an interspacing of $i = 3.80 \pm 0.68 \mu\text{m}$ were printed at LP = 50 mW. The result of this preliminary study indicated the minimum feature size and interspacing that could be feasibly manufactured for such high aspect ratio geometries and laid the groundwork for the following study on 3D porous structures.

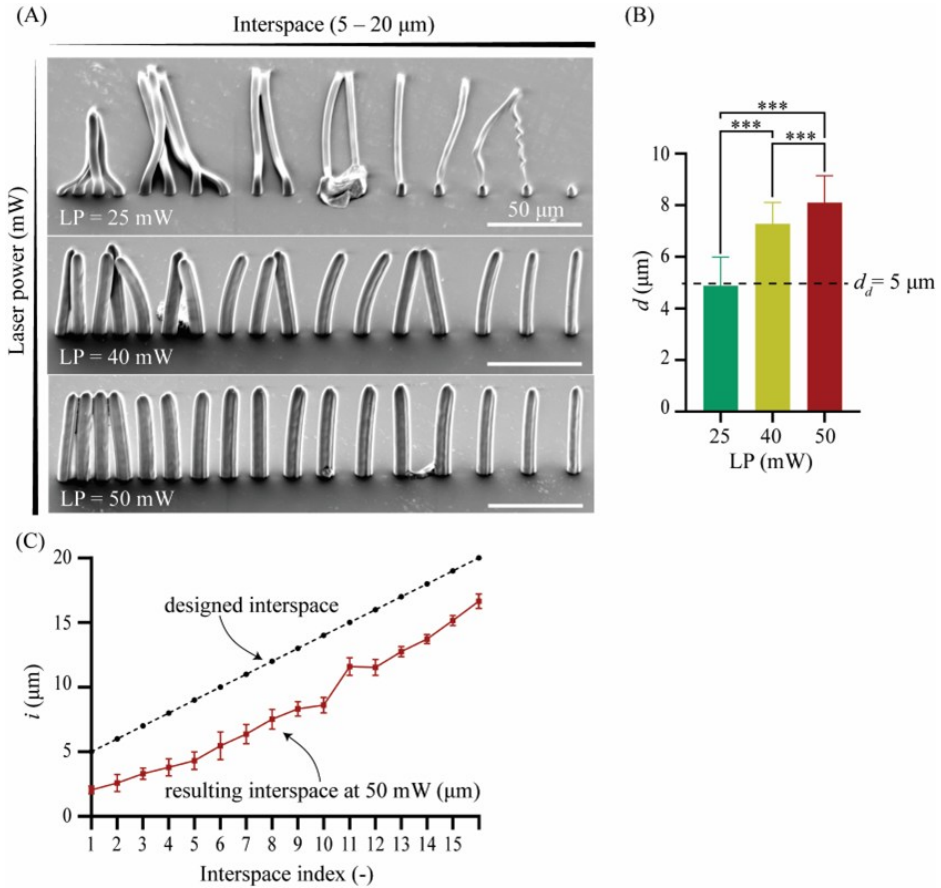


Figure 2.2. (A) The SEM images of the 2PP-printed pillar arrays with a d_d of 5 μm and LP values of 25, 40, and 50 mW (tilt angle = 45°); (B) the quantification of the apparent pillar diameter (d) and comparison with the designed pillar diameter (d_d) (***) ($p < 0.0001$); and (C) quantification of the apparent interspace (i) for an LP of 50 mW and comparison with the design values.

2.3.2. 3D PRINTING OF CUBIC UNIT CELLS AND HOLLOW CYLINDRICAL STRUCTURES

Cubic unit cells with four different strut widths ($s = 20, 30, 40,$ and $50 \mu\text{m}$) and hollow cylindrical units with six different wall thicknesses ($w = 20, 30, 40, 50, 75,$ and $100 \mu\text{m}$) were printed using three different values of the laser power (LP = 25 mW, 40 mW, and 50 mW). The laser power affected the resulting width of the struts and thickness of the walls as well as the general shape of both the cubic unit cells and hollow cylinders (Table 2.3). Cubic unit cells printed at any LP led to smaller s values than the designed ones (Figure 2.3A). In contrast, hollow cylindrical structures with larger LP values

(i.e., LP = 40, 50 mW) exhibited larger w values than the designed ones (Figure 2.3C). The cubic unit cells had resulting strut widths that were 50-70% smaller than designed. The larger the designed strut width, the larger the deviation of the printed width from the designed. The SEM images (Figure 2.3B) also showed that the cubic unit cells exhibited a truncated shape for most printing conditions. However, this set of prints indicated that a cubic unit cell with a designed strut width of at least $s = 50 \mu\text{m}$ could be printed while maintaining the designed shape using the following printing parameters: LP = 50 mW and $v = 150000 \mu\text{m/s}$. For hollow cylindrical structures, on the other hand, the actual dimensions of the printed geometries were 20-30% larger than the design values for LP = 40 mW and 30-40% larger than those designed for LP = 50 mW. For both of these LP values and a designed wall thickness of $w = 100 \mu\text{m}$, wall thickness assessment was not possible due to the excessive and irregular shape of the printed structures (Figure 2.3D). The results of this set of prints revealed that hollow cylindrical specimens yield high-quality prints when printed at LP = 50 mW and $v = 150000 \mu\text{m/s}$. They also maintain their overall shape with an overshoot at the wall thickness but can be printed for apparent wall thicknesses (w) ranging from ~40 to 100 μm .

Table 2.3. Resulting strut width (s) and wall thickness (w) compared to the designed values for the three laser power values (LP) (* symbol represents bad-quality prints). The values are presented as mean \pm standard deviation (μm).

LP (mW)	Designed s (μm)					Designed w (μm)				
	20	30	40	50	20	30	40	50	75	100
	Resulting s (μm)					Resulting w (μm)				
25	*	*	*	25.20 \pm 0.84	*	*	*	*	40.64 \pm 0.0	*
40	*	*	20.39 \pm 1.33	29.65 \pm 1.39	*	36.76 \pm 7.34	52.59 \pm 4.39	63.90 \pm 3.46	97.06 \pm 2.30	*
50	*	17.57 \pm 1.17	26.48 \pm 1.79	35.43 \pm 1.25	*	43.67 \pm 3.71	62.57 \pm 4.02	72.70 \pm 7.47	108.68 \pm 6.13	*

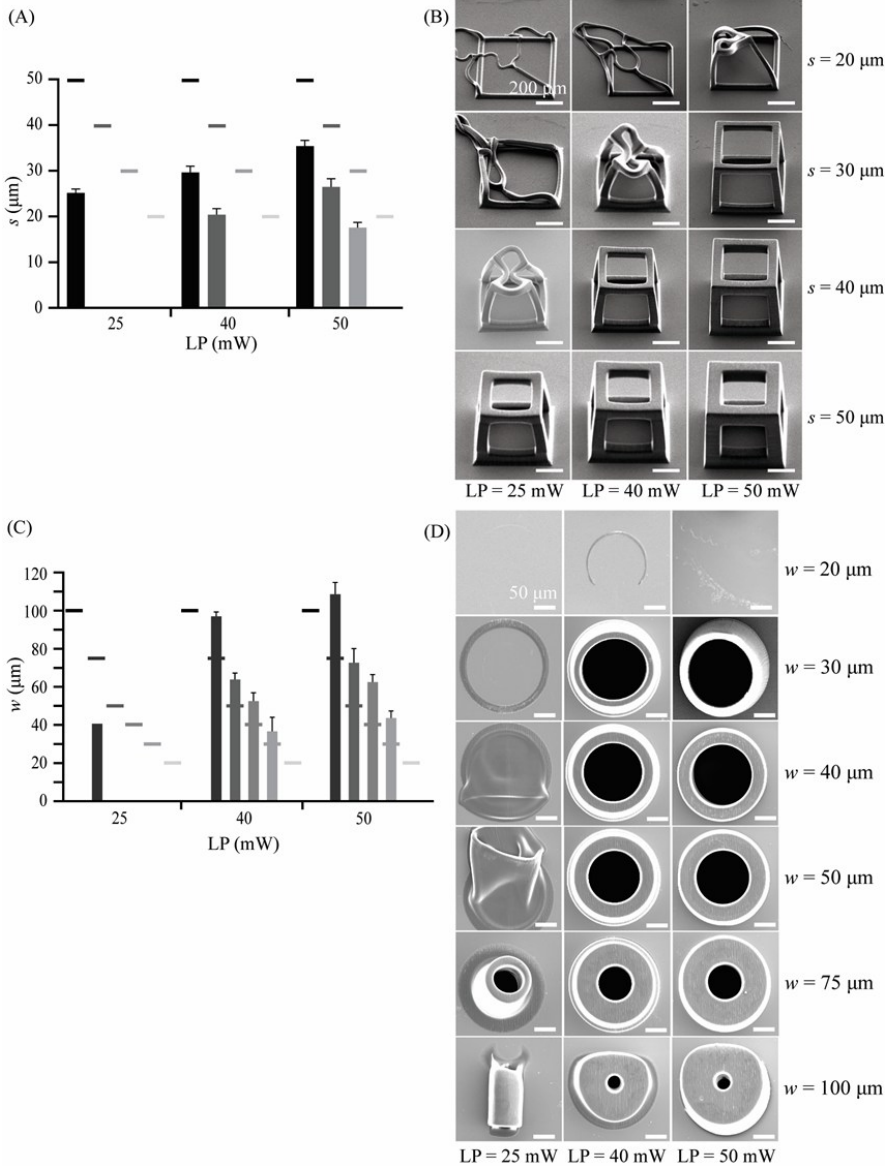


Figure 2.3. (A) The effects of laser power (LP) on the width (s) of the struts of the cubic unit cells presented as mean \pm standard deviation ($n = 3$) and compared to the design values (grayscale short lines). (B) SEM images (40° tilt angle) used for the assessment of the structural integrity of separate cubic unit cells designed with a strut width of $s = 20$ – $50 \mu\text{m}$ for LP = 25, 40, and 50 mW (scale bar is 200 μm). (C) The effects of the laser power (LP) on the wall thickness (w) of the hollow cylindrical structures presented as mean \pm standard deviation ($n = 3$) and compared to the design values (grayscale short lines). (D) SEM images (top view) used for the assessment of the structural integrity of the hollow cylindrical structures designed with a wall thickness of $w = 20$ – $100 \mu\text{m}$ for LP = 25, 40, and 50 mW (scale bar is 50 μm).

2.3.3. 3D PRINTING OF THE COCHLEAR IMPLANTS

The cochlear implants were printed on silicon substrates using two different printing directions, namely, horizontal and vertical. Horizontally printed implants showed signs of defects (**Figure 2.4A**). When printed horizontally, the implants exceeded the printing field of the 10× objective (*i.e.*, \varnothing 1000 μm). Splitting and stitching of the structure in blocks is, therefore, required when preparing the printing job. The defects were located at the stitching sites. Vertically printed samples were printed intact as their base size (*i.e.*, $0.6 \times 0.6 \text{ mm}^2$, $W \times H$) did not exceed the printing field of the 10× objective (**Figure 2.4B**). The vertical printing direction and the processing parameters resulting from the preliminary study (*i.e.*, printing of pillar arrays, cubic unit cells, hollow cylinders) enabled the successful printing of the four different designs of the cochlear implants (*i.e.*, R20, R60, C20, C60) (**Figure 2.4B**).

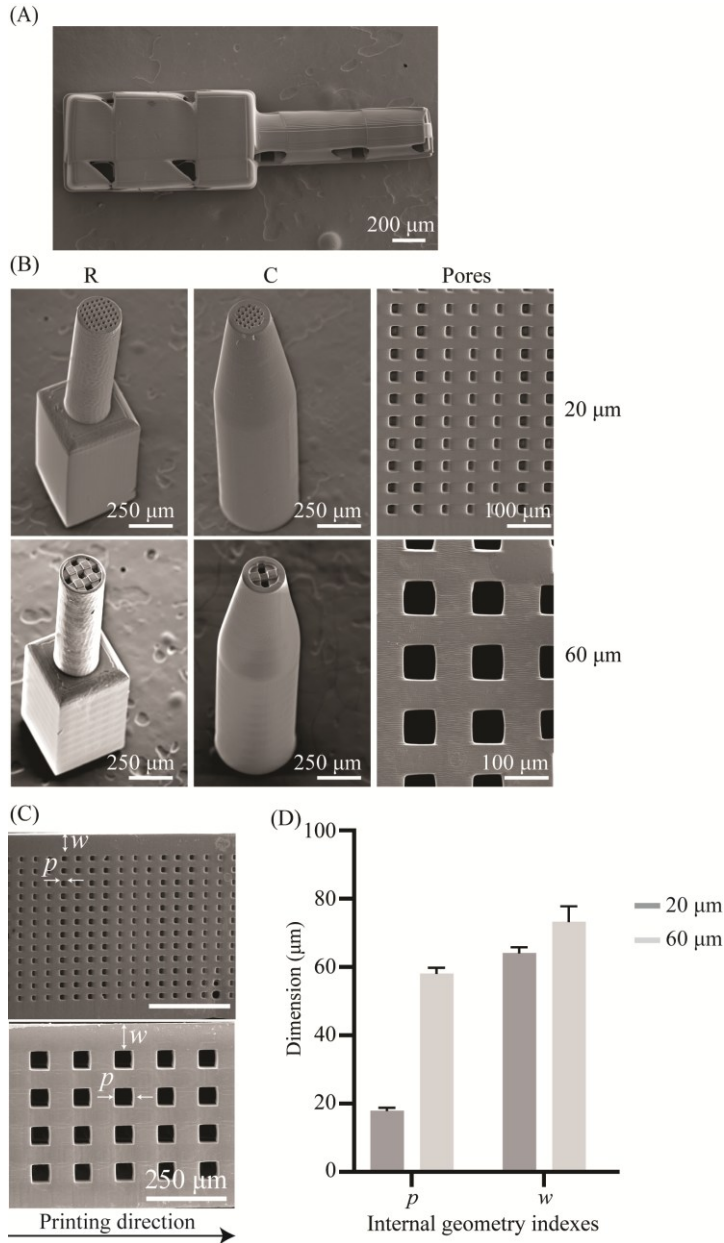


Figure 2.4. (A) A SEM image of a horizontally 2PP-printed R-type cochlear implant (top view); (B) SEM images of 2PP-printed porous cochlear implants (tilt angle = 30°) and their internal porous structure and pore size; (C) SEM images of the interconnected pore network with pore sizes of 20 μm and 60 μm, where p is the pore size and w is the wall thickness of the implant; and (D) quantification of the pore size (p) and wall thickness (w). The values are presented as mean ± standard deviation.

2.3.4. MORPHOLOGICAL CHARACTERIZATION

Assessment of the geometry of both interconnected pore networks (*i.e.*, 20 μm and 60 μm) using SEM yielded pore sizes of $p = 17.88 \pm 0.95 \mu\text{m}$ and $p = 58.15 \pm 1.62 \mu\text{m}$, respectively. The wall thickness was also assessed for all the implant types and was $w = 64.08 \pm 1.76 \mu\text{m}$ for the implant types R20 and C20 and $w = 72.50 \pm 3.38 \mu\text{m}$ for the implant types R60 and C60 (**Table 2.4**). The calculated porosities φ based on **Eq. 2.1** for the different cochlear implants were $\varphi_{R60}=52\%$ and $\varphi_{R20}=46\%$ for the R-type implants and $\varphi_{C60}=\varphi_{C20}=50\%$ for the C-type implants.

Table 2.4. Morphological parameters of the internal porous network (p : pore size) and wall thickness (w) of the cochlear implants. The values are presented as mean \pm standard deviation (μm).

Parameter	Pore Type	
	20	60
p	17.88 ± 0.95	58.15 ± 1.62
w	64.08 ± 1.76	72.50 ± 3.38

2.3.5. SURFACE TOPOGRAPHY

Two surface roughness parameters were measured for the samples used in this study. The average roughness parameter (R_a) was measured over a line profile, whereas the areal average surface roughness (S_a) was measured over a surface. The areal average of the surface roughness of the flat pedestals was $S_a^P = 0.73 \pm 0.5 \mu\text{m}$, whereas their average surface roughness was $R_a^P = 0.09 \pm 0.005 \mu\text{m}$. The areal average surface roughness of the implants printed horizontally was $S_a^H = 0.76 \pm 0.08 \mu\text{m}$, while their average surface roughness was $R_a^H = 0.11 \pm 0.01 \mu\text{m}$. The areal average of the surface roughness of the implants printed vertically was $S_a^V = 1.67 \pm 0.24 \mu\text{m}$ with an average surface roughness of $R_a^V = 0.15 \pm 0.01 \mu\text{m}$. The morphology of the vertically printed implants also seems to reveal the layer structure of the 2PP process (**Figure 2.5A**).

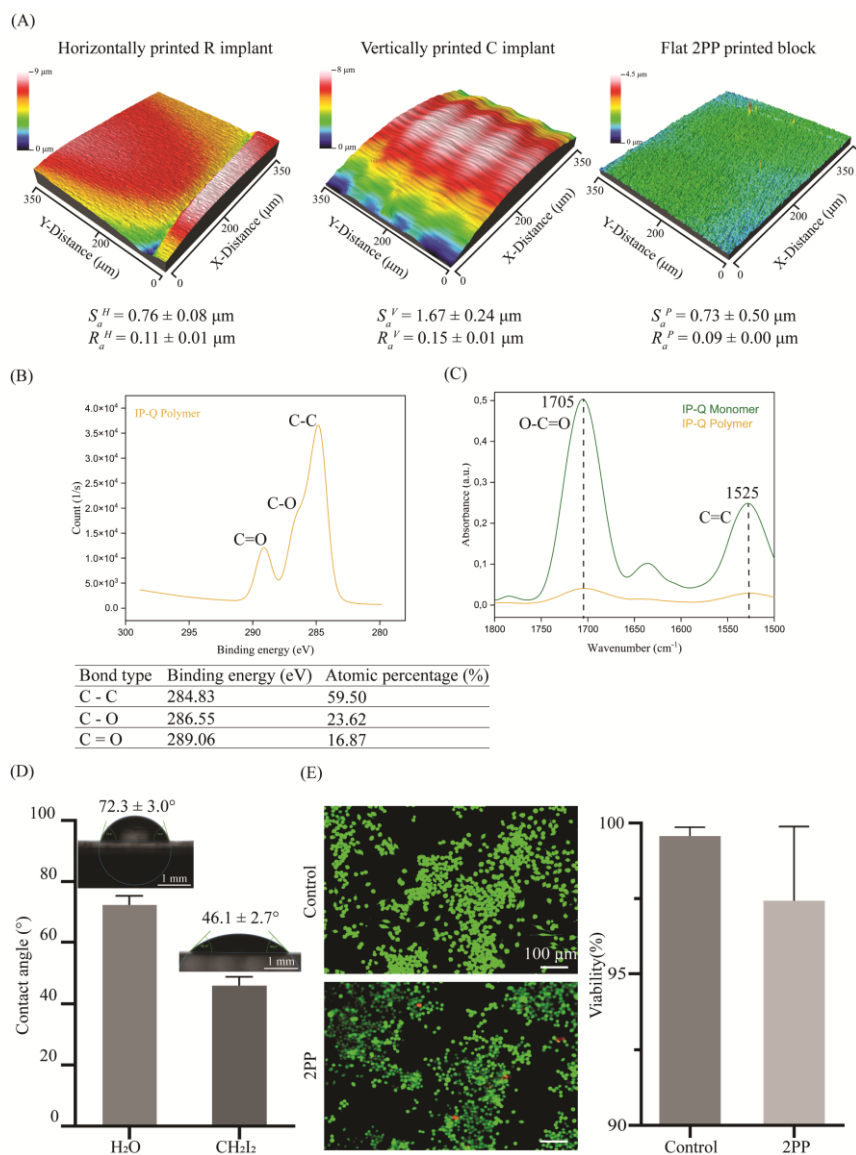


Figure 2.5. (A) The surface roughness measurements (S_a , R_a) for horizontally and vertically printed implants as well as flat 2PP-printed blocks; (B) XPS spectra of C 1s peaks in IP-Q after polymerization, and the binding energy and atomic percentage of C 1s series in the 2P-printed IP-Q specimens, (C) FTIR spectra in the ATR mode of the IP-Q photoresist (yellow) and polymer after 2PP (green); (D) contact angle measurements on flat 2PP-printed IP-Q blocks for water and diiodomethane with the corresponding pictures of the shape of the droplets (scale bar is 1 mm), and the contact angle is presented as mean \pm standard deviation; and (E) the live/dead staining of J774A.1 macrophages after 48 h of culture on control (*i.e.*, well plate) and on 2PP-printed IP-Q flat block specimens (live: green, red: dead) and the quantification of the macrophage viability (%) for the control and the 2PP-printed specimens (scale bar is 100 μm).

2.3.6. CHEMICAL CHARACTERIZATION

Chemical characterization was performed to indirectly assess the efficiency of the 2PP process and to confirm the printing quality of the structures by evaluating changes in chemical bonding associated with monomer conversion. Peaks with binding energies of 284 eV, 286 eV, and 289 eV are in agreement with C-C, C=C, and C-O bonds, respectively, that have been identified in the XPS spectra of the block samples (**Figure 2.5B**). These peaks verify the presence of methacrylate structures [46] in the photocurable resin IP-Q. In the FTIR spectra, a difference in the peak intensity of the carboxyl group (1705 cm^{-1}) and carbon double bond (1525 cm^{-1}) was observed before and after printing (**Figure 2.5C**). More specifically, the intensity of the bonds decreased after printing, indicating double carbon bond depletion as a result of polymerization. The decreases in the intensity of those peaks were $\approx 88\%$ for the carbon double bond at 1525 cm^{-1} and $\approx 92\%$ for the carboxyl group at 1705 cm^{-1} .

2.3.7. WETTABILITY AND SURFACE FREE ENERGY

Water contact angle measurements ($n = 5$) revealed an average water contact angle of $CA_W = 72.3 \pm 3.0^\circ$ and an average contact angle for diiodomethane of $CA_D = 46.1 \pm 2.7^\circ$ (**Figure 2.5D**). According to the OWRK model and using the aforementioned contact angle measurements, the total surface free energy was calculated to be $SFE = 38.1 \pm 2.3\text{ mN/m}$, with a polar component of $\sigma_S^P = 1.7 \pm 1.1\text{ mN/m}$ and a dispersive component of $\sigma_S^D = 36.4 \pm 1.2\text{ mN/m}$.

2.3.8. CYTOTOXICITY

The live/dead assay using J774A.1 macrophages cultured on the block samples showed high (>95%) viability of the cells after 48 h of culture (**Figure 2.5E**). No statistically significant difference in macrophage viability was observed between the control and the test group ($p = 0.1230$).

2.4. DISCUSSION

We aimed to design, fabricate, and characterize a novel DDS for the inner ear. The results demonstrate the feasibility of using the 2PP process for printing implants with anatomically relevant sizes for the human inner ear. Furthermore, the implants

featured internal porous structures to enable the loading of drugs and their controlled release.

2.4.1. IMPLANT DESIGN AND FABRICATION

The fabrication of large-scale structures involves choosing the correct values for several parameters, such as the laser power and orientation angle. An initial investigation of the effects of laser power on the fabrication of pillars with a high aspect ratio (*i.e.*, AR = 16) showed that the height, diameter, and structural integrity of the pillars were strongly dependent on the laser power. The minimum clearance between high-quality pillars with an apparent diameter of $\approx 8 \mu\text{m}$ was $3.80 \pm 0.68 \mu\text{m}$, indicating the highest resolution possible with the setup and material used (*i.e.*, $10\times$ objective, IP-Q resin), which is the only possible combination for the fabrication of large 3D structures using the Nanoscribe system. Using the same configuration, the cubic unit cells that were designed and fabricated to resemble the single pore structure of the implants demonstrated a much smaller strut width ($\sim 35 \mu\text{m}$), even for the highest quality prints compared to the designed one ($\sim 50 \mu\text{m}$). The cylindrical hollow units appeared deformed when the wall thickness was $100 \mu\text{m}$, even for the highest laser power, due to the large volumetric contraction stress compared to structures with a wall thickness $< 100 \mu\text{m}$. These results indicate a direct relationship between the printing conditions and the size and strength of the resulting structure. Generally, low laser power results in a low polymerization rate and subsequently in thinner and more fragile structures than higher laser power [47]. A linear relationship has been recently proposed to describe the correlation between the laser power and the thickness of the resulting structure [48]. Moreover, the resulting shape and size of the printed structure are influenced by the shrinkage and buckling that occurs in the post-processing phase [49,50]. In addition, shape and size inaccuracies between the designed and the printed test structures can also be attributed to errors in the stage movements, errors in the tessellated file formats of the designs, and structural deformations of the 2PP-printed structures [51]. The design conceptualization, realization, and 2PP printing of the cochlear implants were based on the results of our preliminary study, in which a wide range of test structures was printed. More specifically, the interconnected porous network was designed with a pore size of 60

μm based on the printing results of the cubic unit cells. The wall thickness was designed to be $50\ \mu\text{m}$ based on the printing results of the hollow cylinders. Finally, the implants were printed vertically so that no stitching would be necessary. In contrast to the test structures, the shape and dimensions of the printed implants did not substantially deviate from their designs. More specifically, the pore size deviated only 10% from the intended $60\ \mu\text{m}$. Additionally, the total length and width of the implants were 10% smaller than the designed geometry. Implants with a pore size of $20\ \mu\text{m}$ were successfully fabricated with similar geometrical deviations from their designs. The difference between the printing of the test structures and the implants can be explained by the residual polymerization, or proximity effect, that occurs in the implants being printed [52]. To put this concept in perspective, for a structure with a height of $240\ \mu\text{m}$ and a slicing distance of $5\ \mu\text{m}$, 48 layers of material are deposited on top of each other. For a structure that is 10 times larger, the number of layers increases accordingly. The resin, therefore, undergoes many more cycles of exposure to the laser beam, and the heat-initiated polymerization contributes greatly to the final dimensions of the printed structures [53]. Several previous studies have demonstrated that the 2PP process allows for the printing of 3D porous scaffolds with controlled porosity and high precision at the micron and submicron scales [38,54]. In this study, we aimed to incorporate controlled microporosity within millimeter-sized scaffolds suitable for applications as functional cochlear implants. As with the majority of studies, the design of the current study is subject to limitations. The study mainly focuses on the 3D printing feasibility of cochlear implants with an internal porous network consisting of cubic unit cells, and no other type of network has been included. It is known that natural materials develop complex architectures to adapt and function in their environment, with porosity being a crucial factor as it enables filtration, diffusion, and increased permeability for nutrient exchange [55]. The added functional value of porosity has also long been explored in the case of porous scaffolds for various applications [56-58]. The use of porous structures specifically for loading and local release of drugs without any additional material/drug carrier is, however, relatively underexplored. Microneedles have been investigated for transdermal delivery of drugs, proving the suitability of such a system [59,60]. The

uniqueness of our system lies in the fact that the porous device is printed without the drugs; thus, the printing process is not limited by the drug type or phase. This aspect offers the possibility of creating a versatile structure to be combined with different types of pharmaceuticals and could subsequently be used for different pathologies. It would, therefore, be relevant to investigate the potential of the proposed porosity to control drug delivery and to consider the possibility of another pore shape for the same application. Last, it is important to mention that the fabrication of porous structures with pores in the range of 20–60 μm using the same printing parameters and, thus, within a single step and without block splitting or stitching required could be used to create implants with a combination of different pore sizes to achieve better controllability of the drug release.

2.4.2. CHARACTERIZATION

The FTIR and XPS results can only qualitatively indicate the degree of conversion of IP-Q. Nevertheless, they verify the methacrylate character of the resin and the change in the carboxylic and double carbon bonds after polymerization. According to the existing literature, the extent of polymerization can be evaluated when quantifying the transformation of double-carbon bonds to single-carbon bonds with respect to the carboxyl group [61]. In our case, both of the peaks indicated the carbon double bond and the carboxyl group decreased in intensity, indicating the involvement of the carboxyl group in the polymerization process. This characteristic is unique to IP-Q compared to other photoresists [62–64] and might be related to the fact that IP-Q has been designed for high-speed fabrication. To our knowledge, the polymerization mechanism of the IP-Q material has not yet been fully unraveled. However, the findings of the current study can complement the existing characterization [65]. The contact angle measurements and the resulting SFE indicate a partially hydrophilic character for the 2PP-printed IP-Q. The average surface roughness, R_a , for horizontally and vertically printed implants and flat blocks was in the range of 90–150 nm. The areal (3D) surface roughness, S_a , for the corresponding surfaces was much larger, ranging between 0.730 and 1.670 μm . The difference between those two topographical parameters is related to the fact that for the calculation of S_a , the overall surface is considered, which explains the higher S_a of the C implant types compared to

the R implant types. The orientation angle also affected the surface roughness. The higher surface roughness of the vertically printed implant compared to the horizontally printed implant is due to the anisotropic resolution and spatial arrangement of the voxels. The shape of the voxel in the 2PP process resembles an ellipsoid with a higher lateral spatial resolution than the axial resolution. The higher surface roughness at lower orientation angles can also be attributed to the larger slicing distance as compared to the hatching distance. In general, the voxel size and voxel overlap greatly determine the surface finish of a structure, with smaller voxel sizes and a higher degree of overlapping resulting in an improved surface finish. However, the improved surface finish comes at the expense of increased processing and printing times.

Macrophage viability was comparable between the control polystyrene well plate and the 2PP-printed surfaces, and no statistically significant difference was observed between the two groups. Macrophages survived and proliferated similarly on polystyrene surfaces with a water contact angle of $\sim 55^\circ$ [66] and on the 2PP surfaces with a water contact angle of $\sim 72^\circ$. This indicates the good cytocompatibility of the applied resin and confirms the choice of the resin for the fabrication of such types of implants.

2.4.3. OUTLOOK AND CHALLENGES

Hearing preservation through local delivery of drugs, such as antibiotics and steroids [67-69], to the cochlea has been recognized as a potentially efficient treatment strategy. However, it remains challenging to locally deliver drugs to the cochlea. A variety of different systems, such as micropumps [67,70], cochlear electrode arrays [71,72], drug-loaded silicone-based ear implants [12], and drug-loaded PLGA nanoparticles [73], have been developed to achieve sustained, controlled delivery and enhance drug bioavailability in the cochlea. The incorporation of porous structures in 3D-printed DDS to target different pathologies and organs, such as the skin, brain, breast, and cartilage, has been researched by different groups. The structure and dimensions of the implants, on the one hand, and the properties of drugs, on the other hand, influence the release kinetics of drugs both separately and in combination with each other [74]. A general observation is that larger implant surfaces contribute to

faster drug release [74]. It has been reported that drug release is affected by the ratio of the pore size of a porous carrier to the size of the drug molecules [75,76]. Moreover, drug loading and release are influenced by the affinity of the carrier and the drug [29]. However, not much information is available regarding the combination of these two effects in the context of cochlear implants. Future research should, therefore, be directed at understanding the interrelations among the 3D printed materials, porous structures of anatomically relevant sizes, and the properties of the drugs that are most likely to be used in conjunction with cochlear implants. Furthermore, the chemical and mechanical properties of such cochlear implants need to be characterized as one of the first attempts to investigate their suitability for application as a DDS.

2.5. CONCLUSION

In this study, we successfully designed and fabricated cochlear implants with internal microporous structures using the 2PP technique. Our findings show that the 2PP process is suitable for reliably producing implants with both a rectangular and a cylindrical profile featuring internal square pores of 20 μm and 60 μm . A parametric study on different processing parameters enabled us to identify the settings to achieve the intended feature sizes, surface finish, and structural stability. Moreover, the material used for the fabrication of the cochlear implants (IP-Q) showed a high degree of polymerization and good cytocompatibility for macrophages. Taken together, we demonstrated the feasibility of creating anatomically relevant cochlear implants with precisely controlled and tunable internal microporosity, indicating their potential for localized drug delivery to the human cochlea for personalized treatment of hearing loss.

REFERENCES

- [1] Lin, Q.; Guo, Q.; Zhu, M.; Zhang, J.; Chen, B.; Wu, T.; Jiang, W.; Tang, W. Application of Nanomedicine in Inner Ear Diseases. *Front. Bioeng. Biotechnol.* 2021, 9, 809443. <https://doi.org/10.3389/fbioe.2021.809443>.
- [2] World Health Organization. World Report on Hearing. Sensory Functions, Disability and Rehabilitation (SDR). World Health Organization: Geneva, Switzerland, 2021. <https://www.who.int/publications/i/item/9789240020481>.
- [3] Laureyns, M.; Bisgaard, N.; Bobeldijk, M.; Zimmer, D. Getting the Numbers Right on Hearing Loss, Hearing Care and Hearing Aid Use in Europe Wide Strategy Joint AEA, EFHOH, EHIMA Report; EIMA: Brussels, Belgium, 2020. https://hearingloss_care_europ/efhoh
- [4] Ross, F.; Wohllebe, A. Evaluating the Service Quality of Mobile Health Versus Clinic Based Intervention in Hearing Healthcare. A Comparative Study. *Int. J. Interact. Mob. Technol.* 2021, 15, 21-32. <https://doi.org/10.3991/ijim.v15i10.21725>.
- [5] Naples, J.G.; Ruckenstein, M.J. Cochlear Implant. *Otolaryngol. Clin. North. Am.* 2020, 53, 87-102. <https://doi.org/10.1016/j.otc.2019.09.004>.
- [6] Chakravorti, S.; Noble, J.H.; Gifford, R.H.; Dawant, B.M.; O'Connell, B.P.; Wang, J.; Labadie, R.F. Further Evidence of the Relationship Between Cochlear Implant Electrode Positioning and Hearing Outcomes. *Otol. Neurotol.* 2019, 40, 617-624. [10.1097/MAO.0000000000002204](https://doi.org/10.1097/MAO.0000000000002204).
- [7] Altissimi, G.; Colizza, A.; Cianfrone, G.; de Vincentiis, M.; Greco, A.; Taurone, S.; Musacchio, A.; Ciofalo, A.; Turchetta, R.; Angeletti, D.; et al. Drugs Inducing Hearing Loss, Tinnitus, Dizziness and Vertigo: An Updated Guide. *Eur. Rev. Med. Pharmacol. Sci.* 2020, 24, 7946-7952. https://doi.org/10.26355/eurrev_202008_22477.
- [8] Piu, F.; Bishop, K.M. Local Drug Delivery for the Treatment of Neurotology Disorders. *Front. Cell. Neurosci.* 2019, 13, 238. <https://doi.org/10.3389/fncel.2019.00238>.
- [9] McCall, A.A.; Swan, E.E.; Borenstein, J.T.; Sewell, W.F.; Kujawa, S.G.; McKenna, M.J. Drug Delivery for Treatment of Inner Ear Disease: Current State of Knowledge. *Ear Hear.* 2010, 31, 156-165. <https://doi.org/10.1097/AUD.0b013e3181c351f2>.
- [10] Carvalho; Gerard, J.; Anil, K. Lalwani The Effect of Cochleostomy and Intracochlear Infusion on Auditory Brain Stem Response Threshold in the Guinea Pig. *Am. J. Otol.* 1999, 20, 87-90. <https://pubmed.ncbi.nlm.nih.gov/9918180/>
- [11] Krenzlin, S.; Vincent, C.; Munzke, L.; Gnansia, D.; Siepmann, J.; Siepmann, F. Predictability of drug release from cochlear implants. *J. Control. Release* 2012, 159, 60-68. <https://doi.org/10.1016/j.jconrel.2011.12.032>.

- [12] Gehrke, M.; Sircoglou, J.; Gnansia, D.; Tourrel, G.; Willart, J.F.; Danede, F.; Lacante, E.; Vincent, C.; Siepmann, F.; Siepmann, J. Ear Cubes for local controlled drug delivery to the inner ear. *Int. J. Pharm.* 2016, 509, 85–94. <https://doi.org/10.1016/j.ijpharm.2016.04.003>.
- [13] Lehner, E.; Gündel, D.; Liebau, A.; Plontke, S.; Mäder, K. Intracochlear PLGA Based Implants for Dexamethasone Release: Challenges and Solutions. *Int. J. Pharm. X* 2019, 1, 100015. <https://doi.org/10.1016/j.ijpx.2019.100015>.
- [14] Wachowiak, S.; Danede, F.; Willart, J.F.; Siepmann, F.; Siepmann, J.; Hamoudi, M. PLGA Implants for Controlled Dexamethasone Delivery: Impact of the Polymer Chemistry. *J. Drug Deliv. Sci. Technol.* 2023, 86, 104648. <https://doi.org/10.1016/j.jddst.2023.104648>.
- [15] Rongthong, T.; Qnouch, A.; Gehrke, M.M.; Danede, F.; Willart, J.F.; de Oliveira, P.F.M.; Paccou, L.; Tourrel, G.; Stahl, P.; Verin, J.; et al. Long Term Behavior of Dexamethasone-Loaded Cochlear Implants: *In Vitro* & *in Vivo*. *Int. J. Pharm. X* 2022, 4, 100141. <https://doi.org/10.1016/j.ijpx.2022.100141>.
- [16] Rongthong, T.; Qnouch, A.; Maue Gehrke, M.; Paccou, L.; Oliveira, P.; Danede, F.; Verin, J.; Vincent, C.; Willart, J.-F.; Siepmann, F.; et al. Silicone Matrices for Controlled Dexamethasone Release: Toward a Better Understanding of the Underlying Mass Transport Mechanisms. *Regen. Biomater.* 2023, 10, rbad008. <https://doi.org/10.1093/rb/rbad008>.
- [17] Seoane-Viaño, I.; Trenfield, S.J.; Basit, A.W.; Goyanes, A. Translating 3D Printed Pharmaceuticals: From Hype to Real-World Clinical Applications. *Adv. Drug Deliv. Rev.* 2021, 174, 553–575. <https://doi.org/10.1016/j.addr.2021.05.003>.
- [18] Wu, C.; Luo, Y.; Cuniberti, G.; Xiao, Y.; Gelinsky, M. Three-Dimensional Printing of Hierarchical and Tough Mesoporous Bioactive Glass Scaffolds with a Controllable Pore Architecture, Excellent Mechanical Strength and Mineralization Ability. *Acta Biomater.* 2011, 7, 2644–2650. <https://doi.org/10.1016/j.actbio.2011.03.009>
- [19] Zhu, M.; Li, K.; Zhu, Y.; Zhang, J.; Ye, X. 3D-Printed Hierarchical Scaffold for Localized Isoniazid/Rifampin Drug Delivery and Osteoarticular Tuberculosis Therapy. *Acta Biomater.* 2015, 16, 145–155. <https://doi.org/10.1016/j.actbio.2015.01.034>.
- [20] Narayan, R.J.; Doraiswamy, A.; Chrisey, D.B.; Chichkov, B.N. Medical Prototyping Using Two Photon Polymerization. *Mater. Today* 2010, 13, 42–48. [https://doi.org/10.1016/S1369-7021\(10\)70223-6](https://doi.org/10.1016/S1369-7021(10)70223-6).
- [21] Bassand, C.; Benabed, L.; Charlon, S.; Verin, J.; Freitag, J.; Siepmann, F.; Soulestin, J.; Siepmann, J. 3D Printed PLGA Implants: APF DDM vs. FDM. *J. Control. Release* 2023, 353, 864–874. <https://doi.org/10.1016/j.jconrel.2022.11.052>.
- [22] Goyanes, A.; Madla, C.M.; Umerji, A.; Duran Piñeiro, G.; Giraldez Montero, J.M.; Lamas Diaz, M.J.; Gonzalez Barcia, M.; Taherali, F.; Sánchez-Pintos, P.; Couce,

- M.-L.; et al. Automated Therapy Preparation of Isoleucine Formulations Using 3D Printing for the Treatment of MSUD: First Single-Centre, Prospective, Crossover Study in Patients. *Int. J. Pharm.* 2019, 567, 118497. <https://doi.org/10.1016/j.ijpharm.2019.118497>.
- [23] Januskaite, P.; Xu, X.; Ranmal, S.R.; Gaisford, S.; Basit, A.W.; Tuleu, C.; Goyanes, A. I Spy with My Little Eye: A Paediatric Visual Preferences Survey of 3D Printed Tablets. *Pharmaceutics* 2020, 12, 1100. <https://doi.org/10.3390/pharmaceutics12111100>.
- [24] Goyanes, A.; Scarpa, M.; Kamlow, M.; Gaisford, S.; Basit, A.W.; Orlu, M. Patient Acceptability of 3D Printed Medicines. *Int. J. Pharm.* 2017, 530, 71-78. <https://doi.org/10.1016/j.ijpharm.2017.07.064>.
- [25] Fina, F.; Goyanes, A.; Gaisford, S.; Basit, A.W. Selective Laser Sintering (SLS) 3D Printing of Medicines. *Int. J. Pharm.* 2017, 529, 285-293. <https://doi.org/10.1016/j.ijpharm.2017.06.082>.
- [26] Tan, Y.J.N.; Yong, W.P.; Kochhar, J.S.; Khanolkar, J.; Yao, X.; Sun, Y.; Ao, C.K.; Soh, S. On-Demand Fully Customizable Drug Tablets via 3D Printing Technology for Personalized Medicine. *J. Control. Release* 2020, 322, 42-52. <https://doi.org/10.1016/j.jconrel.2020.02.046>.
- [27] Wang, Y.; Müllertz, A.; Rantanen, J. Additive Manufacturing of Solid Products for Oral Drug Delivery Using Binder Jetting Three-Dimensional Printing. *AAPS PharmSciTech* 2022, 23, 196. <https://doi.org/10.1208/s12249-022-02321-w>.
- [28] Dong, M.; Wang, X.; Chen, X.-Z.; Mushtaq, F.; Deng, S.; Zhu, C.; Torlakcik, H.; Terzopoulou, A.; Qin, X.-H.; Xiao, X.; et al. 3D-Printed Soft Magnetoelectric Microswimmers for Delivery and Differentiation of Neuron-Like Cells. *Adv. Funct. Mater.* 2020, 30, 1910323. <https://doi.org/10.1002/adfm.201910323>.
- [29] Bozuyuk, U.; Yasa, O.; Yasa, I.C.; Ceylan, H.; Kizilel, S.; Sitti, M. Light-Triggered Drug Release from 3D-Printed Magnetic Chitosan Microswimmers. *ACS Nano* 2018, 12, 9617-9625. <https://doi.org/10.1021/acsnano.8b05997>.
- [30] Faraji Rad, Z.; Prewett, P.D.; Davies, G.J. High-Resolution Two-Photon Polymerization: The Most Versatile Technique for the Fabrication of Microneedle Arrays. *Microsyst. Nanoeng.* 2021, 7, 71. <https://doi.org/10.1038/s41378-021-00298-3>.
- [31] He, G.S.; Tan, L.-S.; Zheng, Q.; Prasad, P.N. Multiphoton Absorbing Materials: Molecular Designs, Characterizations, and Applications. *Chem. Rev.* 2008, 108, 1245-1330. <https://doi.org/10.1021/cr050054x>.
- [32] He, G.S.; Xu, G.C.; Prasad, P.N.; Reinhardt, B.A.; Bhatt, J.C.; Dillard, A.G. Two-Photon Absorption and Optical-Limiting Properties of Novel Organic Compounds. *Opt. Lett.* 1995, 20, 435-437. <https://doi.org/10.1364/OL.20.000435>.

- [33] Tan, D.; Li, Y.; Qi, F.; Yang, H.; Gong, Q.; Dong, X.; Duan, X. Reduction in Feature Size of Two-Photon Polymerization Using SCR500. *Appl. Phys. Lett.* 2007, 90, 71106. <https://doi.org/10.1063/1.2535504>.
- [34] Geng, Q.; Wang, D.; Chen, P.; Chen, S.-C. Ultrafast Multi-Focus 3-D Nano-Fabrication Based on Two-Photon Polymerization. *Nat. Commun.* 2019, 10, 2179. <https://doi.org/10.1038/s41467-019-10249-2>.
- [35] Stichel, T.; Hecht, B.; Houbertz, R.; Sextl, G. Two-Photon Polymerization as Method for the Fabrication of Large Scale Biomedical Scaffold Applications. *J. Laser Micro/Nanoeng.* 2010, 5, 209-212. <https://doi.org/10.2961/jl.2010.03.0005>.
- [36] Mckee, S.; Lutey, A.; Sciancalepore, C.; Poli, F.; Selli, S.; Cucinotta, A. Microfabrication of Polymer Microneedle Arrays Using Two-Photon Polymerization. *J. Photochem. Photobiol. B* 2022, 229, 112424. <https://doi.org/10.1016/j.jphotobiol.2022.112424>.
- [37] Weiss, T.; Hildebrand, G.; Schade, R.; Liefeth, K. Two-Photon Polymerization for Microfabrication of Three-Dimensional Scaffolds for Tissue Engineering Application. *Eng. Life Sci.* 2009, 9, 384-390. <https://doi.org/10.1002/elsc.200900002>.
- [38] Sharaf, A.; Roos, B.; Timmerman, R.; Kremers, G.-J.; Bajramovic, J.J.; Accardo, A. Two-Photon Polymerization of 2.5D and 3D Microstructures Fostering a Ramified Resting Phenotype in Primary Microglia. *Front. Bioeng. Biotechnol.* 2022, 10, 926642. <https://doi.org/10.3389/fbioe.2022.926642>.
- [39] Rananaware, P.; Brahmkhatria, V.P.; Dasgupta, D.; Patel, A. Functionalized Mesoporous Silica for Drug Delivery of Poorly Soluble Polyphenols: Synthesis, Characterization, and Antimicrobial Action. *J. Solid State Chem.* 2023, 326, 124214. <https://doi.org/10.1016/j.jssc.2023.124214>.
- [40] Yang, Y.; Qiao, X.; Huang, R.; Chen, H.; Shi, X.; Wang, J.; Tan, W.; Tan, Z. E-Jet 3D Printed Drug Delivery Implants to Inhibit Growth and Metastasis of Orthotopic Breast Cancer. *Biomaterials* 2020, 230, 119618. <https://doi.org/10.1016/j.biomaterials.2019.119618>.
- [41] Annamalai, M.; Gopinadhan, K.; Han, S.A.; Saha, S.; Park, H.J.; Cho, E.B.; Kumar, B.; Patra, A.; Kim, S.-W.; Venkatesan, T. Surface Energy and Wettability of van Der Waals Structures. *Nanoscale* 2016, 8, 5764-5770. <https://doi.org/10.1039/C5NR06705G>.
- [42] Kaelble, D.H. Dispersion-Polar Surface Tension Properties of Organic Solids. *J. Adhes.* 1970, 2, 66-81. <https://doi.org/10.1080/0021846708544582>.
- [43] Owens, D.K.; Wendt, R.C. Estimation of the Surface Free Energy of Polymers. *J. Appl. Polym. Sci.* 1969, 13, 1741-1747. <https://doi.org/10.1002/app.1969.070130815>.

- [44] Rabel, W. Einige Aspekte Der Benetzungstheorie Und Ihre Anwendung Auf Die Untersuchung Und Veränderung Der Oberflächeneigenschaften von Polymeren. *Farbe Und Lack* 1971, 77, 997-1005.
- [45] Schneider, C.A.; Rasband, W.S.; Eliceiri, K.W. NIH Image to ImageJ: 25 Years of Image Analysis. *Nat. Methods* 2012, 9, 671--675. <https://doi.org/10.1038/nmeth.2089>
- [46] Abdel-Fattah, E. Surface Activation of Poly(Methyl Methacrylate) with Atmospheric Pressure Ar + H₂O Plasma. *Coatings* 2019, 9, 228. <https://doi.org/10.3390/coatings9040228>
- [47] Hu, Q.; Rance, G.A.; Trindade, G.F.; Pervan, D.; Jiang, L.; Foerster, A.; Turyanska, L.; Tuck, C.; Irvine, D.J.; Hague, R.; et al. The Influence of Printing Parameters on Multi-Material Two-Photon Polymerisation Based Micro Additive Manufacturing. *Addit. Manuf.* 2022, 51, 102575. <https://doi.org/10.1016/j.addma.2021.102575>.
- [48] Zhang, S.; Li, S.; Wan, X.; Li, N.; Li, J.; Yin, Q.; Zhang, L. High-Efficiency Two-Photon Polymerization Initiators Based on Coumarin Derivatives for Additive Manufacturing with Sub-Wavelength Resolution. *Mater. Today Chem.* 2023, 30, 101599. <https://doi.org/10.1016/j.mtchem.2023.101599>.
- [49] Davidson, C.L.; Feilzer, A.J. Polymerization Shrinkage and Polymerization Shrinkage Stress in Polymer-Based Restoratives. *J. Dent.* 1997, 25, 435-440. [https://doi.org/10.1016/S0300-5712\(96\)00063-2](https://doi.org/10.1016/S0300-5712(96)00063-2).
- [50] Kamranikia, K.; Dominici, S.; Keller, M.; Kube, N.; Mougin, K.; Spangenberg, A. Very High-Aspect-Ratio Polymeric Micropillars Made by Two-Photon Polymerization. *Micromachines* 2023, 14, 1602. <https://doi.org/10.3390/mi14081602>.
- [51] Zhou, X.; Hou, Y.; Lin, J. A Review on the Processing Accuracy of Two-Photon Polymerization. *AIP Adv.* 2015, 5, 030701. <https://doi.org/10.1063/1.4916886>.
- [52] Kim, H.; Pingali, R.; Saha, S.K. Rapid Printing of Nanoporous 3D Structures by Overcoming the Proximity Effects in Projection Two-Photon Lithography. *Virtual Phys. Prototyp.* 2023, 18, e2230979. <https://doi.org/10.1080/17452759.2023.2230979>.
- [53] Nguyen, A.K.; Narayan, R.J. Two-Photon Polymerization for Biological Applications. *Mater. Today* 2017, 20, 314-322. <https://doi.org/10.1016/J.MATTOD.2017.06.004>.
- [54] Nouri-Goushki, M.; Isaakidou, A.; Eijkel, B.I.M.; Minneboo, M.; Liu, Q.; Boukany, P.E.; Mirzaali, M.J.; Fratila-Apachitei, L.E.; Zadpoor, A.A. 3D Printed Submicron Patterns Orchestrate the Response of Macrophages. *Nanoscale* 2021, 13, 14304-14315. <https://doi.org/10.1039/D1NR01557E>.
- [55] Udenni Gunathilake, T.M.S.; Ching, Y.C.; Ching, K.Y.; Chuah, C.H.; Abdullah, L.C. Biomedical and Microbiological Applications of Bio-Based Porous

- Materials: A Review. *Polymers* 2017, 9, 160. <https://doi.org/10.3390/polym9050160>.
- [56] Li, Z.; Xu, P.; Shang, L.; Ma, B.; Zhang, H.; Fu, L.; Ou, Y.; Mao, Y. 3D Collagen Porous Scaffold Carrying PLGA-PTX/SDF-1 α Recruits and Promotes Neural Stem Cell Differentiation for Spinal Cord Injury Repair. *J. Biomater. Sci. Polym. Ed.* 2023, 34, 1–24. <https://doi.org/10.1080/09205063.2023.2247715>.
- [57] El-Wakil, N.; Kamel, R.; Mahmoud, A.A.; Dufresne, A.; Abouzeid, R.E.; Abo El-Fadl, M.T.; Maged, A. Risedronate-Loaded Aerogel Scaffolds for Bone Regeneration. *Drug Deliv.* 2023, 30, 51–63. <https://doi.org/10.1080/10717544.2022.2152135>.
- [58] Huang, H.; Qiang, L.; Fan, M.; Liu, Y.; Yang, A.; Chang, D.; Li, J.; Sun, T.; Wang, Y.; Guo, R.; et al. 3D-Printed Tri-Element-Doped Hydroxyapatite/Polycaprolactone Composite Scaffolds with Antibacterial Potential for Osteosarcoma Therapy and Bone Regeneration. *Bioact. Mater.* 2024, 31, 18–37. <https://doi.org/10.1016/j.bioactmat.2023.07.004>.
- [59] Sravani, K.G.; Desala, R.K.; Chand, P.; Sathvik, K.; Rao, K.S.; Lay-Ekuakille, A. Design and Analysis of Bio-Inspired Micro-Needle for Drug Delivery Applications. *IEEE Trans. Nanobioscience* 2023, 22, 237–244. <https://doi.org/10.1109/TNB.2022.3185633>.
- [60] Liu, L.; Kai, H.; Nagamine, K.; Ogawa, Y.; Nishizawa, M. Porous Polymer Microneedles with Interconnecting Microchannels for Rapid Fluid Transport. *RSC Adv.* 2016, 6, 48630–48635. <https://doi.org/10.1039/C6RA07882F>.
- [61] Dewaele, M.; Truffier-Boutry, D.; Devaux, J.; Leloup, G. Volume Contraction in Photocured Dental Resins: The Shrinkage-Conversion Relationship Revisited. *Dent. Mater.* 2006, 22, 359–365. <https://doi.org/10.1016/j.dental.2005.03.014>.
- [62] Bauer, J.; Guell Izard, A.; Zhang, Y.; Baldacchini, T.; Valdevit, L. Programmable Mechanical Properties of Two-Photon Polymerized Materials: From Nanowires to Bulk. *Adv. Mater. Technol.* 2019, 4, 1900146. <https://doi.org/10.1002/admt.201900146>.
- [63] Jiang, L.J.; Zhou, Y.S.; Xiong, W.; Gao, Y.; Huang, X.; Jiang, L.; Baldacchini, T.; Silvain, J.-F.; Lu, Y.F. Two-Photon Polymerization: Investigation of Chemical and Mechanical Properties of Resins Using Raman Microspectroscopy. *Opt. Lett.* 2014, 39, 3034–3037. <https://doi.org/10.1364/OL.39.003034>.
- [64] Pianelli, C.; Devaux, J.; Bebelman, S.; Leloup, G. The Micro-Raman Spectroscopy, a Useful Tool to Determine the Degree of Conversion of Light-Activated Composite Resins. *J. Biomed. Mater. Res.* 1999, 48, 675–681. [https://doi.org/10.1002/\(SICI\)1097-4636\(1999\)48:5<675::AID-JBM11>3.0.CO;2-P](https://doi.org/10.1002/(SICI)1097-4636(1999)48:5<675::AID-JBM11>3.0.CO;2-P).
- [65] Schweiger, S.; Schulze, T.; Schlipf, S.; Reinig, P.; Schenk, H. Characterization of Two-Photon-Polymerization Lithography Structures via Raman Spectroscopy

- and Nanoindentation. *J. Opt. Microsyst.* 2022, 2, 33501. <https://doi.org/10.1117/1.JOM.2.3.033501>
- [66] Zeiger, A.S.; Hinton, B.; Van Vliet, K.J. Why the Dish Makes a Difference: Quantitative Comparison of Polystyrene Culture Surfaces. *Acta Biomater.* 2013, 9, 7354–7361. <https://doi.org/10.1016/j.actbio.2013.02.035>.
- [67] Havenith, S.; Versnel, H.; Agterberg, M.J.H.; de Groot, J.C.M.J.; Sedee, R.-J.; Grolman, W.; Klis, S.F.L. Spiral Ganglion Cell Survival after Round Window Membrane Application of Brain-Derived Neurotrophic Factor Using Gelfoam as Carrier. *Hear. Res.* 2011, 272, 168–177. <https://doi.org/10.1016/j.heares.2010.10.003>.
- [68] Eastwood, H.; Chang, A.; Kel, G.; Sly, D.; Richardson, R.; O’Leary, S.J. Round Window Delivery of Dexamethasone Ameliorates Local and Remote Hearing Loss Produced by Cochlear Implantation into the Second Turn of the Guinea Pig Cochlea. *Hear. Res.* 2010, 265, 25–29. <https://doi.org/10.1016/j.heares.2010.03.006>.
- [69] Saber, A.; Strand, S.P.; Ulfendahl, M. Use of the Biodegradable Polymer Chitosan as a Vehicle for Applying Drugs to the Inner Ear. *Eur. J. Pharm. Sci.* 2010, 39, 110–115. <https://doi.org/10.1016/j.ejps.2009.11.003>.
- [70] Lee, M.Y.; Lee, J.H.; Lee, H.S.; Choi, J.-J.; Jang, J.; Choi, H.; Oh, S.-H.; Jang, J.H. Continuous Topical Drug Delivery Using Osmotic Pump in Animal Cochlear Implant Model: Continuous Steroid Delivery Is Effective for Hearing Preservation. *Acta Otolaryngol.* 2015, 135, 791–798. <https://doi.org/10.3109/00016489.2015.1030771>.
- [71] Jang, J.; Kim, J.; Kim, Y.C.; Kim, S.; Chou, N.; Lee, S.; Choung, Y.; Kim, S.; Brugger, J.; Choi, H.; et al. A 3D Microscaffold Cochlear Electrode Array for Steroid Elution. *Adv. Heal. Mater.* 2019, 8, 1900379. <https://doi.org/10.1002/adhm.201900379>.
- [72] Toulemonde, P.; Risoud, M.; Lemesre, P.E.; Beck, C.; Wattelet, J.; Tardivel, M.; Siepman, J.; Vincent, C. Evaluation of the Efficacy of Dexamethasone-Eluting Electrode Array on the Post-Implant Cochlear Fibrotic Reaction by Three-Dimensional Immunofluorescence Analysis in Mongolian Gerbil Cochlea. *J. Clin. Med.* 2021, 10, 3315. <https://doi.org/10.3390/jcm10153315>.
- [73] Tamura, T.; Kita, T.; Nakagawa, T.; Endo, T.; Kim, T.-S.; Ishihara, T.; Mizushima, Y.; Higaki, M.; Ito, J. Drug Delivery to the Cochlea Using PLGA Nanoparticles. *Laryngoscope* 2005, 115, 2000–2005. <https://doi.org/10.1097/01.mlg.0000180174.81036.5a>.
- [74] Dang, H.P.; Shabab, T.; Shafiee, A.; Peiffer, Q.C.; Fox, K.; Tran, N.; Dargaville, T.R.; Huttmacher, D.W.; Tran, P.A. 3D Printed Dual Macro-, Microscale Porous Network as a Tissue Engineering Scaffold with Drug Delivering Function. *Biofabrication* 2019, 11, 35014. <https://doi.org/10.1088/1758-5090/ab14ff>.

- [75] Gomes Filho, M.S.; Oliveira, F.A.; Barbosa, M.A.A. A Statistical Mechanical Model for Drug Release: Investigations on Size and Porosity Dependence. *Phys. A Stat. Mech. Its Appl.* 2016, 460, 29–37. <https://doi.org/10.1016/j.physa.2016.04.040>.
- [76] Siepmann, J.; Siepmann, F. Mathematical Modeling of Drug Delivery. *Int. J. Pharm.* 2008, 364, 328–343. <https://doi.org/10.1016/j.ijpharm.2008.09.004>.

PART II - Chapter 03

Micromechanics & Materials



3. MICROMECHANICS AND MANUFACTURABILITY OF 3D PRINTED MICROSTRUCTURES

Abstract

A very versatile AM technology with great potential for fabricating biomedical devices is two-photon polymerization (2PP). It can produce polymeric three-dimensional nano- to mesoscale structures with high flexibility in processing parameters and feature sizes down to the nanometer length scale. This study examines the influence of various 2PP printing parameters on the morphology and mechanical properties of solid and porous microstructures fabricated from three commercially available resins: IP-Q, IP-S, and IP-PDMS. To further evaluate micromechanical behavior, micropillar compression tests were additionally conducted using IP-Q, which had not been extensively characterized in this context. The stiffness of the porous microstructures was 80-85% for IP-Q and IP-S and 50% for IP-PDMS of the stiffness of their solid counterparts. The resins were also examined using FTIR spectroscopy to determine their degree of conversion (DC). The calculated DC values were 38% for IP-Q and 61% for IP-S and IP-PDMS. The optimal printing parameters for the IP-Q micropillars were determined to be a laser power (LP) of 50 mW, a slicing distance (s) of 1.2 μm , and a hatching distance (h) of 1 μm . These settings correspond to a peak laser intensity of $1.58 \times 10^{11} \text{ W/cm}^2$, a focal spot diameter (d_{sp}) of 3.17 μm , a Rayleigh length (z_R) of 10.13 μm , and a voxel overlap (δ) of 0.6. These conditions resulted in a Young's modulus of 3.7 GPa and a yield strength of 75.21 MPa. Overall, the findings highlight the complexity of optimizing processing parameters when introducing porosity into designs and when working with different scales and materials. Together, these results establish a systematic framework for tailoring 2PP processing conditions, offering a foundation for future application-oriented studies in biomedical microdevices.

Isaakidou A., Ganjian M., Moosabeiki V., Leeflang M.A., Goushki M.N., Boukany P.E., Wątroba M., Groetsch A., Schwiedrzik J., Mirzaali M.J., Apachitei I., Fratila-Apachitei L.E. and Zadpoor A.A. *Advanced Engineering Materials*. 2025. 000: e202500977. <https://doi.org/10.1002/adem.202500977>

3.1. INTRODUCTION

Two-photon polymerization (2PP) has emerged as a cutting-edge technology with the compelling advantage of producing complex three-dimensional (3D) micro- and nanoscale structures [1]. The working principle of 2PP is based on the nonlinear absorption of two photons by a photoinitiator, which occurs at high photon densities near the laser focus and triggers localized polymerization within a photosensitive material [2]. The quadratic relationship of two-photon absorption with light intensity provides high precision and resolution by enabling precise control of the crosslinking photoreaction, ensuring that polymerization only occurs within the localized focal region (*i.e.*, voxel) [3]. This fine control over the fabrication process is particularly advantageous for creating 3D microstructures with a high level of detail, which is essential for tissue engineering applications and drug delivery systems [2]. A wide range of materials can be used in the two-photon fabrication, including polyacrylic resins, hydrogels, epoxides, and inorganic/organic polymers [4,5].

The selection of suitable materials for biomedical applications (**Figure 3.1C**) is broadened by the increased availability of diverse 2PP materials and their characteristics. The biocompatibility of such materials is a critical factor, necessitating investigations into the interactions between the materials, living tissues [6] and cells [7]. Additionally, the mechanical properties and printing resolution are crucial factors in determining their suitability for specific applications [8]. Studies on the Young's modulus, E , of various commercially available photoresists often consider the printing conditions (**Figure 3.1A**), such as hatching and slicing distance, laser power, and scanning speed, as these influence crosslinking [8–11]. The Young's moduli of polyacrylic resins, epoxides, and inorganic/organic polymers are generally reported to be in the GPa range, while those of hydrogels tend to be in the kPa range [12]. Optimizing the printing conditions is essential to ensure mechanical stability and versatility across various materials, shapes, and scales (**Figure 3.1B**). For example, recent advances in continuous scanning have even enabled high-resolution fabrication across five orders of magnitude. This approach extends the applicability of 2PP into the meso-regime, allowing for the fabrication of centimeter-scale objects with microscale or even nanoscale decorations [13].

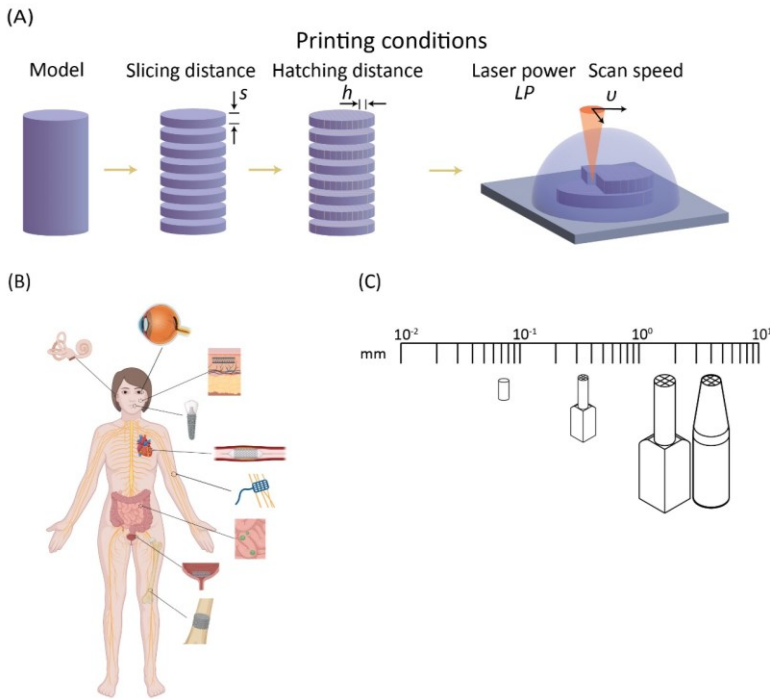


Figure 3.1. (A) A schematic representation of the printing conditions (i.e., slicing and hatching distance, laser power, and scanning speed) that govern the 2PP printing process. (B) Human body anatomy with details on organs that can benefit from porous medical devices in various scales and materials. (C) The versatility of the 2PP method allows for printing across different scales and materials for biomedical applications.

In this study, we focus on the printing and mechanical characterization of solid and porous microstructures inspired by a recently developed cochlear implant design [14]. The structures were fabricated using three photocurable resins: acrylate-based IP-Q, IP-S, and the hybrid polydimethylsiloxane- and acrylate-based IP-PDMS resin (Nanoscribe GmbH & Co. KG, Karlsruhe, Germany). These resins were selected to represent a broad range of mechanical properties, with IP-Q and IP-S exhibiting elastic moduli of 3.17 GPa [11] and 4.6 GPa [15], respectively, and IP-PDMS, a compliant elastomer with a much lower elastic modulus of 17.8 MPa [16]. This range of mechanical properties makes the study of the selected resins relevant for diverse biomedical applications, from load-bearing permanent structures to soft, compliant microsystems.

We aim to provide insights into material selection, optimization of 2PP printing settings, and mechanical properties of the printed 3D microstructures. These structures could be relevant for applications in microfluidics [17,18], drug delivery [19,20], and tissue engineering [21,22]. For example, in drug-delivery applications, porosity is a crucial factor to consider, as it affects drug loading, release kinetics, and bioavailability. Encapsulation of drugs within porous matrices can enhance stability, solubility, and dissolution rates, while allowing precise control over drug release. This approach improves cellular uptake and therapeutic efficacy, and minimizes side effects [23,24]. The present study does not focus on the fabrication of ready-to-use biomedical devices, but rather systematically generates knowledge on how 2PP processing parameters influence the manufacturability, geometry, and micromechanical response of selected commercial resins. This exploration provides a foundation for future device-specific evaluations.

Using all three previously mentioned photoresists, we developed printing methods to manufacture microstructures that were either solid or exhibited confined microporosity. We then characterized the morphology, chemistry, and mechanics of the resulting solid and porous micro-architectures. To our knowledge, no systematic investigation has been conducted on how 2PP printing parameters affect the shape fidelity, chemistry, and mechanical properties of the IP-Q material. Therefore, we performed further mechanical characterization of IP-Q micropillars printed with varying parameters through compression testing. A key aspect of the current study is the use of microcompression to assess the mechanical properties of IP-Q material. In contrast to our previous study [25], where mechanical characterization of IP-Q structures required enlarging the corresponding structures to perform mechanical testing and to combine them with finite element analysis (FEA) models for validation, the current method enabled direct assessment of the material properties of IP-Q. Mechanical properties from such printed solid structures are important input parameters for constitutive models. Thus, our results provide valuable new data for researchers working with the 2PP resins included in this study that can be used for microfluidics, cell scaffold applications, and drug delivery systems (*e.g.*, cochlear implants).

3.2. MATERIALS AND METHODS

3.2.1. 2PP PRINTING OF MICROSCALE STRUCTURES USING IP-Q, IP-S, AND IP-PDMS

Computer-aided design (CAD) models of solid and porous microscale structures, based on recently developed cochlear implant models [14] with dimensions $86 \times 86 \times 343 \mu\text{m}^3$ and a tip diameter of $50 \mu\text{m}$, were created using SolidWorks (Dassault Systèmes SE, Vélizy-Villacoublay, France) and nTopology 3.35 (nTopology Inc., New York, NY, USA), respectively. Using Nanoscribe's Describe software, the designs were used to create the printing job file for the direct laser writing system (Photonic Professional GT, Nanoscribe GmbH, Eggenstein-Leopoldshafen, Germany) operating with a pulsed femtosecond laser (wavelength = 780 nm , pulse duration = 100 fs , with a repetition rate of 80 MHz , Galvo writing mode). For printing with the IP-Q resin a droplet of resin was applied to a silicon substrate and then exposed to the laser beam using a $10\times$ objective ($\text{NA} = 0.3$). For IP-S and IP-PDMS, a droplet of resin was applied to ITO-coated substrates and then exposed to the laser beam using a $25\times$ objective ($\text{NA} = 0.8$). Different printing conditions were explored to identify optimal parameters for repeatable and stable prints of solid and porous models for each resin type (**Table 3.1**). For each resin and condition (solid and porous), three representative microstructures were fabricated and characterized ($n = 3$). All structures were fabricated in a vertical orientation, aligned with the laser axis. The slicing distance (s) and hatching distance (h) were set to $0.2 \mu\text{m}$ for IP-Q and IP-S and $0.4 \mu\text{m}$ for IP-PDMS. The scanning speed (v) was set at 150 mm/s for IP-Q and IP-S and 100 mm/s for IP-PDMS. Laser power (LP) was varied to investigate its effect, ranging from 20 mW to 40 mW in 10 mW increments for IP-Q and IP-S, and from 35 mW to 50 mW in 7.5 mW increments for IP-PDMS. For the IP-Q structures, following exposure, the development process involved immersion of the prints for 25 minutes in propylene glycol monomethyl ether acetate (PGMEA, Sigma Aldrich, Darmstadt, Germany), a 5-minute rinse in isopropyl alcohol (IPA, Sigma Aldrich, Darmstadt, Germany), and drying with an air gun. For the IP-S structures, the development process involved immersing the prints in PGMEA for 20 minutes, followed by 30 seconds in methoxy-

nonafluorobutane (Novec 7100, Sigma Aldrich, Darmstadt, Germany), and then drying with an air gun. In the case of the IP-PDMS structures, the development involved immersing the prints in IPA for 5 minutes, followed by drying with an air gun.

Table 3.1. Printing parameters for microstructures made with IP-Q, IP-S, and IP-PDMS. The best settings for printing porous and solid microstructures are given in bold (LP: laser power, v : scanning speed, h : hatching distance, s : slicing distance).

	LP (mW)	v (mm/s)	h (μm)	s (μm)
IP-Q	20, 30, 40	150	0.2	0.2
IP-S	20, 30, 40	150	0.2	0.2
IP-PDMS	35, 42.5 , 50	100	0.4	0.4

3.2.2. 2PP PRINTING OF MICROPILLARS USING IP-Q

Micropillars with a diameter of $D = 50 \mu\text{m}$ and a height of $H = 100 \mu\text{m}$ were designed using SolidWorks (Dassault Systèmes SE, Vélizy-Villacoublay, France). The scanning speed (v) was set to 100 mm/s. Two groups were investigated: in the first group, the slicing distance (s) was fixed at $5 \mu\text{m}$ while the hatching distance (h) was varied from 0.4 to $3.4 \mu\text{m}$ in $0.6 \mu\text{m}$ steps; in the second group, the hatching distance was fixed at $1 \mu\text{m}$ while the slicing distance was varied from 1.2 to $7.5 \mu\text{m}$ in $1.26 \mu\text{m}$ increments. The laser power (LP) was varied between 20 and 60 mW in 10 mW increments for both groups (**Table 3.2**). For each of the above mentioned conditions one representative micropillar was fabricated and characterized ($n = 1$). Preparation for printing and development of the printed micropillars was performed according to the experimental procedure for IP-Q described in **Section 3.2.1**.

Table 3.2. Printing parameters for the micropillars made with IP-Q (LP: laser power, v : scanning speed, h : hatching distance, s : slicing distance).

Printing parameter	IP-Q
LP (mW)	20, 30, 40, 50, 60
v (mm/s)	100
h (μm)	0.4, 1.0, 1.6, 2.2, 2.8, 3.4
s (μm)	1.2, 2.5, 3.7, 5.0, 6.2, 7.5

3.2.3. MORPHOLOGICAL CHARACTERIZATION OF MICROSCALE STRUCTURES AND MICROPILLARS

Structural characterization of the printed samples was done by scanning electron microscopy (SEM) (FEI Helios G4 CX dual-beam workstation, Hillsborough, OR, USA). Before SEM imaging, the samples were gold sputtered (gold layer thickness ~ 5 nm) using a sputter coater (JFC-1300, JEOL, Akishima, Japan). The influence of this gold layer on the mechanical behavior of the samples is negligible [26]. Focused ion beam scanning electron microscopy (FIB-SEM) (FEI, Helios Nano Lab 650, Hillsborough, OR, USA) was used to examine the pore morphology and calculate the apparent porosity and relative density of the 3D porous microstructures. To image the pores longitudinal cross-sections of the samples were prepared by FIB (Current: 0.17 nA, voltage: 30 kV).

3.2.4. CHEMICAL CHARACTERIZATION OF IP-Q, IP-S, AND IP-PDMS

The elemental composition of IP-Q, IP-S, and IP-PDMS resins was quantified using X-ray photoelectron spectroscopy (XPS) (Thermo Fisher K-Alpha instrument, Rockford, IL, USA). Each sample was scanned four times, with an energy step of 0.4 eV, utilizing an Al K α source gun with a spot size of 400 μm^2 . To identify the functional groups in the different photoresists before and after polymerization and to assess the degree of conversion (DC), Fourier transform infrared spectroscopy (FTIR) was used (Nicolet FTIR spectrometer 6700, Thermo Fisher Scientific in Waltham, MA, USA). The spectra acquisition spanned the range of 4000–463 cm^{-1} . The DC was determined by measuring the change in the absorbance peak height of the bonds most relevant to the polymerization of the resins, according to [27]:

$$DC = \left(1 - \frac{A_P}{A_R}\right) \times 100\% \quad (\text{Eq. 3.1})$$

where A_P is the absorbance of the sample after polymerization (printed structure), and A_R is the absorbance of the unpolymerized resin.

3.2.5. COMPRESSION OF MICROSCALE STRUCTURES AND MICROPILLARS

The IP-Q and IP-S microstructures were compressed using an *ex situ* indenter setup developed at Empa (Thun, Switzerland) and based on commercial hardware for actuation, sensing, and electronics (Alemnis AG, Thun, Switzerland). These experiments were conducted at ambient temperature and humidity, using a flat punch diamond tip (diameter = 150 μm , 60° cone angle) (Synton MDP, Nidau, Switzerland). The microstructures were compressed uniaxially using a quasi-static displacement-controlled loading protocol at a displacement rate of 50 nm/s and up to 10% of engineering strain. The stiffness of the microstructures was extracted from the best linear fit of the loading segment of the load-displacement curves.

For the IP-PDMS microstructures, compression was conducted using a Piuma nanoindenter (Optics11 Life B.V., Amsterdam, The Netherlands), which featured a sphere-shaped tip with a radius of 48 μm (able to cover the tip of the structures) and a measured and calibrated stiffness of 3.89 N/m. Compression was repeated nine times in a grid pattern to ensure complete coverage of the specimen's tip ($d = 50 \mu\text{m}$), with a 5 μm displacement for each step. This test was conducted for four printed samples. According to the manufacturer's instructions [28] the samples were submerged in demineralized water throughout the test to avoid adhesion of the probe and the sample. An indentation-controlled procedure was followed for these measurements, with a maximum indentation depth of 5000 nm, a displacement rate of 500 nm/s, and a retraction speed of 5000 nm/s. The force-displacement curves were analyzed, and the data was extracted from the best linear fit of the loading part of the curves.

The IP-Q micropillars were tested by applying the same tip specifications and ambient conditions as the IP-Q and IP-S microstructures. They were compressed uniaxially using a quasi-static displacement-controlled loading protocol at a displacement rate of 50 nm/s and up to 36.5% of engineering strain (ϵ). The engineering strain was calculated based on the recorded displacement data and the initial height of each micropillar, determined by high-resolution SEM imaging. The engineering stress was then calculated by dividing the recorded load data by the top

surface area of the structures. The yield stress (σ_y) was determined using the 0.2% offset criterion. The elastic modulus (E) was extracted from the loading segment of the stress-strain curves before the yield point using linear regression.

3.2.6. STATISTICAL ANALYSIS

To investigate whether there is a significant difference in the stiffness between the solid and porous counterparts of the microstructures fabricated by IP-Q, IP-S, and IP-PDMS, we conducted unpaired t-tests ($p \leq 0.05$). We assessed the normality of the data using the Shapiro-Wilk test ($p \leq 0.05$), which is appropriate for the small sample size in our study. The results of these normality tests for the stiffness values are presented in **Figure S3.1**. We applied one-way ANOVA analysis (**Table S3.2**) and the Tukey's multiple comparisons test (**Table S3.3**) to assess the cross-material comparison amongst our groups. The data was analyzed using Prism 10 (GraphPad Software Inc., San Diego, CA, United States).

3.3. RESULTS

3.3.1. MORPHOLOGICAL CHARACTERIZATION OF MICROSCALE STRUCTURES

A parametric study was performed to determine suitable printing parameters for a repeatable fabrication of the microscale structures from each resin (**Figure 3.2**). Porous structures from IP-PDMS printed with $h = s = 0.4 \mu\text{m}$, $v = 150000 \mu\text{m/s}$, and $LP = 35$ or 50 mW exhibited defects on both their tip and main body. Random resin protrusions were observed on their tip, and dents on their main trunk revealed their inner porous structure (**Figure 3.2C**). IP-PDMS structures printed with $LP = 42.5$ mW exhibited improved overall quality with fewer manufacturing imperfections (**Figure 3.2C**). Examination through FIB milling of the porous structures revealed well-formed internal pores (**Figure 3.2D**). The parametric study on the microstructures made by IP-Q and IP-S did not reveal outer morphological differences in different printing settings. Although the exact sizes of the pores could not be accurately quantified from the FIB/SEM images, the parametric study indicated the window of printing conditions (see also **Table 3.1**) that can be used for each type of resin to generate stable and reproducible solid and porous microscale structures.

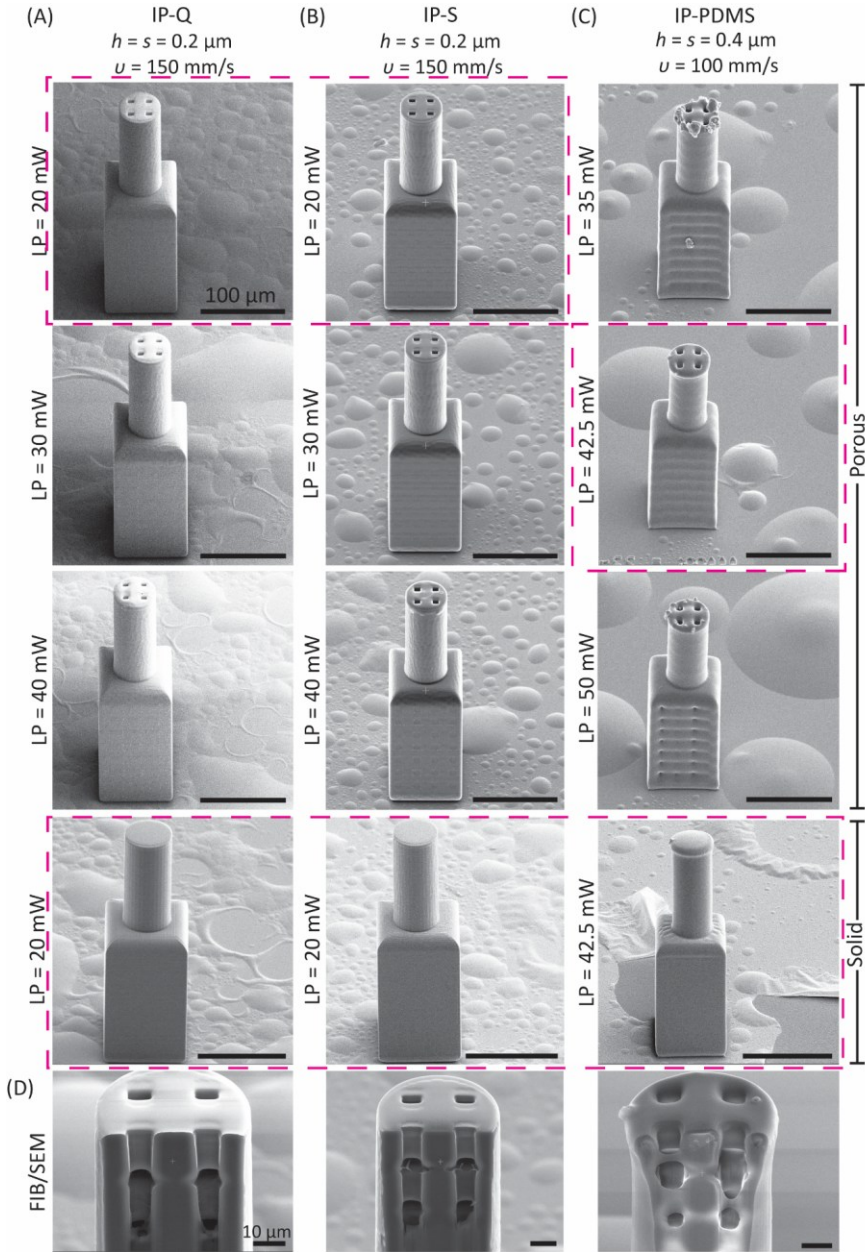


Figure 3.2. Tilt-view (52°) SEM images of 2PP printed porous and solid microstructures with varying laser powers (LP = 20 - 50 mW) made from (A) IP-Q (left), (B) IP-S (middle), and (C) IP-PDMS (right) resin (scale bar = $100 \mu\text{m}$). The dashed lines enclose the highest-quality prints. (D) The FIB milling of porous microstructures fabricated using the mentioned resins demonstrates the embedding of pores (scale bar = $10 \mu\text{m}$).

3.3.2. MORPHOLOGICAL CHARACTERIZATION OF MICROPILLARS

Since the process-structure-mechanics relationship for the 2PP printed IP-Q material was not previously studied, a more detailed parametric study was performed, and the results were used for understanding the mechanical properties of the printed samples. Therefore, a first series of IP-Q micropillars were fabricated by varying the laser power and slicing distance while keeping the hatching distance ($h = 1 \mu\text{m}$) and scanning speed ($v = 100000 \mu\text{m/s}$) constant (**Figure 3.3**). When using a laser power of $LP = 20 \text{ mW}$ and a slicing distance of $s = 7.5 \mu\text{m}$, no micropillars formed on the substrate (**Figure 3.3**), indicating that the processing parameters were unsuitable for initiating photopolymerization. As the slicing distance decreased, micropillars began to form. Lower slicing distances resulted in micropillars with dimensions closer to the designed specifications ($D = 50 \mu\text{m}$, $H = 100 \mu\text{m}$); however, they did not reach the target dimensions for D (**Figure 3.4A**). Generally, with $LP > 30 \text{ mW}$, micropillars could be printed even with larger slicing distances, while their dimensions deviated further from the designed values (**Figure 3.4A**). The diameter of the pillars deviated by 22-37% from the designed one ($D = 39.2 \mu\text{m}$). The largest diameter achieved was at $LP = 60 \text{ mW}$ and for $s = 1.2 \mu\text{m}$. At the largest diameter settings, the pillar's height was measured to be approximately 5% larger than the designed one, thus $104.6 \mu\text{m}$.

A second batch of IP-Q micropillars was fabricated to study the influence of varying laser power and hatching distance while keeping the slicing distance ($s = 5 \mu\text{m}$) and scanning speed ($v = 100000 \mu\text{m/s}$) constant (**Figure 5**). Laser power values of $LP = 20 \text{ mW}$ did not result in the fabrication of stable micropillars. By increasing the laser power to 30 mW , the micropillars were formed for low values of the hatching distance ($h = 0.4$ and $1.0 \mu\text{m}$). Increasing the hatching distance ($h = 2.2 - 3.4 \mu\text{m}$) decreased the chance of polymerization so that the fabricated micropillars were not stable enough to stand vertically on the substrate, which led to bending (**Figure 3.5**). When $LP > 40 \text{ mW}$, micropillars formed for all chosen hatching distances (**Figure 3.5**). Similarly to the investigation on the slicing distance, smaller hatching distances resulted in dimensions closer to the designed ones. The diameter of the pillars deviated by 18 - 99% from the designed one. The largest diameter achieved was at $LP = 60 \text{ mW}$ and $h = 0.4 \mu\text{m}$ ($D = 41.1 \mu\text{m}$), and at those settings, the height of the micropillar was $H = 109$

μm , 9% larger than designed. Generally, the higher the laser power and the smaller the slicing and hatching distance values, the closer the dimensions were to the designed values (**Figure 3.4B**). However, for $s = 5 \mu\text{m}$ and $h = 2.8 \mu\text{m}$, both the pillar diameter and height increased until $LP = 50 \text{ mW}$, but for $LP = 60 \text{ mW}$, there is a drop in the resulting D and H values (purple arrows on **Figure 3.4B**).

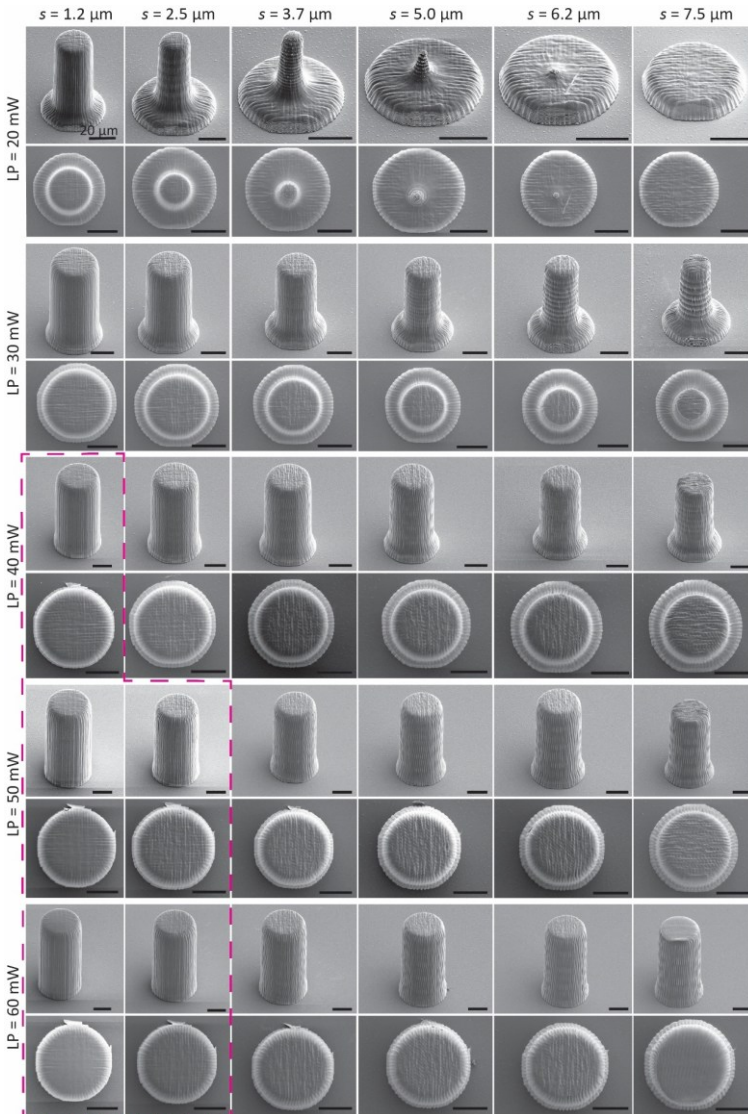


Figure 3.3. Top and tilt-view (52°) SEM images of 2PP-printed IP-Q micropillars fabricated with varying slicing distance ($s = 1.2 - 7.5 \mu\text{m}$) and laser power ($LP = 40 - 120\%$) for constant hatching distance ($h = 1 \mu\text{m}$) and scanning speed ($v = 100 \text{ mm/s}$) (scale bar = $20 \mu\text{m}$). The dashed lines enclose the highest-quality prints.

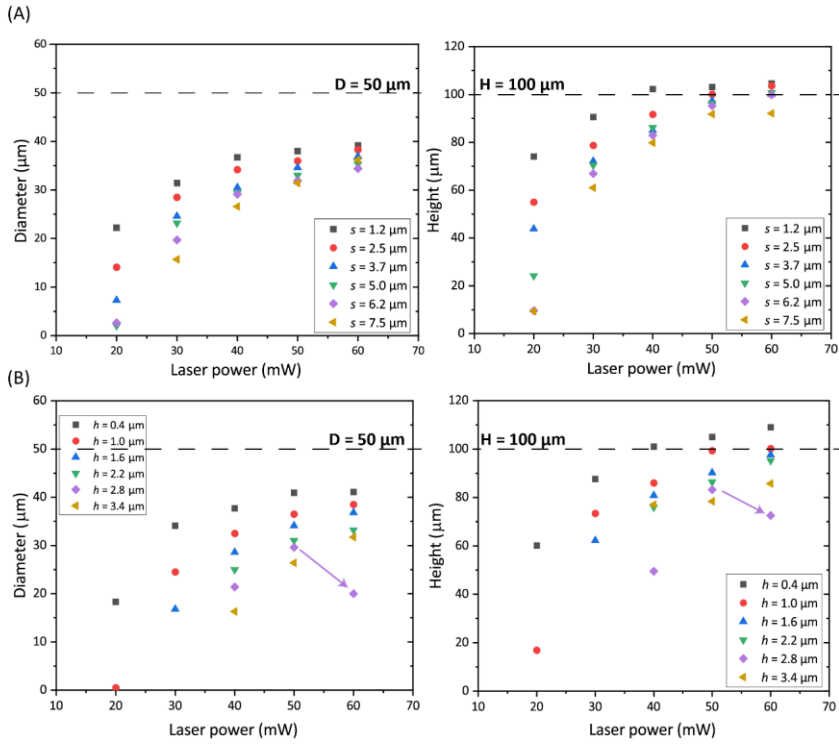


Figure 3.4. (A) Effects of laser power (LP) and slicing distance (s) on the diameter (D) and height (H) of micropillars fabricated using IP-Q; (B) Effects of LP and hatching distance (h) on D and H of the micropillars fabricated using IP-Q.

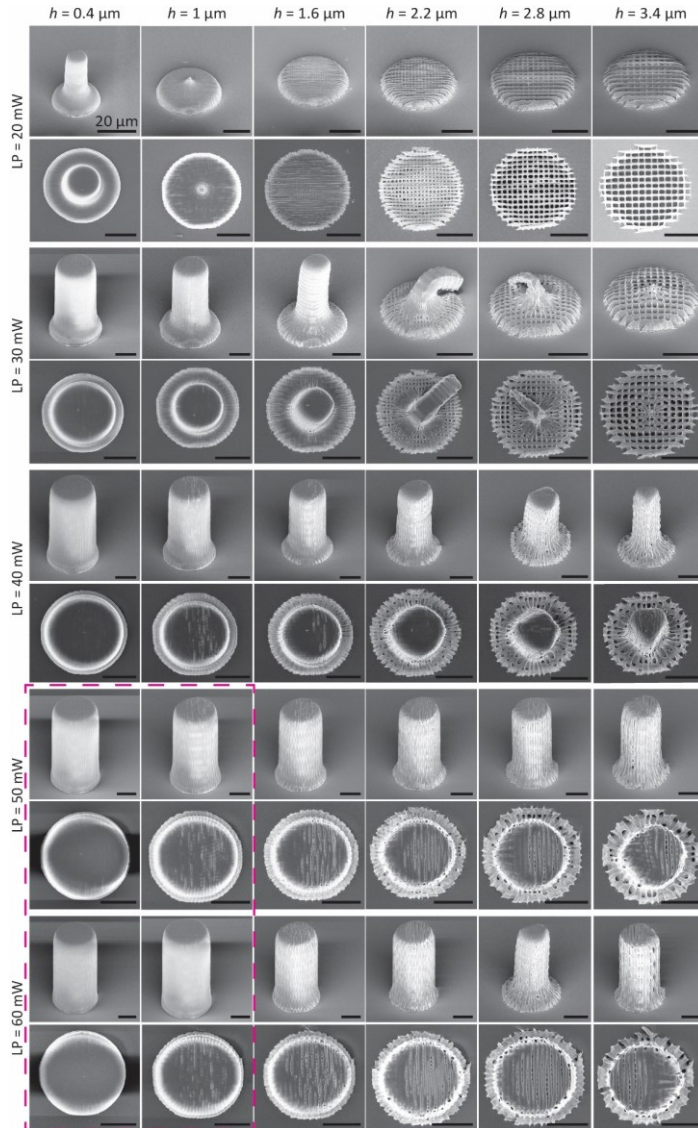


Figure 3.5. Top and tilt-view (52°) SEM images of 2PP-printed IP-Q micropillars fabricated with varying hatching distance ($h = 0.4 - 3.4 \mu\text{m}$) and laser power (LP = 40 - 120%) for constant slicing distance ($s = 5 \mu\text{m}$) and scanning speed ($v = 100 \text{ mm/s}$) (scale bar = $20 \mu\text{m}$). The dashed lines enclose the highest-quality prints.

3.3.3. CHEMICAL CHARACTERIZATION OF IP-Q, IP-S, AND IP-PDMS

A survey scan was performed to identify elements different from C, O, and N for all the resins (**Figure 3.6A**). The IP-S and IP-Q samples are similar, and their XPS survey graphs overlap. The IP-PDMS survey scan clearly shows the presence of Si and

confirms the presence of the monomer $\text{Si}(\text{CH}_3)_2\text{O}$. The spectrum shows a peak centered around 284.47 eV for IP-S (**Figure 3.6B**). For IP-Q, the spectrum is centered around 284.10 eV (**Figure 3.6C**), corresponding to the C1s bond. For IP-PDMS, the C1s bond is found at 284.05 eV (**Figure 3.6D**). A peak deconvolution for each of the resins confirms the presence of C–C(C1s A), C–O(C1s B), O–C=O(C1s C), and C=O(C1s D) groups. The corresponding binding energies can be found in **Table 3.3**. Due to polymerization, the resins' FTIR spectra indicated the depleted bonds' positions. For IP-S, the depletion of the characteristic bands associated with the C=C group was found at 814, 941, 1406, and 1637 cm^{-1} (**Table S3.4, S3.5**). The corresponding values for C=O and C–O were at 1699 cm^{-1} and 1150/1240 cm^{-1} . According to **Eq. 3.1**, the DC based on the decrease of the peak height at 1637 cm^{-1} was approximately 58% (**Table S3.6**). The depletion of the C=C groups at 1525, 1597, and 1639 cm^{-1} and the C=O group at 1700 cm^{-1} corroborate the polymerization of the IP-Q resin with an approximate DC = 37% based on the peak height change at 1639 cm^{-1} (**Table S3.4, S3.5, S3.6**). The polymerization of IP-PDMS can be confirmed by the decrease of the intensity of different functional groups at 790, 1257, and 1729 cm^{-1} , related to the Si–CH₃ group, at 1009 and 1062 cm^{-1} , related to the C=O group, at 1187 cm^{-1} because of the C–O group, and at 1405 cm^{-1} related to the C=C group, that yield an approximate DC= 63% at that wavenumber (**Table S4, S5, S6**).

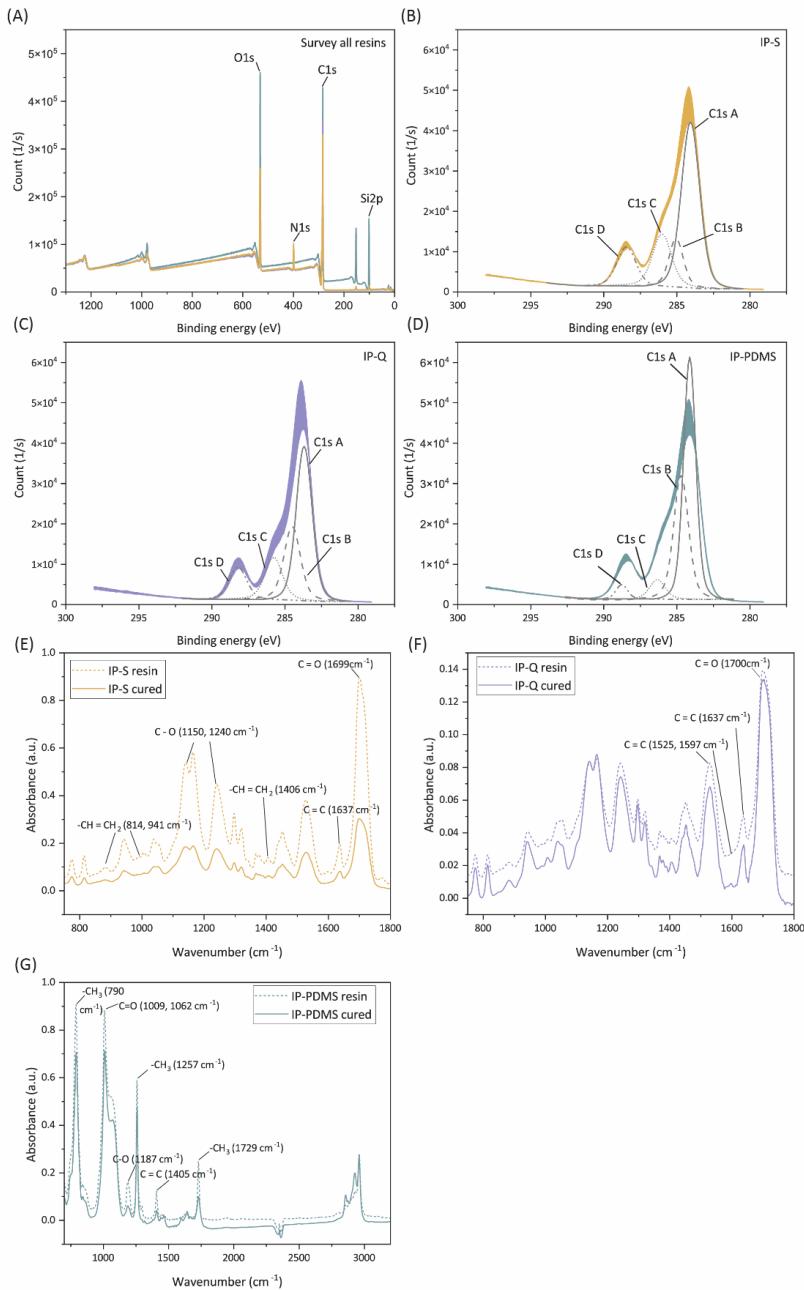


Figure 3.6. (A) XPS survey spectra for IP-S, IP-Q, and IP-PDMS Nanoscribe resins. High energy resolution XPS spectrum of C1s region on (B) IP-S, (C) IP-Q, and (D) IP-PDMS samples. The FTIR spectra of the (E) IP-S resin (dashed line) and the cured version (solid line), (F) IP-Q resin (solid line) and the cured version (dashed line), and (G) IP-PDMS resin (solid line) and the cured version (dashed line).

Table 3.3. The binding energy and atomic percentage of the C1s, O1s, Si2p, and N1s regions for the IP-S, IP-Q, and IP-PDMS Nanoscribe resins.

Bond type	IP-S		IP-Q		IP-PDMS	
	Binding energy (eV)	Atomic percentage (%)	Binding energy (eV)	Atomic percentage (%)	Binding energy (eV)	Atomic percentage (%)
C 1s	284.47	71.93	284.10	75.26	284.05	57.42
C1s A (C - C)	284.07	39.18	283.69	34.89	283.48	25.10
C1s B (C - O)	285.06	9.39	284.51	18.18	284.07	16.38
C1s C (O - C = O)	286.02	13.48	285.78	11.15	285.69	2.77
C1s D (C = O)	288.46	9.66	288.22	8.06	288.13	1.55
O 1s	532.15	21.25	531.87	19.29	531.56	22.89
O1s A	531.20	10.26	531.04	11.00	530.99	17.54
O1s B	532.77	11.40	532.58	8.24	532.29	2.20
Si 2p	101.43	1.43	101.22	4.45	101.42	19.33
Si2p3 A	101.24	1.01	100.96	2.01	100.72	17.09
Si2p1 A	101.97	0	101.69	2.01	101.42	17.10
N 1s	399.34	5.40	394.56	1.00	399.23	0.37
N1s A	399.20	5.62	398.94	4.47	398.66	0.28

3.3.4. MECHANICAL CHARACTERIZATION OF MICROSCALE STRUCTURES AND MICROPILLARS

The stiffness values of the solid and porous structures, made from IP-Q and IP-S resins, were within the same range: 32.97 ± 0.16 kN/m and 33.77 ± 0.28 kN/m for the solid versions and 27.91 ± 0.06 kN/m and 26.98 ± 0.19 kN/m for the porous versions, respectively (**Figure 3.7A**). The porous structures exhibited approximately 85% (IP-Q) and 80% (IP-S) of the stiffness of their solid counterparts. The solid IP-PDMS structures had a stiffness of 11.8 ± 0.1 N/m, and the porous ones had a stiffness of 5.80 ± 0.4 N/m. Thus, they had a stiffness of about 50% smaller than their solid counterparts (**Figure 3.7B**). The difference in the stiffness of solid and porous structures made for each resin type was statistically significant (**Table S3.1**). The elastic modulus E was calculated for the solid structures based on **Eq. 3.2**:

$$E = k \times L/A \quad (\text{Eq. 3.2})$$

where k is the measured stiffness of the solid structure, L is the length of the cylindrical tip of the microstructure, and A is the surface area of the cylindrical tip (**Table S3.2**). The calculated elastic moduli were 2.04 GPa for IP-Q, 2.03 GPa for IP-S, and 870 MPa for IP-PDMS.

The mechanical properties of the IP-Q micropillars, E and σ_y , displayed a distinct dependence on the 2PP printing parameters. For LP = 20 and 30 mW, the micropillars were either not printed or lacked stability, preventing mechanical characterization (**Figures 3.3** and **3.5**). In general, E and σ_y increased with larger LP values but decreased with increasing h and s values. The range of Young's moduli achieved was $E = 1.31 - 3.7$ GPa, while the yield strength ranged $\sigma_y = 24.77 - 81.75$ MPa. The highest mechanical properties were achieved for LP = 50 mW, $h = 1 \mu\text{m}$, and $s = 1.2 \mu\text{m}$ and were $E = 3.7$ GPa and $\sigma_y = 75.21$ MPa (Figure 7C, 7D). Interestingly, the highest E and σ_y values were not associated with the largest achieved dimensions, D and H . For LP = 60 mW, E decreased to 3.2 GPa, but the yield strength value ($\sigma_y = 75.05$ MPa) remained similar to the value obtained at LP = 50 mW (**Figure 3.7C, D**). For LP = 50 mW, $h = 1 \mu\text{m}$, and $s = 7.5 \mu\text{m}$, the resulting micropillars exhibited $E = 2.4$ GPa and $\sigma_y = 57.3$ MPa. Increasing the LP to 60 mW (keeping $h = 1 \mu\text{m}$ and $s = 7.5 \mu\text{m}$) resulted in a slight reduction to $E = 2.36$ GPa, which is almost comparable to the previous value (Figure 7C). The yield strength, however, decreased by nearly 20%, dropping to $\sigma_y = 47.5$ MPa (**Figure 3.7D**). This indicates that while the E remains relatively unaffected by the increase in LP, the σ_y is adversely impacted, highlighting a trade-off between these mechanical properties at higher LP settings. For varying h distances, the mechanical properties of the micropillars followed the general rule of increasing values with increasing LP values (**Figure 3.7E, F**).

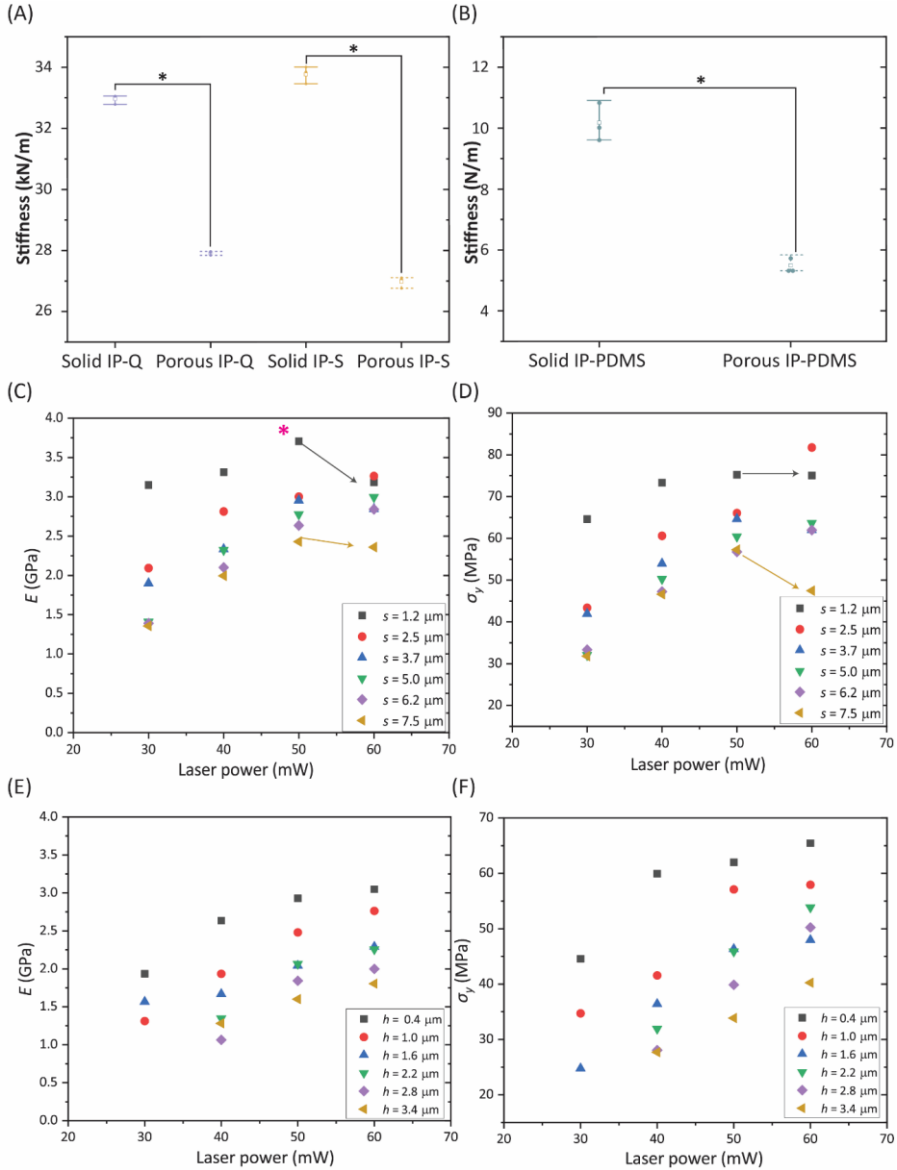


Figure 3.7. The box plots for the stiffness values of solid and porous microstructures printed with (A) IP-Q and IP-S and (B) IP-PDMS. Relationships between laser power (LP), slicing distance (s), hatching distance (h), and the resultant mechanical properties, E modulus, and yield stress σ_y of micropillars fabricated using IP-Q. (C) E (* highest value achieved) and (D) σ_y for $h = 1 \mu\text{m}$, $s = 1.2 - 7.5 \mu\text{m}$ and LP = 30 - 60 mW. (E) E modulus and (F) σ_y for $s = 5 \mu\text{m}$, $h = 0.4 - 3.4 \mu\text{m}$ and LP = 30 - 60 mW.

3.4. DISCUSSION

We aimed to understand the effects of the different parameters of the 2PP printing process on the shape fidelity and mechanical properties of microscale solid and porous structures fabricated from various resins. Therefore, we printed solid and porous microscale structures using the commercial materials IP-Q, IP-S, and IP-PDMS and characterized them morphologically, chemically, and mechanically. This comprehensive study, the most detailed yet available in the literature, enables a better understanding of the process-structure (morphology and chemistry)-mechanics relationships relevant to 2PP technology, especially considering that IP-Q has not been extensively investigated.

3.4.1. STIFFNESS RETENTION IN POROUS MICROSCALE STRUCTURES

The stiffness and calculated elastic moduli of the solid and porous structures in this study were evaluated and compared with available literature data. The solid structures made from IP-Q and IP-S resins exhibited calculated elastic moduli of 2.04 GPa and 2.03 GPa, respectively. These values are lower than the reported elastic moduli for these resins (3.17 GPa [11] for IP-Q and 4.6 GPa [15] for IP-S). For IP-PDMS, the calculated elastic modulus of 870 MPa is significantly higher than the 17.8 MPa value reported in the literature [16]. These discrepancies can be attributed to differences in the printing parameters, the scale of the tested structures, and the mechanical testing method applied.

In terms of stiffness, the solid IP-Q and IP-S structures demonstrated comparable values, consistent with their similar elastic moduli, and the porous structures retained 80-85% of the stiffness of the solid ones. For IP-PDMS, the porous structures retained only half the stiffness of the solid counterparts, highlighting the material's inherently compliant character. The results show that the mechanical properties of 2PP-fabricated solid microstructures differ from bulk material properties reported in the literature, emphasizing the critical influence of microfabrication parameters, sample design, and testing methods on the evaluation of mechanical performance. This is in accordance with the literature on woodpile structures that have exhibited

mechanical response similar to foams and lattices and thus have proven to be able to modulate the elastic performance by tuning the density of the structure [29].

The SEM/FIB images of the cross-section morphology of the porous microstructures made of the three materials revealed well-defined pores in all the samples (**Figure 3.2**). However, accurately evaluating the pore size of the microstructures was challenging. The SEM/FIB imaging proved unreliable for measuring the pore size, as the ablation process can often introduce artifacts and deformations in the cross-section [30]. X-ray μ -CT was also explored but deemed unsuitable because the printing resolution of the structures approached the imaging resolution of the available devices.

Therefore, to estimate the porosity range of the printed microstructures, we applied the Gibson-Ashby model [31], using the stiffness values obtained from the micromechanical tests. According to this model, a power-law relationship exists between the relative density of a porous structure and its mechanical properties:

$$k^*/k_{solid} = C \times (\rho^*/\rho_{solid})^n \quad (\text{Eq. 3.3})$$

where k^* and k_{solid} represent the stiffness of the porous and solid structures, respectively, ρ^* and ρ_{solid} are their corresponding densities, C is the Gibson-Ashby constant and n is a material-specific exponent.

For this analysis, we assumed $C = 1$, and $n = 1$ and 2 . Using these assumptions, we calculated the range of the relative density (ρ^*/ρ_{solid}) and porosity (φ) for the three investigated microstructures (**Table 3.4**). Based on these calculations, the porosity values of the samples were estimated to be between 8.5% ($n = 1$) to 15.5% ($n = 2$) for IP-Q, between 15.5% ($n = 1$) to 20% ($n = 2$) for IP-S and between 31.5% ($n = 1$) and 51% ($n = 2$) for IP-PDMS.

The Gibson-Ashby model results highlight significant deviations from the designed porosity of 26% for all structures (**Table S3.5**). For IP-Q and IP-S, the estimated porosity values are lower than the design, which can be attributed to partial pore closure and reduced pore connectivity during the 2PP fabrication process. Several factors may explain these discrepancies. First, the degree of conversion in 2PP resins is typically incomplete, as also observed in this study, leading to local variations in

crosslink density and densification of the polymer network, which effectively reduces the available pore volume. Second, voxel size, overlap, and local laser intensity influence the exposure dose [32–34], while increased overlap can counterbalance insufficient conversion, excessive exposure may cause material accumulation that narrows or even closes the designed pores. Third, post-processing steps introduce additional variation, as capillary forces during solvent evaporation and the release of internal stresses can promote shrinkage or deformation of thin features [35]. In contrast, the higher porosity values estimated for IP-PDMS suggest that its printed pore size and connectivity were closer to the design, as also supported by SEM/FIB imaging. When comparing the three resins, it becomes evident that printing the *same* porous design requires very different compromises in processing. This comparison highlights how delicate and resin-specific the optimization of printing parameters must be in order to balance polymerization kinetics, voxel geometry, and development effects to achieve reliable porosity across different materials.

To validate theoretical models like Gibson-Ashby, future studies could incorporate finite element analysis (FEA) simulations to model the deformation and mechanical properties of the porous structures more effectively. Submicron X-ray imaging, potentially combined with *in situ* mechanical testing and digital image correlation techniques, could provide accurate, high-resolution validation of both porous structures and FEA models. Moreover, this study did not investigate orientation-dependent effects, as all structures were printed vertically. Since build angle can influence voxel arrangement, polymerization efficiency, and material anisotropy, it is expected to affect both geometry and mechanical properties. Printing orientation therefore represents an unexplored parameter that should be systematically studied in future work, particularly for porous architectures and large aspect ratio structures. A key novelty of this study lies in the direct comparison of stiffness retention across three different materials (*i.e.*, IP-Q, IP-S, and IP-PDMS) fabricated into similar porous designs. By employing the same geometric design and fabrication process, this approach reveals how each resin responds to the introduction of porosity. Such a comparative analysis is not reported in the literature and provides unique insights into material-specific behaviors, such as stiffness retention and porosity influence,

under identical experimental conditions. Recent work has demonstrated that 2PP-fabricated microstructured arrays can guide neuronal outgrowth by tailoring mechanical stiffness and topographical cues [36]. These findings further support the potential of finely tuned 2PP architectures across scales and materials in the tissue engineering field.

3.4.2. THE INFLUENCE OF THE PRINTING PARAMETERS ON THE MORPHOLOGY AND MECHANICAL PROPERTIES OF THE IP-Q MICROPILLARS

Our investigation into the impact of the 2PP printing parameters on micropillar fabrication revealed the effects of various printing parameters (*e.g.*, LP, *h*, *s*) on their morphology and their mechanical properties. Higher LP generally resulted in a larger diameter and larger micropillar height, confirming that greater energy input leads to sufficient polymerization and more robust structures [13-16]. The printing parameters *h* and *s* exhibited an inverse relationship with the apparent geometry. Increased *h* and *s* reduced both the diameter and the height of the pillars. This can be explained by the fact that reduced exposure of the material to the laser results in less crosslinking and sparse structures. Increasing the laser power generally had a positive effect in reducing the impact of the slicing and hatching distances on the diameter, height, and mechanical properties of the fabricated micropillars [15]. The desired micropillar geometry, however, was not achieved with any of the tested parameter combinations, highlighting the need for design adjustments. On average, the lateral dimension (diameter) should be increased by approximately 30%, while the axial dimension (height) should be reduced by about 10% to achieve the target geometry under most tested conditions. The decrease in both diameter and height for $h = 2.8 \mu\text{m}$ and $s = 5 \mu\text{m}$ despite the large LP = 60 mW shows that there is a boundary to the extent the laser power can positively contribute to a better geometry. That is because excessive laser power can cause a saturation in the polymerization of the material and induce burning. The morphological trends were to a large extent similar to the results of the mechanical properties of the micropillars. In most cases, both the elastic modulus and the yield strength of the micropillars increased with an increasing laser power and for small *h* and *s* values. The best mechanical properties ($E = 3.7 \text{ GPa}$, $\sigma_y = 75.21 \text{ MPa}$) were, however, not achieved for LP = 60 mW but for LP = 50 mW and the

smallest slicing distance ($s = 1.2 \mu\text{m}$). The calculation of the degree of conversion (DC = 37%) for those conditions confirmed an efficient exposure of the material to the laser power. Unlike prior work [9], where the E values of the 2PP-printed IP-Q samples were assessed by using indentation testing, we employed uniaxial micropillar compression to evaluate the mechanical properties. The E values measured in the current study are notably larger and this can be attributed to the hatching and slicing parameters that are much smaller than the values explored before and can lead to higher structural density. Another aspect that can explain the differences in the measured values could be the presence of surface imperfections and heterogeneities that can affect the indentation results, in contrast to the micropillar compression approach, which can provide an evaluation of the bulk mechanical properties. Moreover, the DC value obtained for IP-Q in this study is also smaller than the already reported one. The reported values were between 55 and 80%. However, the spectra were obtained with Raman spectroscopy, and the DC calculation was performed by inspecting the changes in the area below the relevant peak, while we obtained the data with FTIR spectroscopy and calculated the value by looking at differences in the peak height.

3.4.3. INFLUENCE OF PHYSICAL EXPOSURE PARAMETERS ON POLYMERIZATION, MECHANICS AND SUITABILITY FOR BIOMEDICAL APPLICATIONS

To better interpret the structure–property relationships, we further calculated the physical exposure parameters associated with the 2PP process following frameworks proposed in recent literature on nonlinear photopolymerization systems [41,42]. These include intensity (I), fluence per pulse (F_p), exposure dose (D), number of pulses per voxel, voxel overlap (δ), focal spot geometry (lateral diameter, d_{xy} , Rayleigh length, (z_R) derived from the system’s optical configuration parameters (λ , NA, f , τ), and the chosen printing parameters (LP, v , h , s) (Table S3.10-12).

For the fabricated microstructures, the voxel lateral diameter and Rayleigh length spanned $\sim 3.17 \mu\text{m}$ and $10.13 \mu\text{m}$ for IP-Q, $\sim 1.19 \mu\text{m}$ and $1.42 \mu\text{m}$ for IP-S and IP-PDMS, with voxel overlaps (δ) being 0.92, 0.72, and 0.48, respectively. These values show that tighter focusing and a voxel overlap of approximately 50% were sufficient

to achieve stable structures with IP-PDMS. For IP-S that exhibits the same focal geometry as IP-PDMS but with larger voxel overlap, and for IP-Q that shows the largest focal geometry and the largest overlap, we also observe the most significant retention in the mechanical properties compared to IP-PDMS.

We also evaluated the physical exposure parameters for the micropillars fabricated with IP-Q under varying hatching and slicing distances. In both cases (constant h or s), increasing laser power resulted in systematically higher fluence and dose. Interestingly, when slicing was fixed and hatching varied, the voxel overlap even reached negative values (indicating no voxel overlap), and aligned well with the less dense structures observed (**Figure 3.5**).

The relationship between mechanical performance and the peak intensity calculated for the printing of microstructures across all three IP resins revealed a consistent sublinear scaling of both Young's modulus (E) and yield strength (σ_y) across all tested micropillars made from IP-Q (**Figure S3.2**). The power-law fitting yielded exponents (β) ranging from 0.08 to 1.41, significantly below the quadratic behavior expected for ideal two-photon absorption. These results corroborate previous observations that reported saturation-like deviations from ideal quadratic two-photon behavior in different photopolymer systems [41,43].

The calculated exposure intensities in this study, 6.33×10^{10} - 1.12×10^{12} W/cm², appear to be in the range but slightly lower than those reported in the literature for initiator-free systems ($0.58 - 1.55 \times 10^{12}$ W/cm²) [44]. Moreover, the influence of reflective silicon substrates was not considered in the selection of printing parameters. However, periodic interference and standing wave effects may locally affect the exposure, the crosslinking, and explain the ridge-like structures on all 2PP printed structures (**Figure 3.2, 3.3, 3.5**) [41].

In addition to optical exposure parameters, thermal effects during printing and post-curing have also been shown to influence geometry and mechanical performance of 2PP structures. Specifically, thermal control during printing can improve the resolution of lattice structures [45], while thermal post-curing has been reported to increase the degree of conversion and enhance the mechanical properties of 2PP printed structures [46]. In the present study, thermal effects could not be investigated

with our in-house system, and we focused exclusively on as-printed samples. Future work should therefore explore thermal management strategies, both during fabrication and in post-processing, to further harness the process-structure-property regime of IP resins.

Another crucial aspect of these resins is their suitability for biomedical application. The IP resins investigated here (IP-Q, IP-S, and IP-PDMS) are crosslinked thermosets, which are inherently resistant to hydrolysis and therefore not expected to degrade under physiological humidity and temperature (~ 37 °C). According to the manufacturer thermal softening occurs only above ~ 55 °C, outside the range relevant for implantation. These considerations were among the reasons for selecting these resins; however, systematic studies of long-term degradation and stability in biologically relevant environments remain necessary. Previous reports, however, have demonstrated favorable cytocompatibility for IP resins used in 2PP [14,47-50], supporting their potential for biomedical applications. Nevertheless, future studies should perform in-depth evaluations of the biological response on the specific porous and solid architectures presented in this study to confirm their suitability for biomedical translation.

3.5. CONCLUSION

This study demonstrates how 2PP printing parameters govern the morphology and mechanical properties of microscale solid and porous structures fabricated from IP-Q, IP-S, and IP-PDMS resins. For all resins, a set of printing conditions was identified that enabled reproducible structures with morphological integrity. The differences in the optimum printing conditions were attributed to variations in the polymerization behavior of the resins. IP-Q and IP-S required smaller hatching and slicing distances, along with lower laser power, to achieve reliable printing of the structures. In contrast, IP-PDMS needed higher laser power and larger hatching distance for effective polymerization and structural integrity.

Mechanical characterization further revealed material-dependent differences. The porous microstructures made from IP-Q and IP-S resins retained 85% of the stiffness of their solid versions, while the IP-PDMS porous microstructures retained only 50%

of the stiffness of their solid counterparts, likely due to the higher actual porosity of the 3D printed IP-PDMS microstructures.

For IP-Q micropillars, reducing slicing and hatching distances improved dimensional fidelity, while increasing laser power up to 50 mW enhanced mechanical properties. However, excessive exposure introduced geometrical aberrations and reduced yield strength, underscoring the trade-off between accuracy and mechanical performance. Overall, this work establishes a systematic framework for understanding how 2PP processing parameters affect the manufacturability, geometry, and micromechanical behavior of commercial resins. These insights provide a foundation for future studies, where device-specific mechanical performance requirements, such as those of cochlear implants, can be directly addressed.

REFERENCES

- [1] X. Jing, H. Fu, B. Yu, M. Sun, L. Wang, Two-photon polymerization for 3D biomedical scaffolds: Overview and updates, *Front Bioeng Biotechnol* 10 (2022). <https://doi.org/10.3389/fbioe.2022.994355>.
- [2] M.T. Raimondi, S.M. Eaton, M.M. Nava, M. Laganà, G. Cerullo, R. Osellame, Two-Photon Laser Polymerization: From Fundamentals to Biomedical Application in Tissue Engineering and Regenerative Medicine, *J Appl Biomater Funct Mater* 10 (2012) 56–66. <https://doi.org/10.5301/JABFM.2012.9278>.
- [3] C. Greant, B. Van Durme, J. Van Hoorick, S. Van Vlierberghe, Multiphoton Lithography as a Promising Tool for Biomedical Applications, *Adv Funct Mater* (2023). <https://doi.org/10.1002/adfm.202212641>.
- [4] A. Ovsianikov, A. Doraiswamy, R. Narayan, B.N. Chichkov, Two-photon polymerization for fabrication of biomedical devices, in: *Microfluidics, BioMEMS, and Medical Microsystems V*, SPIE, 2007: p. 64650O. <https://doi.org/10.1117/12.699979>.
- [5] C. Liao, A. Wuethrich, M. Trau, A material odyssey for 3D nano/microstructures: two photon polymerization based nanolithography in bioapplications, *Appl Mater Today* 19 (2020) 100635. <https://doi.org/10.1016/j.apmt.2020.100635>.
- [6] J.R. Thompson, K.S. Worthington, B.J. Green, N.K. Mullin, C. Jiao, E.E. Kaalberg, L.A. Wiley, I.C. Han, S.R. Russell, E.H. Sohn, C.A. Guymon, R.F. Mullins, E.M. Stone, B.A. Tucker, Two-photon polymerized poly(caprolactone) retinal cell delivery scaffolds and their systemic and retinal biocompatibility, *Acta Biomater* 94 (2019) 204–218. <https://doi.org/10.1016/j.actbio.2019.04.057>.
- [7] P. Timashev, D. Kuznetsova, A. Koroleva, N. Prodanets, A. Deiwick, Y. Piskun, K. Bardakova, N. Dzhoyashvili, S. Kostjuk, E. Zagaynova, Y. Rochev, B. Chichkov, V. Bagratashvili, Novel Biodegradable Star-Shaped Polylactide Scaffolds for Bone Regeneration Fabricated By Two-Photon Polymerization, *Nanomedicine* 11 (2016) 1041–1053. <https://doi.org/10.2217/nnm-2015-0022>.
- [8] C. LaFratta, T. Baldacchini, Two-Photon Polymerization Metrology: Characterization Methods of Mechanisms and Microstructures, *Micromachines (Basel)* 8 (2017) 101. <https://doi.org/10.3390/mi8040101>.
- [9] P.F.J. van Altena, A. Accardo, Micro 3D Printing Elastomeric IP-PDMS Using Two-Photon Polymerisation: A Comparative Analysis of Mechanical and Feature Resolution Properties, *Polymers (Basel)* 15 (2023) 1816. <https://doi.org/10.3390/polym15081816>.
- [10] L. Angeloni, M. Ganjian, M. Nouri-Goushki, M.J. Mirzaali, C.W. Hagen, A.A. Zadpoor, L.E. Fratila-Apachitei, M.K. Ghatkesar, Mechanical characterization of nanopillars by atomic force microscopy, *Addit Manuf* 39 (2021) 101858. <https://doi.org/10.1016/j.addma.2021.101858>.

- [11] S. Schweiger, T. Schulze, S. Schlipf, P. Reinig, H. Schenk, Characterization of two-photon-polymerization lithography structures via Raman spectroscopy and nanoindentation, *Journal of Optical Microsystems* 2 (2022) 33501. <https://doi.org/10.1117/1.JOM.2.3.033501>
- [12] F. Zurita, L. Grob, A. Erben, F. Del Duca, H. Clausen-Schaumann, S. Sudhop, O. Hayden, B. Wolfrum, Fully 3D-Printed Cuff Electrode for Small Nerve Interfacing, *Adv Mater Technol* 8 (2023). <https://doi.org/10.1002/admt.202200989>.
- [13] L. Jonušauskas, D. Gailevičius, S. Rekštytė, T. Baldacchini, S. Juodkasis, M. Malinauskas, Mesoscale laser 3D printing, *Opt Express* 27 (2019) 15205. <https://doi.org/10.1364/OE.27.015205>.
- [14] A. Isaakidou, I. Apachitei, L.E. Fratila-Apachitei, A.A. Zadpoor, High-Precision 3D Printing of Microporous Cochlear Implants for Personalized Local Drug Delivery, *J Funct Biomater* 14 (2023) 494. <https://doi.org/10.3390/jfb14100494>.
- [15] R.C.L.N. Kramer, E.J. Verlinden, L. Angeloni, A. van den Heuvel, L.E. Fratila-Apachitei, S.M. van der Maarel, M.K. Ghatkesar, Multiscale 3D-printing of microfluidic AFM cantilevers, *Lab Chip* 20 (2020) 311-319. <https://doi.org/10.1039/C9LC00668K>.
- [16] A.-I. Bunea, N. del Castillo Iniesta, A. Droumpali, A.E. Wetzel, E. Engay, R. Taboryski, Micro 3D Printing by Two-Photon Polymerization: Configurations and Parameters for the Nanoscribe System, *Micro* 1 (2021) 164-180. <https://doi.org/10.3390/micro1020013>.
- [17] M. Oellers, F. Lucklum, M.J. Vellekoop, On-chip mixing of liquids with swap structures written by two-photon polymerization, *Microfluid Nanofluidics* 24 (2020) 4. <https://doi.org/10.1007/s10404-019-2309-8>.
- [18] E. Fakeih, A.A. Aguirre-Pablo, S.T. Thoroddsen, K.N. Salama, Fabrication and Characterization of Porous Microneedles for Enhanced Fluid Injection and Suction: A Two-Photon Polymerization Approach, *Adv Eng Mater* 25 (2023). <https://doi.org/10.1002/adem.202300161>.
- [19] A.S. Cordeiro, I.A. Tekko, M.H. Jomaa, L. Vora, E. McAlister, F. Volpe-Zanutto, M. Nethery, P.T. Baine, N. Mitchell, D.W. McNeill, R.F. Donnelly, Two-Photon Polymerisation 3D Printing of Microneedle Array Templates with Versatile Designs: Application in the Development of Polymeric Drug Delivery Systems, *Pharm Res* 37 (2020) 174. <https://doi.org/10.1007/s11095-020-02887-9>.
- [20] S. Mckee, A. Lutey, C. Sciancalepore, F. Poli, S. Selli, A. Cucinotta, Microfabrication of polymer microneedle arrays using two-photon polymerization, *J Photochem Photobiol B* 229 (2022) 112424. <https://doi.org/10.1016/j.jphotobiol.2022.112424>.

- [21] S. Czich, T. Wloka, H. Rothe, J. Rost, F. Penzold, M. Kleinsteuber, M. Gottschaldt, U.S. Schubert, K. Liefeth, Two-Photon Polymerized Poly(2-Ethyl-2-Oxazoline) Hydrogel 3D Microstructures with Tunable Mechanical Properties for Tissue Engineering, *Molecules* 25 (2020) 5066. <https://doi.org/10.3390/molecules25215066>.
- [22] Y. Yuan, L. Chen, Z. Shi, J. Chen, Micro/Nanoarchitectonics of 3D Printed Scaffolds with Excellent Biocompatibility Prepared Using Femtosecond Laser Two-Photon Polymerization for Tissue Engineering Applications, *Nanomaterials* 12 (2022) 391. <https://doi.org/10.3390/nano12030391>.
- [23] E. Juère, R. Caillard, F. Kleitz, Pore confinement and surface charge effects in protein-mesoporous silica nanoparticles formulation for oral drug delivery, *Microporous and Mesoporous Materials* 306 (2020) 110482. <https://doi.org/10.1016/j.micromeso.2020.110482>.
- [24] J. Parra-Nieto, M.A.G. del Cid, I.A. de Cárcer, A. Baeza, Inorganic Porous Nanoparticles for Drug Delivery in Antitumoral Therapy, *Biotechnol J* 16 (2021). <https://doi.org/10.1002/biot.202000150>.
- [25] A. Isaakidou, M. Ganjian, R. van Hoften, M.C. Saldivar, M.A. Leeflang, A. Groetsch, M. Wątroba, J. Schwiedrzik, M.J. Mirzaali, I. Apachitei, L.E. Fratila-Apachitei, A.A. Zadpoor, Multi-scale *in silico* and *ex silico* mechanics of 3D printed cochlear implants for local drug delivery, *Front Bioeng Biotechnol* 11 (2024). <https://doi.org/10.3389/fbioe.2023.1289299>.
- [26] G. Rochat, Y. Leterrier, P. Fayet, J.-A.E. Manson, Mechanical analysis of ultrathin oxide coatings on polymer substrates *in situ* in a scanning electron microscope, *Thin Solid Films* 437 (2003) 204–210. [https://doi.org/10.1016/S0040-6090\(03\)00613-8](https://doi.org/10.1016/S0040-6090(03)00613-8).
- [27] M. Kwaśny, A. Bombalska, K. Obroniecka, A Reliable Method of Measuring the Conversion Degrees of Methacrylate Dental Resins, *Sensors* 22 (2022) 2170. <https://doi.org/10.3390/s22062170>.
- [28] J. Pyszkowski, K. Bielawski, Piuma Nanoindenter - User Manual, *Optics11* (2019). <https://www.optics11life.com/piuma>.
- [29] S. Juodkazis, V. Mizeikis, K.K. Seet, H. Misawa, U.G.K. Wegst, Mechanical properties and tuning of three-dimensional polymeric photonic crystals, *Appl Phys Lett* 91 (2007). <https://doi.org/10.1063/1.2822825>.
- [30] A.G. Clark, R. Wang, Y. Qin, Y. Wang, A. Zhu, J. Lomeo, Q. Bao, D.J. Burgess, J. Chen, B. Qin, Y. Zou, S. Zhang, Assessing microstructural critical quality attributes in PLGA microspheres by FIB-SEM analytics, *Journal of Controlled Release* 349 (2022) 580–591. <https://doi.org/10.1016/j.jconrel.2022.06.066>.
- [31] T. Maconachie, R. Tino, B. Lozanovski, M. Watson, A. Jones, C. Pandelidi, A. Alghamdi, A. Almalki, D. Downing, M. Brandt, M. Leary, The compressive behaviour of ABS gyroid lattice structures manufactured by fused deposition

- modelling, *The International Journal of Advanced Manufacturing Technology* 107 (2020) 4449-4467. <https://doi.org/10.1007/s00170-020-05239-4>.
- [32] G. Flamourakis, Q. Dong, D. Kromm, S. Teurlings, J. van Haren, T. Allertz, H. Smeenk, F.M.S. de Vrij, R.P. Tas, C.S. Smith, D. Brinks, A. Accardo, Deciphering the Influence of Effective Shear Modulus on Neuronal Network Directionality and Growth Cones' Morphology via Laser-Assisted 3D-Printed Nanostructured Arrays, *Adv Funct Mater* 35 (2025). <https://doi.org/10.1002/adfm.202409451>.
- [33] C.-S. Shin, T.-J. Li, C.-L. Lin, Alleviating Distortion and Improving the Young's Modulus in Two-Photon Polymerization Fabrications, *Micromachines (Basel)* 9 (2018) 615. <https://doi.org/10.3390/mi9120615>.
- [34] E.D. Lemma, F. Rizzi, T. Dattoma, B. Spagnolo, L. Sileo, A. Quattieri, M. De Vittorio, F. Pisanello, Mechanical properties tunability of three-dimensional polymeric structures in two-photon lithography, *IEEE Trans Nanotechnol* (2016) 1-1. <https://doi.org/10.1109/TNANO.2016.2625820>.
- [35] M. Diamantopoulou, N. Karathanasopoulos, D. Mohr, Stress-strain response of polymers made through two-photon lithography: Micro-scale experiments and neural network modeling, *Addit Manuf* 47 (2021) 102266. <https://doi.org/10.1016/j.addma.2021.102266>.
- [36] J. Bauer, A.G. Izard, Y. Zhang, T. Baldacchini, L. Valdevit, Thermal post-curing as an efficient strategy to eliminate process parameter sensitivity in the mechanical properties of two-photon polymerized materials, *Opt Express* 28 (2020) 20362. <https://doi.org/10.1364/OE.395986>.
- [37] H. Wang, W. Zhang, D. Ladika, H. Yu, D. Gailevičius, H. Wang, C. Pan, P.N.S. Nair, Y. Ke, T. Mori, J.Y.E. Chan, Q. Ruan, M. Farsari, M. Malinauskas, S. Juodkazis, M. Gu, J.K.W. Yang, Two-Photon Polymerization Lithography for Optics and Photonics: Fundamentals, Materials, Technologies, and Applications, *Adv Funct Mater* 33 (2023). <https://doi.org/10.1002/adfm.202214211>.
- [38] X. Zhou, Y. Hou, J. Lin, A review on the processing accuracy of two-photon polymerization, *AIP Adv* 5 (2015). <https://doi.org/10.1063/1.4916886>.
- [39] R. Cunha, J.V.P. Valverde, L. De Boni, L. Misoguti, C.R. Mendonça, Nonlinear Refraction and Absorption in Polymers Used for Femtosecond Direct Laser Writing, *ACS Omega* 10 (2025) 1440-1447. <https://doi.org/10.1021/acsomega.4c09152>.
- [40] D. Ladika, A. Butkus, V. Melissinaki, E. Skliutas, E. Kabouraki, S. Juodkazis, M. Farsari, M. Malinauskas, X-photon 3D lithography by fs-oscillators: wavelength-independent and photoinitiator-free, *Light: Advanced Manufacturing* 5 (2024) 567. <https://doi.org/10.37188/lam.2024.048>.

3.6. SUPPORTING INFORMATION

3.6.1. STATISTICAL EXPLORATION AND ANALYSIS

Shapiro-Wilk normality tests were performed on the data for the solid and porous versions of the microstructures made by IP-Q, IP-S, and IP-PDMS as part of the statistical analysis. The normality test results are presented in QQ-normality plots and the resulting p-values in **Figure S3.1**. The results of the t-tests are presented in **Table S3.1**.

A Hodges-Lehmann estimator for the stiffness values of the porous and solid IP-PDMS microstructures was calculated as follows:

$$HL(p, b) = \text{median}_{1 \leq i \leq n, 1 \leq j \leq m} (p_i - b_j) \quad (\text{Eq. S3.1})$$

where p and b are the stiffness of the porous and solid IP-PDMS microstructures, respectively, and $n = m = 3$. The Hodges-Lehmann estimator is 4.69, which is substantial given that it represents between 43% and 88% of the stiffness values.

3.6.2. CALCULATION OF THE THEORETICAL (DESIGNED) POROSITY AND RELATIVE DENSITY OF THE MICROSTRUCTURES

The porosity, φ , of the porous microstructures was calculated as follows:

$$\varphi = \left(1 - \frac{V_P}{V_T}\right) \times 100\% \quad (\text{Eq. S3.2})$$

where V_T is the volume of the solid structure (μm^3), V_P is the volume of the porous structure (μm^3), and φ is the resulting porosity of the structure (%). The digital designs were used to calculate the theoretical porosity. Consequently, the relative density, $\rho_r = \rho^*/\rho_{\text{solid}}$, thus the density of a porous material (ρ^*) to the density of the same material when it is fully dense (ρ_{solid}), was derived as follows:

$$\rho_r = \rho^*/\rho_{\text{solid}} = \frac{V_P}{V_T} \quad (\text{Eq. S3.3})$$

The geometry and sizes of the printed microstructures is presented in **Table S3.2** and the calculation of the theoretical porosity and the relative density of the microstructures in **Table S3.3**.

3.6.3. GEOMETRY (DIAMETER, HEIGHT) OF THE 2PP-PRINTED MICROPILLARS AND CALCULATION OF THE DEVIATION WITH RESPECT TO THE DESIGNED GEOMETRY

3.6.4. CHEMICAL COMPOSITION OF IP-Q, IP-S, IP-PDMS

The chemical composition analyses results are presented in **Table S3.7-9**.

3.6.5. EXPOSURE CONDITIONS AND CALCULATED PHYSICAL PARAMETERS

The exposure conditions and calculated physical parameters are presented in **Table S3.10-12**.

LIST OF SUPPORTING TABLES

Table S3.1. T-test results for the stiffness (N/m) of solid and porous IP-Q, IP-S, and IP-PDMS structures. The notation for $p < 0.05$ is one asterisk (*), for $p < 0.01$, two asterisks (**), for $p < 0.001$, three asterisks (***), and for $p < 0.0001$, four asterisks (****).

	IP-Q porous vs. solid	IP-S porous vs. solid	IP-PDMS porous vs. solid
Test type	Unpaired t-test	Unpaired t-test	Mann-Whitney test
p-value	<0.0001 (0.00004735)	<0.0001 (0.00001445)	0.1000
p-value summary	****	****	ns
Significantly different?	yes	yes	no

Table S3.2. Summary of one-way ANOVA results for the stiffness (N/m) of solid and porous IP-Q, IP-S, and IP-PDMS structures.

ANOVA summary	
F	46309
P value	<0,0001
P value summary	****
Significant diff. among means (P < 0.05)?	Yes
R squared	0,9999

Table S3.3. Tukey’s multiple comparisons test for the stiffness (N/m) of solid and porous structures fabricated from IP-Q, IP-S, and IP-PDMS. Significant pairwise differences are indicated with adjusted p values.

Tukey's multiple comparisons test	Mean diff	Below threshold?	Summary	Adjusted P value
IP-Q solid vs. IP-Q porous	0,07229	Yes	***	0,0008
IP-Q solid vs. IP-S solid	-0,01053	No	ns	0,9495
IP-Q solid vs. IP-S porous	0,08704	Yes	***	0,0001
IP-Q solid vs. IP-PDMS solid	3,511	Yes	****	<0,0001
IP-Q solid vs. IP-PDMS porous	3,778	Yes	****	<0,0001
IP-Q porous vs. IP-S solid	-0,08281	Yes	***	0,0002
IP-Q porous vs. IP-S porous	0,01475	No	ns	0,8271
IP-Q porous vs. IP-PDMS solid	3,439	Yes	****	<0,0001
IP-Q porous vs. IP-PDMS porous	3,706	Yes	****	<0,0001
IP-S solid vs. IP-S porous	0,09756	Yes	****	<0,0001
IP-S solid vs. IP-PDMS solid	3,521	Yes	****	<0,0001
IP-S solid vs. IP-PDMS porous	3,789	Yes	****	<0,0001
IP-S porous vs. IP-PDMS solid	3,424	Yes	****	<0,0001
IP-S porous vs. IP-PDMS porous	3,691	Yes	****	<0,0001
IP-PDMS solid vs. IP-PDMS porous	0,2675	Yes	****	<0,0001

Table S3.4. Dimensions of the solid and porous microscale structures fabricated from IP-Q, IP-S, and IP-PDMS, as investigated by SEM. The designed dimension is included in the bracket next to the measured value.

	IP-Q (solid)	IP-Q (porous)	IP-S (solid)	IP-S (porous)	IP- PDMS (solid)	IP- PDMS (porous)
Tip diameter (µm)	49.9 (50)	48.3 (50)	50.4 (50)	49.0 (50)	47.9 (50)	48.6 (50)
Cuboid side (µm)	85.8 (86)	84.1(86)	90.9 (86)	84.4 (86)	77.4 (86)	76.4 (86)
Cylinder length (µm)	120.5	125.0	120.5	125.1	122.6	87.8
	(171.5)	(171.5)	(171.5)	(171.5)	(171.5)	(171.5)
Cuboid length (µm)	175.3	176.6	178.7	179.3	154.8	145.0
	(171.5)	(171.5)	(171.5)	(171.5)	(171.5)	(171.5)
Total length (µm)	295.8	301.6	298.7	304.4	277.4	232.8
	(343)	(343)	(343)	(343)	(343)	(343)

Table S3.5. Theoretical porosity (φ) and relative density (ρ_r) of the samples.

	Solid (theoretical)	Porous (theoretical)
Volume of the solid structure, $V_T(\mu\text{m}^3)$	1510000	-
Volume of the porous structure, $V_P(\mu\text{m}^3)$	0	1110000
Porosity, φ (%)	0	26
Relative density, ρ_r (-)	1	0.74

Table S3.6. Calculations of the geometrical deviations in diameter and height of the micropillars with respect to the designed geometry ($D = 50 \mu\text{m}$, $H = 100 \mu\text{m}$).

	s (μm)	LP		LP		LP		LP		LP	
		(mW)		(mW)		(mW)		(mW)		(mW)	
		20		30		40		50		60	
Micropillar diameter (μm)	1.2	22.2	56%	31.4	37%	36.70	27%	38.00	24%	39.20	22%
	2.4	14.1	72%	28.5	43%	34.2	32%	36	28%	38.3	23%
	3.7	7.27	85%	24.6	51%	30.5	39%	34.6	31%	36.9	26%
	5	2.04	96%	23.2	54%	29.4	41%	33	34%	35.3	29%
	6.2	2.65	95%	19.7	61%	29.1	42%	31.9	36%	34.4	31%
	7.5	N.A.	N.A.	15.7	69%	26.6	47%	31.4	37%	36.2	28%
Micropillar height (μm)	1.2	74.1	26%	90.6	9%	102.3	-2%	103.1	-3%	104.6	-5%
	2.4	55	45%	78.7	21%	91.7	8%	100.1	0%	103.6	-4%
	3.7	13.8	86%	72.1	28%	85	15%	97.3	3%	100.1	0%
	5	24.2	76%	70.4	30%	86.2	14%	82.9	17%	79.8	20%
	6.2	9.6	90%	66.9	33%	82.9	17%	95.3	5%	99.8	0%
	7.5	9	91%	61	39%	79.8	20%	91.8	8%	92.1	8%
	h (μm)	LP		LP		LP		LP		LP	
		(mW)		(mW)		(mW)		(mW)		(mW)	
		20		30		40		50		60	
Micropillar diameter (μm)	0.4	18.3	63%	34.1	32%	37.7	25%	40.9	18%	41.1	18%
	1.0	0.5	99%	24.5	51%	32.5	35%	36.5	27%	38.5	23%
	1.6	N.A.	N.A.	16.8	66%	28.6	43%	34.1	32%	36.8	26%
	2.2	N.A.	N.A.	N.A.	N.A.	25	50%	31	38%	33.2	34%
	2.8	N.A.	N.A.	N.A.	N.A.	21.4	57%	29.6	41%	26.4	47%
	3.4	N.A.	N.A.	N.A.	N.A.	16.3	67%	26.4	47%	31.7	37%
Micropillar height (μm)	0.4	60.1	40%	87.6	12%	100.9	-1%	105	-5%	109	-9%
	1.0	16.9	83%	73.4	27%	86	14%	99.2	1%	100.1	0%
	1.6	N.A.	N.A.	62.2	38%	80.8	19%	90.16	10%	97.6	2%
	2.2	N.A.	N.A.	N.A.	N.A.	75.9	24%	86.4	14%	95.2	5%
	2.8	N.A.	N.A.	N.A.	N.A.	49.5	51%	83.2	17%	72.5	28%
	3.4	N.A.	N.A.	N.A.	N.A.	77	23%	78.4	22%	85.7	14%

Table S3.7. Composition/information on IP-Q, IP-S, and IP-PDMS components, as provided in the manufacturer's material safety data sheet.

Resin	CAS No.	Chemical name	Amount
IP-Q	72869-86-4	Diurethane dimethacrylate, mixture of isomers	>95%
	128-37-0	Butylated hydroxytoluene	<1%
IP-S	NaN	Carbamate-, methacrylate, mixture	>95%
	NaN	Butyrolactone	<5%
	158061-40-6	[15-20% (acryloxypropyl)methylsiloxane] dimethylsiloxane copolymer	>90%
IP-PDMS	1116-76-3	Tri-n-octylamine	>5%
	128754-61-0	(3-acryloxy-2-hydroxypropoxypropyl) terminated polydimethylsiloxane	<5%

Table S3.8. Expected FTIR peaks before and after polymerization for the individual components of IP-Q, IP-S, and IP-PDMS, based on the components provided in the manufacturer's material safety data sheet.

Resin	Chemical name	FTIR peaks before polymerization (cm ⁻¹)	FTIR peaks after polymerization (cm ⁻¹)
IP-Q	Diurethane dimethacrylate, mixture of isomers	C=C: 1635-1640 C=O: 1720-1740 N-H: 3300-3500 C-O: 1000-1300	C=O: 1720-1740 N-H: 3300-3500 C-O: 1000-1300
	Butylated hydroxytoluene	O-H: 3200-3600	O-H: 3200-3600
IP-S	Carbamate-, methacrylate, mixture	C=C: 1635-1640 C=O: 1720-1740 N-H: 3300-3500 C-O: 1000-1300	C=O: 1720-1740 N-H: 3300-3500 C-O: 1000-1300
	Butyrolactone	C=O: 1750	C=O: 1750
	Photoinitiator based on aromatic ketones	C-H: 3000-3100	C-H: 3000-3100
IP-PDMS	[15-20% (acryloxypropyl)methylsiloxane] dimethylsiloxane copolymer	Si-C=C: 1400-1450 C=O: 1720-1740 Si-O-Si: 1000-1100	C=O: 1720-1740 Si-O-Si: 1000-1100
	Tri-n-octylamine	N-H: 3300-3500	N-H: 3300-3500
	(3-acryloxy-2-hydroxypropoxypropyl) terminated	C=C: 1635-1640 C=O: 1720-1740 O-H: 3200-3600	C=C: 1635-1640 C=O: 1720-1740 O-H: 3200-3600
	polydimethylsiloxane		

Table S3.9. Relevant peak heights used to calculate the degree of conversion (DC) for IP-Q, IP-S, and IP-PDMS.

Resin	Wavenumber (cm⁻¹)	A_R (a.u.)	A_P (a.u.)	DC (%)
IP-Q	1637	0.022	0.012	45.5
IP-S	1637	0.194	0.082	57.8
IP-PDMS	1407	0.112	0.041	63.2

Table S3.10. Calculated laser exposure parameters for microstructures fabricated from IP-Q, IP-S, and IP-PDMS.

Microstructures									
Material	Laser Power (mW)	Intensity (W/cm ²)	Fluence per pulse (J/cm ²)	Number of pulses per voxel	Exposure dose (J/cm ²)	Focal spot, d _{xy} (μm)	Rayleigh length, z _R (μm)	Voxel overlap, δ (-)	
IP-Q	20	6.33 × 10 ¹⁰	3.16 × 10 ⁻⁰³	2718296	8599.64	3.17	10.13	0.92	
	30	9.49 × 10 ¹⁰	4.75 × 10 ⁻⁰³		12899.47				
	40	1.27 × 10 ¹¹	6.33 × 10 ⁻⁰³		17199.29				
IP-S	20	4.50 × 10 ¹¹	2.25 × 10 ⁻⁰²		1209.33				
	30	6.75 × 10 ¹¹	3.37 × 10 ⁻⁰²	53755	1813.99	1.19	1.42	0.72	
	40	9.00 × 10 ¹¹	4.50 × 10 ⁻⁰²		2418.65				
IP-PDMS	35	7.87 × 10 ¹¹	3.94 × 10 ⁻⁰²		793.62				
	42.5	9.56 × 10 ¹¹	4.78 × 10 ⁻⁰²	20158	963.68	1.19	1.42	0.48	
	50	1.12 × 10 ¹²	5.62 × 10 ⁻⁰²		1133.74				

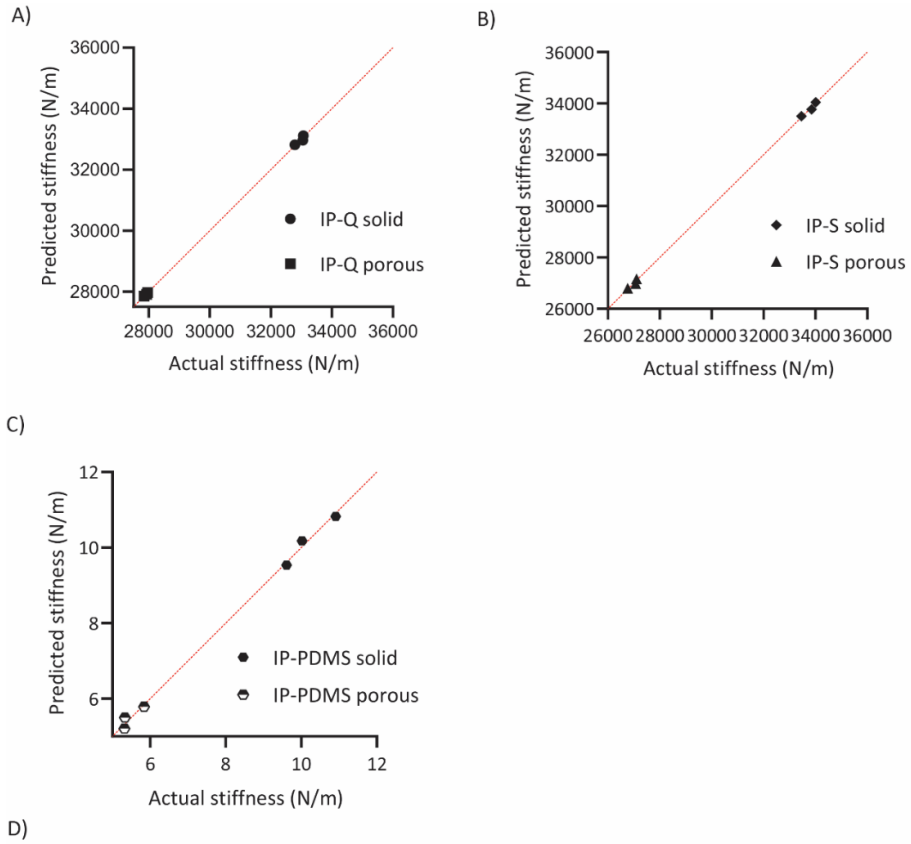
Table S3.11. Calculated laser exposure parameters for micropillars (constant slicing distance, s) fabricated from IP-Q.

Micropillars (constant s)									
Material	Laser Power (mW)	Intensity (W/cm^2)	Fluence per pulse (J/cm^2)	Number of pulses per voxel	Exposure dose (J/cm^2)	Focal spot, d_{xy} (μm)	Rayleigh length, z_R (μm)	Voxel overlap, δ (-)	
IP-Q	20	6.33×10^{10}	2.50×10^{10}	81549	257.99			0.44	
				32620	103.20			0.35	
				20387	64.50			0.25	
				14827	46.91			0.16	
				11650	36.86			0.06	
				9594	30.35			-0.04	
	30	9.49×10^{10}	3.75×10^{10}	81549	386.98			0.44	
				32620	154.79			0.35	
				20387	96.75			0.25	
				14827	70.36			0.16	
				11650	55.28			0.06	
				9594	45.53			-0.04	
40	1.27×10^{11}	5.00×10^{10}	81549	515.98			0.44		
			32620	206.39			0.35		
			20387	128.99		3.17	0.25		
			14827	93.81		10.13	0.16		
			11650	73.71			0.06		
			9594	60.70			-0.04		
50	1.58×10^{11}	6.25×10^{10}	81549	644.97			0.44		
			32620	257.99			0.35		
			20387	161.24			0.25		
			14827	117.27			0.16		
			11650	92.14			0.06		
			9594	75.88			-0.04		
60	1.90×10^{11}	7.50×10^{10}	81549	773.97			0.44		
			32620	309.59			0.35		
			20387	193.49			0.25		
			14827	140.72			0.16		
			11650	110.57			0.06		
			9594	91.06			-0.04		

Table S3.12. Calculated laser exposure parameters for micropillars (constant hatching distance, h) fabricated from IP-Q.

Micropillars (constant h)									
Material	Laser Power (mW)	Intensity (W/cm^2)	Fluence per pulse (J/cm^2)	Number of pulses per voxel	Exposure Dose (J/cm^2)	Focal spot, d_{xy} (μm)	Rayleigh length, z_R (μm)	Voxel overlap, δ (-)	
IP-Q	20	6.33×10^{10}	2.50×10^{10}	135915	429.98			0.60	
				65239	206.39			0.52	
				44080	139.45			0.43	
				32620	103.20			0.35	
	30	9.49×10^{10}	3.75×10^{10}	26306	83.22			0.27	
				21746	68.80			0.18	
				135915	644.97			0.60	
				65239	309.59			0.52	
	40	1.27×10^{11}	5.00×10^{10}	44080	209.18			0.43	
				32620	154.79			0.35	
				26306	124.83			0.27	
				21746	103.20			0.18	
50	1.58×10^{11}	6.25×10^{10}	135915	859.96			0.60		
			65239	412.78			0.52		
			44080	278.91	3.17	10.13	0.43		
			32620	206.39			0.35		
60	1.90×10^{11}	7.50×10^{10}	26306	166.44			0.27		
			21746	137.59			0.18		
			135915	1074.96			0.60		
			65239	515.98			0.52		
				44080	348.63			0.43	
				32620	257.99			0.35	
				26306	208.06			0.27	
				21746	171.99			0.18	
				135915	1289.95			0.60	
				65239	619.17			0.52	
				44080	418.36			0.43	
				32620	309.59			0.35	
				26306	249.67			0.27	
				21746	206.39			0.18	

LIST OF SUPPORTING FIGURES



D)

Shapiro-Wilk Test Results						
	IP-Q solid	IP-Q porous	IP-S solid	IP-S porous	IP-PDMS solid	IP-PDMS porous
p-value	0.0604	0.5107	0.5521	0.1652	0.5989	0.0321
Passed normality test?	yes	yes	yes	yes	yes	no

Figure S3.1. QQ normality plots for the stiffness (N/m) of solid and porous (A) IP-Q, (B) IP-S, and (C) IP-PDMS structures. (D) Shapiro-Wilk Test Results.

3. MICROMECHANICS OF 3D PRINTED MICROSTRUCTURES

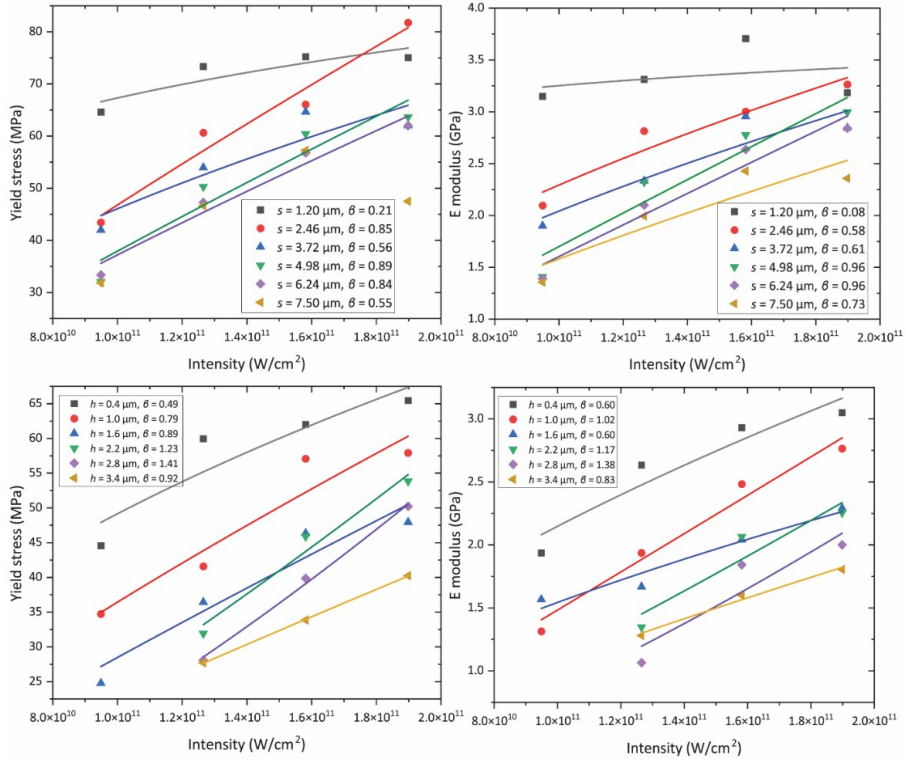
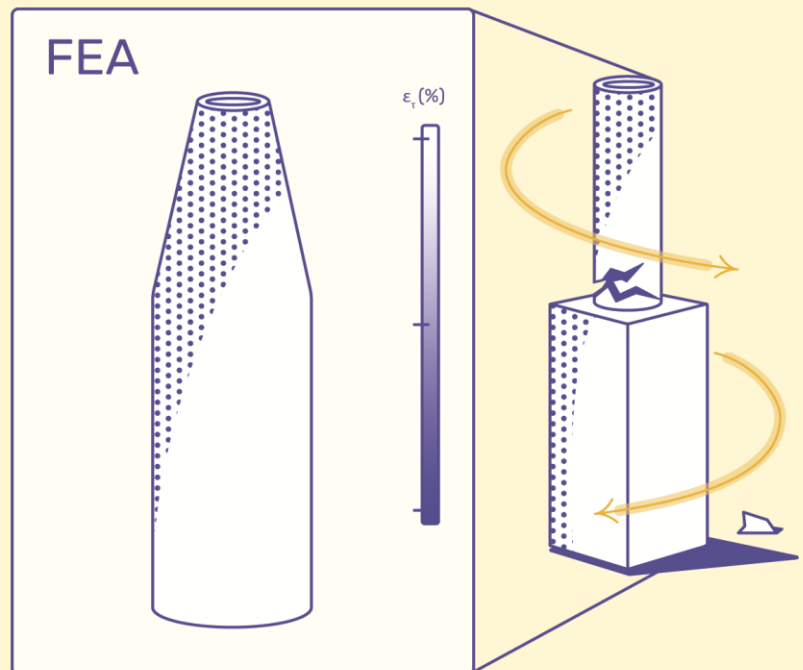


Figure S3.2. Mechanical properties (Yield strength σ_y , and Young's modulus E) as a function of peak laser intensity for the IP-Q micropillars. Each dataset is fitted with a power law: $E, \sigma_y \propto I^\beta$, where β appears mostly less than 1, indicating a sublinear dependence of polymerization efficiency on intensity for most of the cases.

Macromechanics & Computational Analysis



4. MECHANICS OF POROUS COCHLEAR IMPLANTS

Abstract

The currently available treatments for inner ear disorders often involve systemic drug administration, leading to suboptimal drug concentrations and side effects. Cochlear implants offer a potential solution by providing localized and sustained drug delivery to the cochlea. While the mechanical characterization of both the implants and their constituent material is crucial to ensure functional performance and structural integrity during implantation, this aspect has been mostly overlooked. This study proposes a novel methodology for the mechanical characterization of our recently developed cochlear implant design, namely rectangular (R) and cylindrical (C), fabricated using two-photon polymerization (2PP) with a novel photosensitive resin (IP-Q). We, therefore, used *in silico* computational models and *ex silico* experiments to study the mechanics of our newly designed implants when subjected to torsion as a result of the foreseeable implantation procedure. Torsion testing on the actual-sized implants was not feasible due to their small size ($0.6 \times 0.6 \times 2.4 \text{ mm}^3$). Therefore, scaled-up R-type cochlear implants ($5 \times 5 \times 20 \text{ mm}^3$, $10 \times 10 \times 40 \text{ mm}^3$, and $20 \times 20 \times 80 \text{ mm}^3$) were fabricated using stereolithography (SLA) and were subjected to torsion testing. Finite element analysis (FEA) was employed to simulate torsion testing on those scaled-up implants, and the FEA models accurately represented the linear behavior observed in the torsion tests. We then used the validated FEA models to study the mechanical behavior of real-sized implants fabricated from the IP-Q resin. Mechanical characterization of both implant designs, with different inner porous structures and a hollow version, revealed that the C-type implants exhibited approximately three times higher stiffness and mechanical strength as compared to the R-type implants. The influence of the pore sizes on the mechanical behavior of these implant designs was found to be small. Based on these findings, the C design, regardless of the pore size, is recommended for further research and development efforts.

4.1. INTRODUCTION

The effective delivery of drugs to the inner ear, encompassing the vestibule and cochlea, is impeded by the presence of the blood-labyrinth barrier (BLB) [35]. Although essential for maintaining homeostasis and regulating ion and nutrient transportation, the BLB restricts the entry of high molecular weight compounds, such as drugs, hindering the treatment of inner ear disorders [17,32]. Local drug delivery methods, such as microneedles, intratympanic injections, nanoparticles, stents, silicone-based rods, and implants offer a promising approach to enhance drug bioavailability within the target organ while minimizing the systemic side effects associated with general drug administration [17]. Cochlear implants, with anatomically relevant sizes for the human ear (*i.e.*, $0.6 \times 0.6 \times 2.4 \text{ mm}^3$), incorporating a drug reservoir and an implantable tip, have been recently developed by using two-photon polymerization (2PP) (**Figure 4.1A**) [19]. The implant shapes were rectangular (R) and cylindrical (C) featuring cylindrical tips. These implants feature either an internal interconnected network of square pores in two different sizes (20 μm and 60 μm) (**Figure 4.1B and C**) or a hollow design (**Figure 4.1D**). As a result, six distinct implant designs were created, namely R20, R60, RH, C20, C60, and CH (**Figure 4.1B - D**). The internal porosity serves a dual purpose: first, as a storage space for the specific drug pertaining to the hearing disorder, and second, as a means to regulate the controlled release of the drug into the cochlear labyrinth. Additionally, the implant's structural design and its internal porous features play a vital role in maintaining its mechanical integrity both prior to, during, and following the implantation procedure. The implant size and shape are crucial to fulfilling the anatomical requirements of the cochlea at the implantation site. These implants can be inserted through either the round window (RW) or the oval window (OW) of the cochlea, requiring twisting and insertion into a surgically created aperture (**Figure 4.1E**). As these implants undergo mechanical stresses during implantation, it is crucial to determine their mechanical properties to ensure the safety of the surgical procedure. However, due to their small size, complex geometry, and specific fabrication technique, conventional mechanical testing methods could not easily be used for comprehensive mechanical characterization of such implants. The utilization of the 2PP printing method rendered microscale mechanical testing

difficult due to limitations in the adhesion between the implants and the substrate on which they were printed. Microscale mechanical testing with commercially available micromechanical testing systems has been demonstrated feasible when the samples (micropillars, cantilevers, or dogbones) were prepared using focused ion beam scanning electron microscopy (FIB/SEM) [4,13,21,36]. Numerical modeling for the compression testing of 2PP printed origami architected metamaterials has been also employed to get a better understanding of their mechanical behavior [23]. In this regard, finite element analysis (FEA) offers a numerical approach to simulate the mechanical behavior of cochlear implants during implantation, while experimental validation can be achieved using enlarged implant models. This study represents the first-ever attempt to investigate the mechanical behavior of 3D-printed cochlear implants designed for local drug delivery, as there is no prior mechanical characterization of such implants to be found in the literature. Therefore, *in silico* FEA models for enlarged cochlear implants were developed to investigate their mechanical behavior under compression and torsion. The results were validated against *ex silico* experimental data obtained with enlarged implants printed by stereolithography (SLA). The validated FEA models were then used to help us assess the mechanical properties of real-size cochlear implants and enabled us to choose the most potent design for further studies.

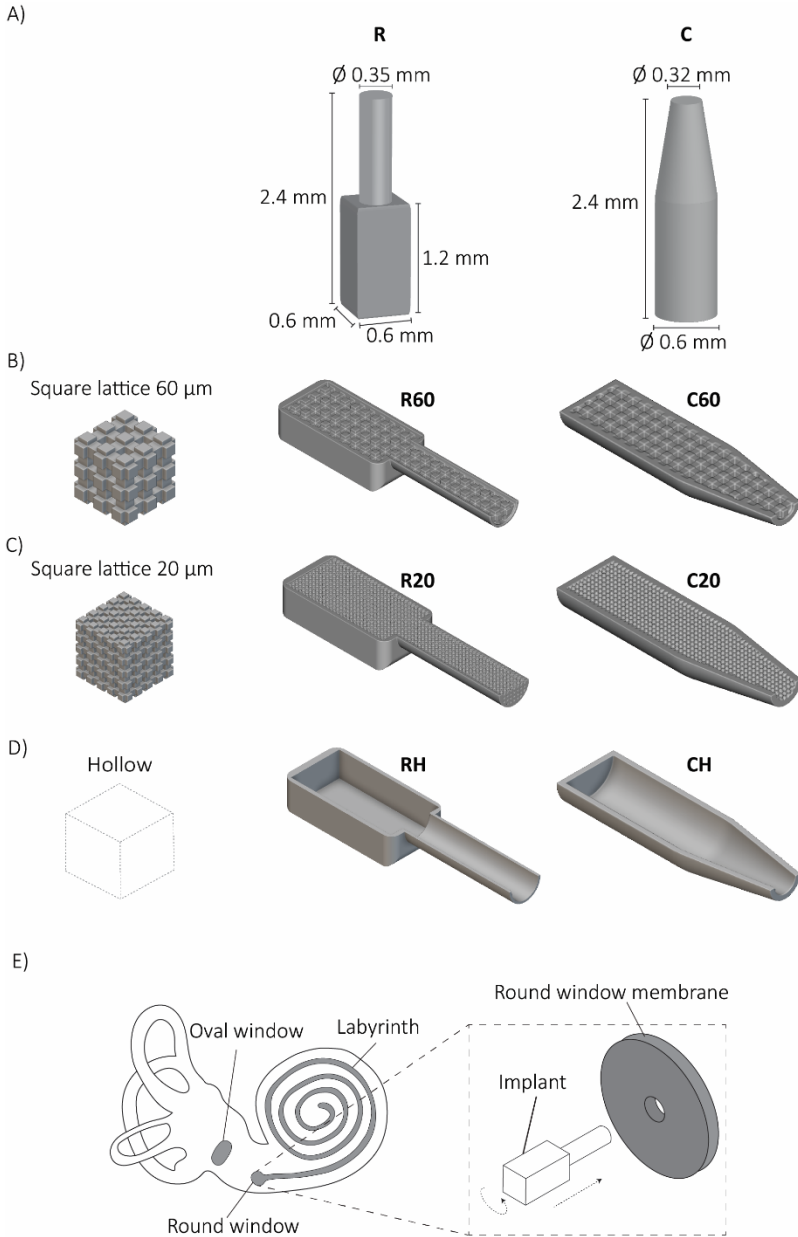


Figure 4.1. The cochlear implants and implantation method. **(A)** The cochlear implant designs with dimensions; rectangular (**R**) and cylindrical (**C**). The lateral views of the **R** and **C** implants with inner porous cubic lattice structures with a unit cell of **(B)** $60 \times 60 \times 60 \mu\text{m}^3$, **(C)** $20 \times 20 \times 20 \mu\text{m}^3$ and **(D)** hollow implants. **(E)** A schematic representation of the anatomy of the inner ear (*i.e.*, cochlea) including the labyrinth, the oval, and round window. The details of the proposed implantation method of the implant to the round window involve a translational and a rotational move.

4.2. MATERIALS AND METHODS

4.2.1. FABRICATION OF THE SPECIMENS FOR COMPRESSION TESTING

4.2.1.1. PRINTED PILLARS PRODUCED BY 2PP

The desired pillar geometry with specific dimensions (diameter = 50 μm , height = 100 μm) was designed using SolidWorks (Dassault Systèmes SE, Vélizy-Villacoublay, France). The design was then exported as a standard tessellation language (STL) file for further processing. The STL file was imported into a job preparation software called Describe (Nanoscribe, Eggenstein-Leopoldshafen, Germany) to facilitate the printing process. Subsequently, the file was transferred to a Photonic Professional GT machine (Nanoscribe, Eggenstein-Leopoldshafen, Germany) for pillar fabrication at the microscale. The printing parameters were set as follows: a laser power of 50 mW, a scanning speed of 100,000 $\mu\text{m}/\text{sec}$, a hatching distance of 1 μm , and a slicing distance of 5 μm . The galvo writing strategy was employed to precisely print the designed pillar structure. To initiate the printing process, a droplet of IP-Q resin (Nanoscribe, Eggenstein-Leopoldshafen, Germany) was carefully deposited onto a silicon substrate. The resin-coated substrate was then subjected to a femtosecond infrared laser beam with a wavelength of 780 nm, which facilitated the printing of the desired pillar structure. After the printing process, the fabricated specimen was immersed in propylene glycol monomethyl ether acetate (PGMEA, Sigma-Aldrich, Hamburg, Germany) for 25 minutes for development. Subsequently, it was rinsed in isopropyl alcohol (Sigma-Aldrich, Hamburg, Germany) for 5 minutes to remove any residual impurities. Finally, the specimen was dried thoroughly using an air-blowing gun. The dimensions of the printed pillars were measured using a high-resolution scanning electron microscopy (SEM) (FEI Helios G4 CX dual-beam workstation, Hillsborough, OR, USA) microscope. The specimens were gold-sputtered using a sputter coater (JFC-1300, JEOL, Akishima, Japan) for 40 sec prior to SEM imaging.

4.2.1.2. ENLARGED PRINTED PILLARS PRODUCED BY SLA

The pillar geometry with the specified dimensions (diameter = 8 mm, height = 16 mm) was created using SolidWorks (Dassault Systèmes SE, Vélizy-Villacoublay, France). The STL file of the design was then imported into the preparation software of the 3D printer (PreForm 3.24.2, Formlabs Inc., Berlin, Germany), which allowed adjustments

to be made for size, structure orientation, and layer thickness. For the printing process, Grey resin (Formlabs Inc, Berlin, Germany) was selected as the material due to its elastic properties, which were expected to closely resemble those of IP-Q. A Form 3+ SLA printer (Formlabs Inc., Berlin, Germany) was utilized to print the pillars in triplicate ($n = 3$). Two different printing orientations were employed, namely horizontal and vertical, to investigate their effects on the resulting structures. Additionally, two different layer thicknesses, namely 25 μm and 50 μm , were utilized to examine their impact on the printed pillars. Upon completion of the printing process, the build platform, containing the printed structures, was carefully removed from the printer. It was then immersed in isopropyl alcohol (IPA) for 10 minutes to remove any residual materials. Subsequently, the printed structures underwent post-curing under UV light at 80 °C for 15 minutes, following the manufacturer's instructions. The final geometry of the printed pillars, including height and diameter, were measured using a caliper with a precision of 0.05 mm. These measurements allowed for the evaluation and characterization of the printed pillar dimensions.

4.2.2. FABRICATION OF ENLARGED 3D PRINTED IMPLANTS FOR TORSION TESTING

In this study, upscaled models of recently developed porous cochlear implant designs [19] were modified and fabricated specifically for torsion testing. Four different specimen types were developed, namely 8R, 16R, 32R, and 32R60, where the letter 'R' represents the implant type (*i.e.*, rectangular), the number preceding it (8, 16, or 32) corresponds to the scaling factor relative to the actual implant size, and the subsequent number after the letter R (if present) indicates the pore size (in μm) in the original porous design (**Figure 4.2A**). To facilitate torsion testing, additional grippers were integrated into both ends of the implants. These grippers were designed using SolidWorks (Dassault Systèmes SE, Vélizy-Villacoublay, France) and were consistent in size across all three upscaled models. The upper gripper, located near the cylindrical part of the implant, was designed as a hexagonal prism with a base edge length (a) of 19.93 mm and a height (h) of 31.88 mm. The lower gripper, situated close to the cuboid part of the implant, was designed as a square prism with the dimensions of 39.85 mm \times 39.85 mm \times 31.88 mm (width \times height \times length) (**Figure 4.2B**). To minimize stress

concentrations at the joints, additional fillets with a radius (r) of 8 mm were incorporated into the design, ensuring a smoother transition from the implant to the grippers. The models were fabricated in triplicate ($n=3$) using the aforementioned SLA system (Form 3B+, Formlabs Inc., Berlin, Germany) with a layer thickness of 50 μm vertically oriented on the built plate. Grey resin was utilized as the printing material, following the methodology described earlier. The resulting geometry of the printed torsion specimens was measured using a caliper with a precision of 0.05 mm (**Table 4.1**).

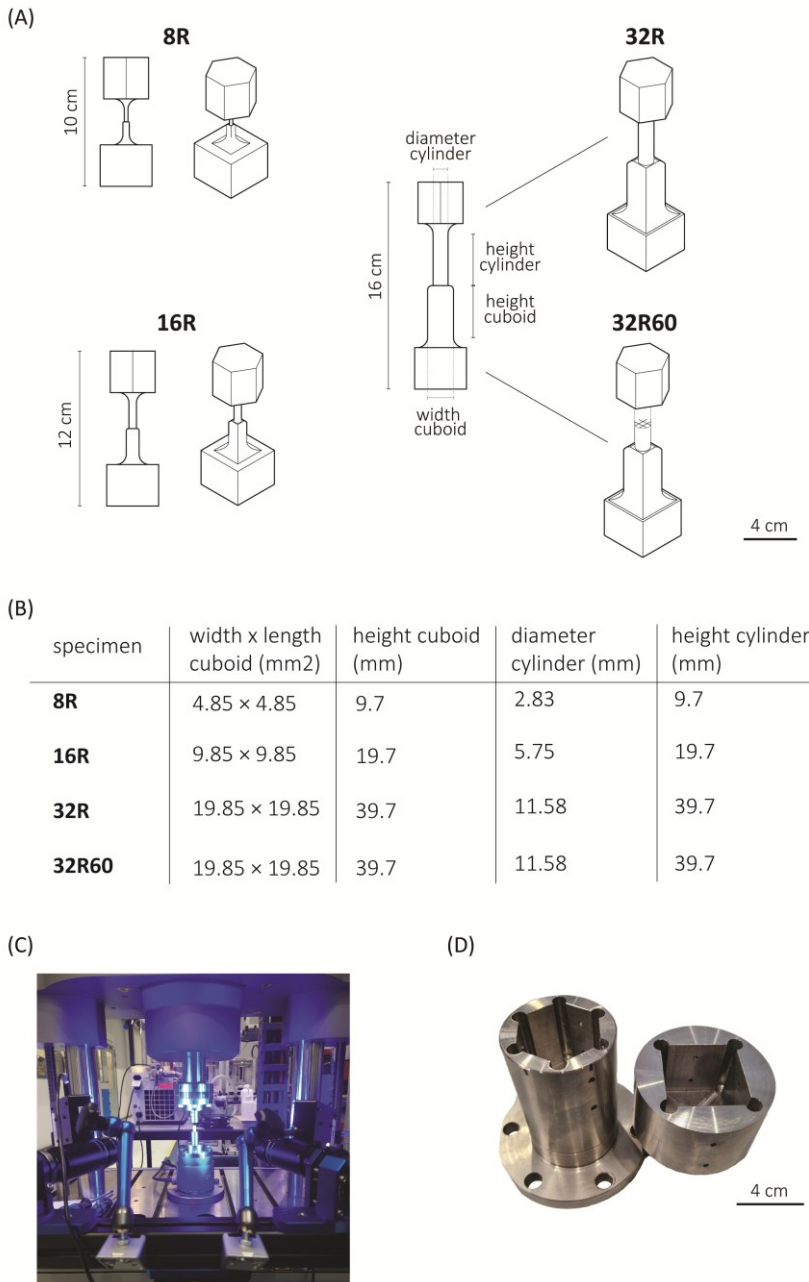


Figure 4.2. (A) The scaled-up R implant designs, including prismatic grippers (top: hexagonal, bottom: square) for torsion testing. (B) The design parameters of the scaled-up R implants for both the solid (8R, 16R, 32R) and porous (32R60) versions. (C) An image of the mechanical testing setup including Electropulse 10,000 and the DIC system. (D) The steel holders with prismatic sockets (top: hexagonal, bottom: square) used in torsion testing.

4.2.3. *IN SILICO* INVESTIGATION OF TORSION SPECIMENS AND COCHLEAR IMPLANTS

FEA simulations were performed using the commercially available Abaqus Standard (Dassault Systèmes Simulia, Vélizy-Villacoublay, France). The torsion testing was modeled for both the enlarged and real-sized implants. Variations with and without grippers as well as solid and porous designs were simulated for the enlarged specimens while variations of solid, hollow, and porous designs with pore sizes of 20 μm and 60 μm were simulated for the real-sized implants. The computational models of the torsion specimens required such inputs as the Young's modulus, Poisson's ratio, true stress, and true plastic strain. The Young's modulus and Poisson's ratio were derived from the compression tests on the Grey resin pillars, while the true stress and true plastic strain were calculated using **Eq. 4.1** and **Eq. 4.2**, respectively. The outputs of the computational models included the forces (torque) and displacements of the structures, which were then converted into true stresses and strains. To assess the accuracy of the models, a comparison was made between the FEA results and the experimental data. The simulation of torsion testing for the R and C types of implants (solid, hollow, and porous) involved a pre-processing step that transformed the STL files into hexahedral element meshes, following the methodology developed and described by Saldivar *et al.* [30]. The mesh density analysis of a cylinder can be found in **Section 4.6** and **Figure S4.1**. Based on the results of this analysis, torsion testing of the specimens was simulated using the selected mesh density. The torque, rotation, shear stress, and shear strain were extracted for analysis.

4.2.4. *EX SILICO* MECHANICAL CHARACTERIZATION

4.2.4.1. COMPRESSION OF THE IP-Q MICROPILLARS

The compression testing of the IP-Q micropillars was performed according to the experimental protocol in **Section 3.2.5**. Briefly, uniaxial quasi-static compression was conducted using a commercial ex-situ indenter setup (Alemnis AG, Thun, Switzerland) equipped with a flat punch diamond tip of 50 μm diameter. The tests were terminated at a maximum displacement of 30 μm . Engineering stress and strain were calculated as described in **Section 3.2.5**, and the Young's modulus was extracted from the initial linear elastic regime (10-15%) of the stress-strain curves.

4.2.4.2. COMPRESSION AND TORSION OF THE GREY RESIN PRINTED SPECIMENS

Compression and torsion testing of the SLA printed specimens was conducted using a dynamical testing machine (Electropulse™ E10000, Instron Systems, Norwood, USA) (**Figure 4.2C**). The compression tests were performed at a rate of 1.3 mm/min, following the ASTM D695-15 standard [5], with a maximum loading of 8500 N. To study the full-field strain distributions, the local displacement fields of each test were captured using a Q-400 2 × 12 MPixel digital image correlation (DIC) system (LIMESS GmbH, Krefeld, Germany) at a frequency of 1 Hz. Before testing, a black dot speckle pattern was applied over a white paint background on each specimen. The strains of the tested specimens were determined using the commercial DIC program Instra 4D v4.6 (Danted Dynamics A/S, Skovunde, Denmark). The elastic modulus was calculated from the engineering stress-strain curve within the elastic region (0.3% - 2% strain) using MATLAB R2020b, and the average value was obtained for each set of three specimens. The yield strength (σ_y) was calculated at 0.2% strain. The true stress and strain were calculated from the engineering stress and strain using **Eq. 4.1** and **Eq. 4.2** [2]:

$$\varepsilon = \ln(1 + \varepsilon_{eng}) \quad (\text{Eq. 4.1})$$

$$\sigma = \sigma_{eng}(1 + \varepsilon_{eng}) \quad (\text{Eq. 4.2})$$

where ε is the true strain and σ is the true stress. The true plastic strain of the material was calculated using **Eq. 4.3**:

$$\varepsilon_{pl} = \varepsilon_t - \varepsilon_{el} = \varepsilon_t - \sigma/E \quad (\text{Eq. 4.3})$$

where ε_{pl} is the true plastic strain, ε_t is the true total strain, ε_{el} is the true elastic strain, and E is the Young's modulus.

For torsion testing, special steel holders were required, which were designed in SolidWorks and manufactured using a 5-axis computer numerical control (CNC) machine (MillTap 700, DMG MORI, Veenendaal, NL) (**Figure 4.2D**).

The torsion specimens were rotated at a rate of 0.001 s⁻¹ according to ASTM E143-20. The rotational speed was adjusted to the specimen size (**Table 4.2**) using **Eq. 4.4** [6]:

$$\gamma = \theta r / L \quad (\text{Eq. 4.4})$$

where γ is the torsional shear strain, θ is the angle of rotation, r is the radius of the specimen, and L is the total length of the specimen.

The torque (T) and rotation angle (θ) were recorded until failure or until reaching the torque limit (95 Nm) or rotation angle limit (270°). The DIC system was utilized to calculate the torsional shear strain for improved measurement accuracy. The torsional shear stress was determined from the recorded torque using **Eq. 4.5** [6]:

$$\tau = Tr / J \quad (\text{Eq. 4.5})$$

where τ is the shear stress and J is the second polar moment of area. The polar moment of the area was calculated for the smallest cross-sectional area (*i.e.*, the cylindrical tip of the R implant) according to **Eq. 4.6** [6]:

$$J = \pi D^4 / 32 \quad (\text{Eq. 4.6})$$

where D is the diameter of the cylindrical tip of the torsion specimens (**Table 4.1**).

The strain was calculated by utilizing the DIC displacement values for two points on the cylindrical part of the specimens, near the base and the top. The recorded displacements were converted to rotational displacements using coordinate system conversion for cylindrical coordinates. The shear strain was then calculated using **Eq. 4.4** and the shear modulus was calculated according to **Eq. 4.7**:

$$E = 2G(1 + \nu) \quad (\text{Eq. 4.7})$$

4.2.5. FRACTOGRAPHY

To investigate the failure mode of the specimens after the torsion test, high-resolution SEM images of 8R specimens were captured from the fracture surface using a Helios microscope (FEI Helios G4 CX dual-beam workstation, Hillsborough, OR, USA) operating at 10 kV and 25 pA. Before SEM imaging, the specimens were coated with a thin layer of gold (thickness \approx 5 nm) using a sputter coater (JFC-1300, JEOL, Japan). Optical images were also taken from the section closest to the cuboidal end of the torsion specimens following the test, and whenever possible, the fracture angles were determined.

4.2.6. RAMAN SPECTROSCOPY

The chemistry of uncured and cured IP-Q and Grey resin was analyzed using an inVia Reflex Raman system (Renishaw plc, Wotton-under-Edge, UK). Raman spectra were acquired using a 50 \times objective lens, operated at an excitation wavelength of 532 nm. The laser intensity was set to 50%. Each spectrum was obtained by averaging 15 acquisitions with an exposure time of 1.0 sec. Subsequently, a baseline correction was applied to eliminate instrument noise using OriginPro 9.8.0.200 (OriginLab Corporation, Northampton, USA).

4.2.7. STATISTICAL ANALYSIS

To investigate whether the Young's modulus and yield strength of the Grey resin micropillars differed significantly with regards to the layer thickness and printing orientation a one-way ANOVA test was conducted ($p \leq 0.05$).

4.3. RESULTS

4.3.1. COMPRESSION OF THE IP-Q (2PP) AND GREY RESIN (SLA) PILLARS

Micropillar compression tests revealed a Young's modulus of 2.78 GPa and a yield strength of 60.4 MPa for the IP-Q printed pillars. Compression testing was employed to calculate the Young's modulus and yield strength of the pillars printed with two different layer thicknesses and in two different printing directions. The vertically printed pillars with a layer thickness of 25 μm exhibited a Young's modulus of 2.51 ± 0.13 GPa and a yield strength of 59.2 ± 0.91 MPa, while those with a layer thickness of 50 μm had a Young's modulus of 2.50 ± 0.10 GPa and a yield strength of 56.4 ± 1.7 MPa. The horizontally printed pillars displayed a Young's modulus and yield strength of 2.51 ± 0.05 GPa and 72.4 ± 3.4 MPa for the 25 μm pillars, and 2.33 ± 0.20 GPa and 79.4 ± 2.8 MPa for the 50 μm pillars. The stress-strain curves measured for the pillars with different layer thicknesses and printing orientations demonstrated that there were no statistically significant differences in the Young's modulus values, but there were statistically significant differences in the yield strength values (**Section 4.6** and **Figure S4.4**). However, the general mechanical behavior of the pillars remained the same regardless of the layer thickness or printing direction (**Figures 4.3A, B**). Moreover, the pillars did not exhibit any buckling during the compression tests (DIC

details in **Figures 4.3A, B**). The Young's modulus and yield strength of IP-Q and Grey resin pillars were similar (**Figure 4.3C**).

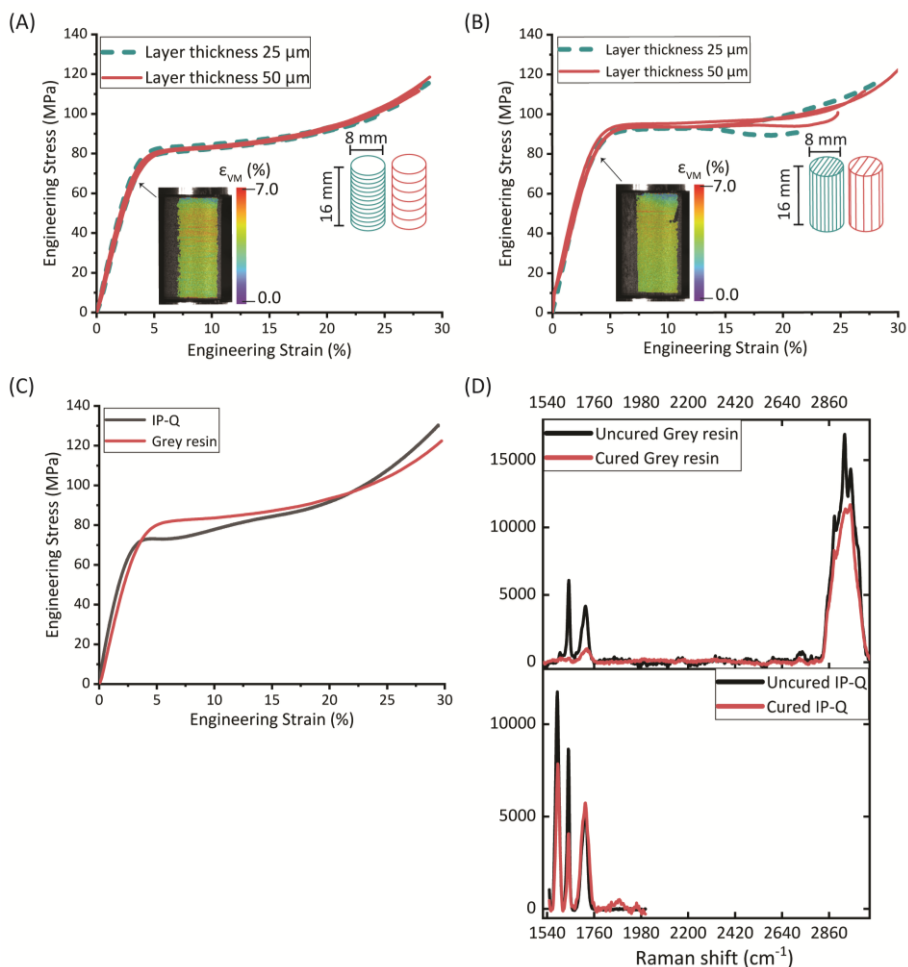
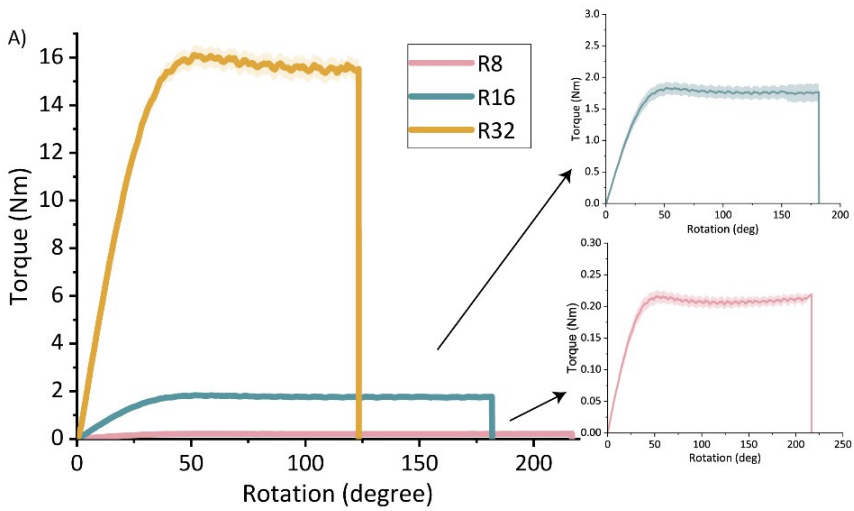


Figure 4.3. The compression stress-strain curves of **(A)** Grey resin pillars (\varnothing 8 mm \times 16 mm) with horizontally printed layers with a thickness of 25 μm or 50 μm (inset: DIC image of a compressed pillar at yield). **(B)** Grey resin pillars (\varnothing 8 mm \times 16 mm) with vertically printed layers with a thickness of 25 μm or 50 μm (inset: DIC image of a compressed pillar at yield). **(C)** The compression stress-strain curves for pillars printed from Grey resin and IP-Q. **(D)** The Raman spectra of polymerized (red) and unpolymerized (black) Grey resin and IP-Q specimens.

4.3.2. TORSION TESTING

4.3.2.1. EXPERIMENTAL TORSION TESTING ON SOLID GREY RESIN TORSION SPECIMENS

The largest torsion specimen (32R) failed at the lowest angle of rotation ($123.2^\circ \pm 9.0^\circ$) and the highest applied torque (15.43 ± 0.39 Nm), while the smallest torsion specimens (8R) failed at the highest angle of rotation ($216.9^\circ \pm 5.4^\circ$) and the lowest applied torque (0.21 ± 0.01 Nm) (**Figure 4.4A**). The 16R torsion specimens failed at a rotation of $181.7^\circ \pm 27.0^\circ$ and a torque of 1.78 ± 0.08 Nm (**Figure 4.4A**). All the specimen types experienced failure in the cylindrical shaft close to the junction with the cuboid (**Figure 4.4B** and **Figure S4.2**). Among the 8R specimens, one exhibited a fracture angle of $\approx 44^\circ$, while the other two had a fracture angle of $\approx 0^\circ$ (**Figure 4.4B**). The hackles on the inclined fracture surface appeared to radiate from a single point of origin, whereas the flat angle surface showed visible hackles without a single point of origin. The inclined-angle surface displayed elongated markings and relatively larger smooth sections within the roughness of the surface, in contrast to the flat-angle surface which exhibited more uniformly sized round markings (**Figure 4.4C-F**).



4

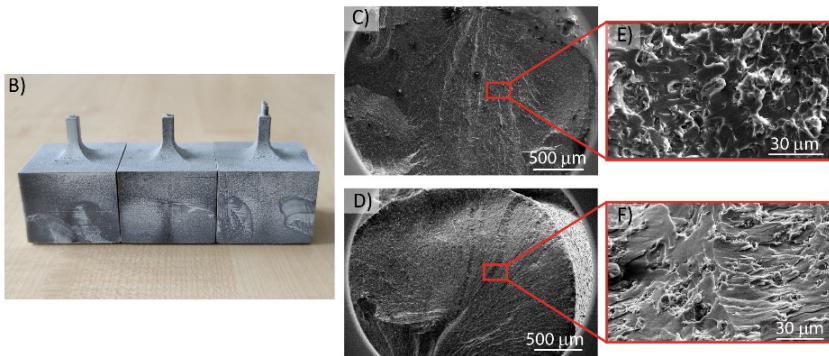


Figure 4.4. (A) The torque vs rotation curves of the torsion specimens 8R, 16R, and 32R printed from Grey resin. (B) The optical image of the fracture angles of the 8R torsion specimens. (C, E) SEM images of the 8R flat fracture surfaces. (D, F) SEM images of the 8R inclined fracture surface.

4.3.2.2. EXPERIMENTAL AND FEA SIMULATION OF THE SOLID AND POROUS GREY RESIN TORSION SPECIMENS

Torque vs. rotation

FEA simulation and experimental torsion testing on specimens 8R, 16R, and 32R confirmed that torque increased with the specimen size. The torque for the 16R specimens was approximately 8.5 times greater than that of the 8R torsion specimens and approximately 8.7 times lower than that of the 32R specimens. At 15° rotation, the measured torque values for the 8R, 16R, and 32R specimens were $85.6 \pm 5.0\%$, $84.6 \pm 5.1\%$, and $89.2 \pm 2.8\%$ of the torque value resulting from their corresponding FEA

models, respectively. The difference between the measured and FEA-predicted values of torque increased with the rotation. For example, at 50° rotation, the torque measured for the 8R, 16R, and 32R torsion specimens were $77.1 \pm 2.6\%$, $78.5 \pm 3.5\%$, and $83.6 \pm 2.2\%$ of their corresponding FEA-predicted values, respectively. The FEA-predicted torque values of the torsion specimens were lower than the FEA-predicted torque values of the enlarged implants without grippers and were more similar to the experimental data. FEA simulations for all the sizes of the R design indicated that higher torques were needed to achieve the same rotation as in the torsion specimens (**Figure 4.5A-C**). However, as the size of the specimens increased, the difference between the FEA-predicted torque values of the torsion specimens and that of the R implants decreased, with the grippers playing a minor role in the final response of the specimens under torsion. A comparison between the torque-rotation values of the porous 32R60 specimens and the FEA simulations revealed that the specimens failed at the rotation angle of $38 \pm 10^\circ$, which was approximately 3.2 times lower than the rotation angle corresponding to the failure point of the 32R specimens (**Figure 4.5C, D**). Within the linear part of the curve, the results of the FEA simulations and the experiments were in good agreement. For instance, at 15° rotation, the measured torque value for the porous 32R specimens was $98.9 \pm 2.8\%$ of the corresponding FEA values (**Figure 4.5D**).

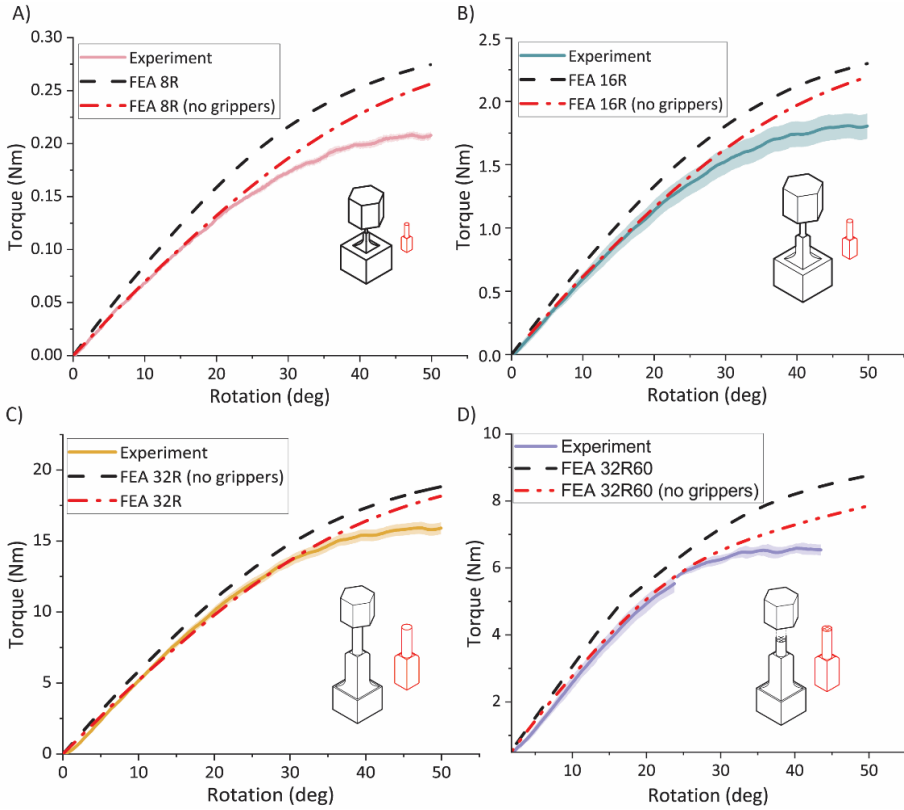
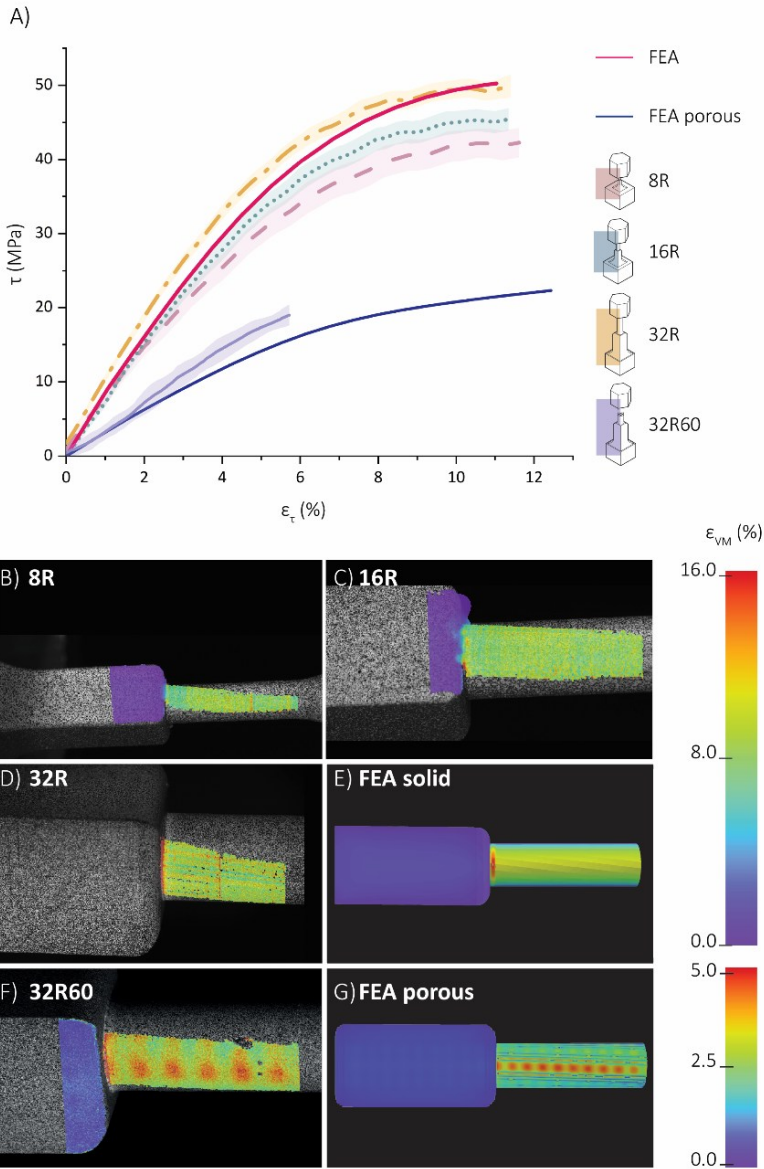


Figure 4.5. Torque vs rotation graph for all the torsion specimens. The experimental and FEA data for the (A) 8R, (B) 16R, (C) 32R, and (D) 32R60 torsion specimens with and without the grippers.

Shear stress vs. shear strain

Comparing the shear stress-strain values between the FEA torsion specimens and experimental data for the 8R, 16R, and 32R specimens prior to the 0.2% yield (50° rotation) revealed that the shear stresses of the 8R and 16R specimens were lower than those predicted by the FEA models (**Figure 4.6A**). However, the shear stress values of the 32R specimens were higher than those obtained from the FEA simulations. Calculation of the shear modulus using the linear part of the shear stress- shear strain graph resulted in shear modulus values of 670.0 ± 34.0 MPa, 772.2 ± 30.6 MPa, and 867.1 ± 36.7 MPa, for the 8R, 16R, and 32R specimens, respectively. Based on **Eq. 4.7**, the theoretical value for the shear modulus is 896.1 MPa. The strain distribution analysis using DIC for the 8R and 16R specimens revealed very low stress values near the junction (**Figure 4.6B, C**). However, the 32R specimens displayed the highest

stress values at the junction between the cylindrical shaft and the cube (**Figure 4.6D**). The FEA strain distribution also showed similar values and behavior (**Figure 4.6E**). A comparison between the strain distributions measured by DIC for the 32R60 specimens and the corresponding FEA results revealed that the highest strain values were observed at the junction, as well as on the checkered patterns present on the cylinder, corresponding to the pores of the inner lattice structure (**Figure 4.6F, G**).



4

Figure 4.6. Shear stress-shear strain curves and full-field strain measurement using digital image correlation (DIC). (A) Shear stress vs shear strain for the SLA-printed torsion specimens printed from Grey-resin and the corresponding FEA data (red). The experimental data is averaged and is presented as mean \pm standard deviation (shadowed lines). The DIC-measured distribution of the effective strain (von Mises) for the (B) 8R, (C) 16R, (D) 32R, and (E) FEA model of the scaled-up R torsion specimen. Color map strain: 0%-16%. (F) The FEA-predicted values of the effective strain (von Mises) for the porous 32R60 scaled-up torsion specimen. (G) The distribution of the FEA-predicted values of the effective strain (von Mises) for the porous torsion specimen. Color map strain: 0%-5%.

FEA simulation of IP-Q implants

A comparison between the FEA-predicted torque-rotation curves of the R, R20, R60, and RH IP-Q implants showed that much higher torque is required for the R specimens to achieve the same rotation angle, while there was a smaller difference between the torque values required for achieving the same rotation angle between the R60 and R20 implants. The shear stress and shear strain distribution measured for the R, R20, and R60 specimens at a rotation of 15° indicated the stress and strain values experienced by the cuboid part are close to zero, and the entire stress and strain distribution was limited to the cylindrical part (**Figure 4.7B**). In the case of the R specimens, the maximum shear stress and strain occurred at the junction. However, these observations were not valid for either of the porous designs, namely R60 and R20. For R60, a discernible checkered pattern was observed within the cylindrical region, representing the presence of pores within the structure (**Figure 4.7B**). Additionally, two distinct lines were identified along the longitudinal axis of the cylinder, aligning with the regions of elevated shear strain and shear stress. However, the checkered patterns were not visible on the R20 design. Nonetheless, a broad line was discerned along the longitudinal axis of the cylinder, corresponding to the regions of maximum shear stress and strain within the structure. A comparison between the FEA-predicted torque-rotation curves of the C, C20, C60, and CH IP-Q implants showed that much higher torque is required for the C specimens to achieve the same rotation angle, while there was no significant difference between the torque values required for the C20 and C60 implants (**Figure 4.7A**). More specifically, the torque needed to rotate the C60 specimens by 15° was 97% of the torque needed to rotate the C20 specimens (**Figure 4.7A**). The distribution of the shear strain was similar for all the designs (**Figure 4.7C**). The C specimens had the highest maximum strain of the three designs, while C20 had the lowest maximum strain (**Figure 4.7C**). The shear strain was concentrated at the tip of the specimens, where the diameter of the design was the smallest (**Figure 4.7C**). A comparison between the results of the torsion tests on the two different designs revealed that, within each porous group, the C design exhibited greater stability and required higher torque to achieve the same amount of rotation as compared to the R design (**Figure 4.7A**). For instance, at a rotation angle of 15°, the torques required to rotate the C, C60, and C20 specimens

were respectively 1.6, 3.1, and 2.7 times higher than the torques required to rotate the R, R60, and R20 specimens (**Figure 4.7A**).

4.3.3. RAMAN SPECTROSCOPY

The Raman spectra of the uncured and cured IP-Q exhibited characteristic peaks at 1590 cm^{-1} , 1635 cm^{-1} , and 1715 cm^{-1} , associated with aromatic ring vibrations, double bond (C=C) stretching vibrations, and carbonyl (C=O) stretching vibrations, respectively. The peak intensity of the carbonyl (C=O) vibration did decrease upon curing. However, the peak intensity of the double bond (C=C) at 1635 cm^{-1} and the aromatic ring vibration at 1590 cm^{-1} decreased in the cured specimens. In the case of the uncured and cured Grey resin specimens, a prominent peak at 2952 cm^{-1} corresponding to C-H stretching vibration was observed. Additionally, the uncured Grey resin exhibited peaks at 1715 cm^{-1} (carbonyl C=O stretching vibration) and 1640 cm^{-1} (presence of monomers).

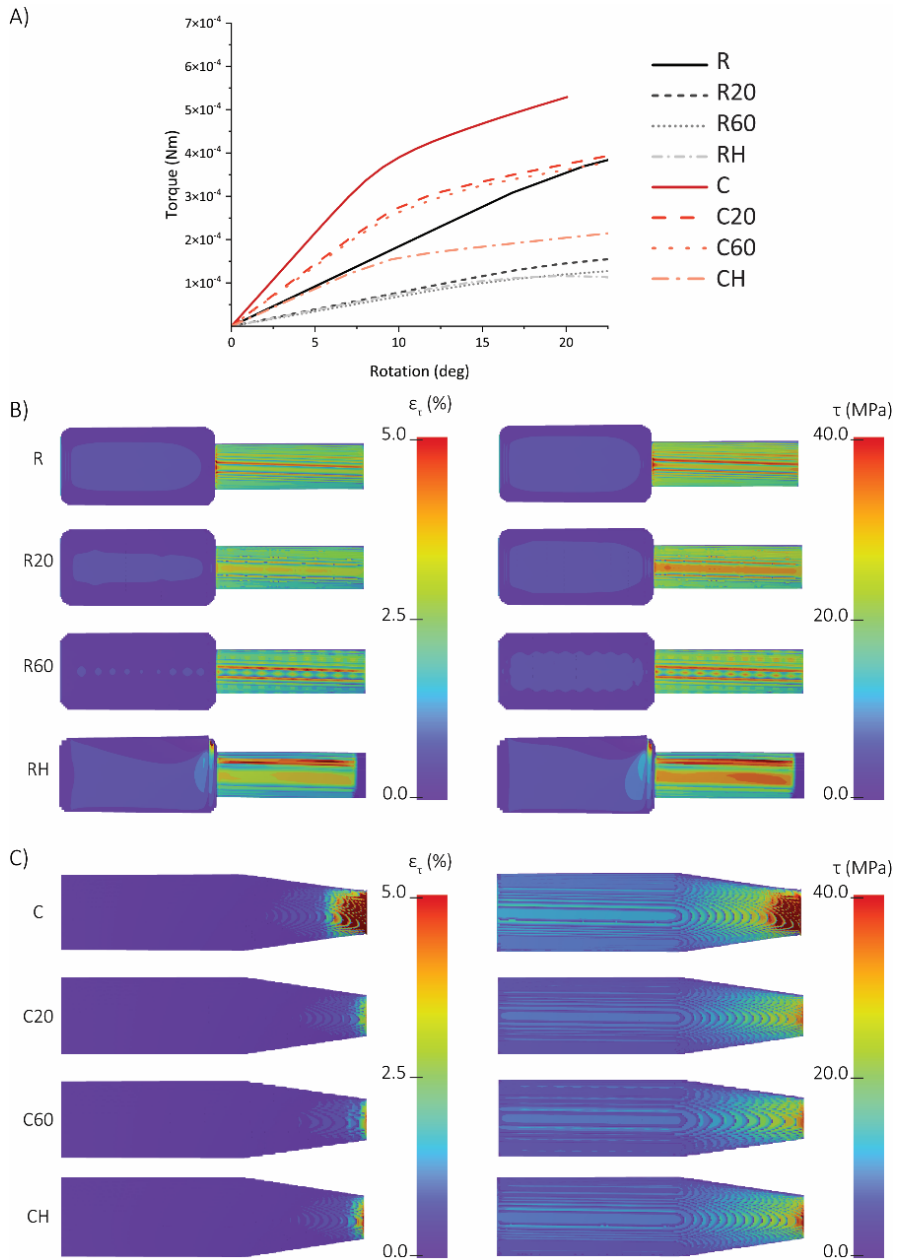


Figure 4.7. (A) The FEA-predicted torque vs rotation for the solid, porous, and hollow types of cochlear implants made from IP-Q (*i.e.*, R, R20, R60, RH, C, C20, C60, and CH). (B) The FEA-predicted values of the shear stress (on the left) and shear strain (on the right) corresponding to a rotation of 15° for the R, R20, R60, and RH specimens. (C) The FEA-predicted values of the shear stress (on the left) and shear strain (on the right) corresponding to a rotation of 15° for the C, C20, C60, and CH specimens.

4.4. DISCUSSION

The aim of the current study was the mechanical characterization of newly developed 3D-printed cochlear implants intended for local drug delivery, considering their implantation method and their suitability as permanent implants that can affect their efficiency as a drug delivery system. Due to the unique size and complex shape of these implants, mechanical testing on such implants with standard testing equipment was challenging and had received limited attention. Consequently, the development of a novel approach was necessary, incorporating multi-scale *in silico* and *ex silico* methods to achieve a comprehensive mechanical characterization of cochlear implants. To address size and shape limitations, enlarged models of cochlear implants were simulated for torsion using FEA models, which were further validated through torsion tests. By extrapolating the validated *in silico* model to real-size implants, the study enabled the mechanical characterization of various cochlear implant designs, facilitating the selection of the most suitable one for cochlear implantation. Moreover, the development of this new method provided an opportunity to investigate some additional parameters related to the 3D printing techniques employed and the materials utilized.

4.4.1. EFFECT OF LAYER THICKNESS AND PRINT ORIENTATION ON THE YOUNG'S MODULUS OF GREY RESIN

Compression testing was performed on the pillars printed with Grey resin using different printer settings. Two different layer thicknesses (25 and 50 μm) and two different print orientations (horizontal and lateral layers) were used. The Young's modulus was determined for each of these four conditions. In the case of the horizontally printed pillars, the Young's modulus of the pillars printed with a 25 μm layer thickness was 2.51 ± 0.13 GPa, while for the 50 μm layer thickness, it was 2.50 ± 0.10 GPa. The laterally printed pillars had a Young's modulus of 2.51 ± 0.050 GPa for the pillars printed with a 25 μm layer thickness and 2.33 ± 0.20 GPa for the 50 μm layer thickness pillars. The lack of difference in the Young's modulus between the pillars with different layer thicknesses was unexpected, as previous research on specimens with different layer thicknesses has observed differences in the tensile strength and the Young's modulus [9,34]. The literature is divided on whether different print

orientations should affect the Young's modulus of the material. Some studies have found that SLA printed parts are broadly isotropic materials, and print orientation does not significantly affect the Young's modulus [3,9,10,11], which is in agreement with our findings. However, other studies have reported a dependence of the mechanical properties on the printing direction [12,29,34]. It is worth noting that most of these tests are performed using tensile testing, making it difficult to directly compare them with the compression tests we conducted here. Therefore, a more comprehensive study investigating the anisotropy of SLA materials, possibly employing different mechanical tests, is necessary to draw definitive conclusions.

4.4.2. FAILURE MODE ANALYSIS OF GREY RESIN

One of the crucial aspects of a material's mechanical behavior is its failure mode, which can generally be categorized as either ductile or brittle [18]. In this study, experimental torsion testing was conducted on Grey resin torsion specimens until failure to determine the material's failure mode. Several factors were considered, including the shape of torque versus rotation curves, the failure angles of the torsion specimens, and the SEM images of the fracture surface. Analysis of the experimental torque versus rotation curves for all three scales of the specimens revealed that the material yielded after approximately 50° of rotation, with the torque reaching a plateau as rotation increased. This behavior indicates a ductile material, as it exhibits a large area under the stress-strain curve due to continued deformation after the yield point [18]. Next, the failure angles of the specimens were examined. In ductile materials, torsion failure typically occurs along the plane of maximum shear stress since they are weaker in shear, which is perpendicular to the structure's axis. In contrast, brittle materials are weaker in tension, and torsion failure tends to occur along the plane of maximum tension, resulting in a 45° angle [16, 28]. Out of the ten analyzed failure angles, three (two 8R and one 16R torsion specimens) exhibited a failure angle perpendicular to the axis of the structure, indicating shear failure. The remaining six measured specimens (including all 32R types) had failure angles ranging between 31° and 44°, suggesting that these specimens were weaker in tension than in shear (**Table S4.1**). This implies that most of the torsion specimens experienced a brittle failure mode and that the different failure rotational angles

across the samples are related to the different specimen sizes. Furthermore, SEM images were captured of the fracture surfaces of two 8R torsion specimens: one with a flat failure angle and one with an inclined failure angle. Both specimens displayed a rough surface with visible micropatterning and fibrillations, although the specimen with the flat angle exhibited overall smaller micropatterning compared to the inclined-angle specimen. A study examining the fracture surfaces of tensile test specimens made using SLA from an acrylate polymer MD-R001CR (ApplyLabWork, Torrance, USA) concluded that specimens with a highly ductile stress-strain curve exhibited a smooth fracture surface, while specimens with a more brittle stress-strain curve had rougher fractures [27]. This observation does not hold for our torsion specimens made out of Grey resin, as they demonstrate a ductile stress-strain curve but exhibit a rough fracture surface. An exact comparison between the results of the previous study and our study can, therefore, not be made since the type of the material seems to influence the mechanical and fractural behavior more than the manufacturing technique. In summary, the various aspects of the failure mode analysis cannot predominantly conclude a brittle or ductile failure in the Grey resin material. Conducting additional torsion testing to examine the post-yield plastic behavior of the material would help clarify this inconsistency. Understanding the failure mode of Grey resin is essential for evaluating its potential applications.

4

4.4.3. COMPARATIVE ANALYSIS OF EXPERIMENTAL AND FEA TORSION TESTING RESULTS

For both solid and porous specimens, the experimental torsion tests conducted on the torsion specimens made from Grey resin were compared with the torsion tests simulated using FEA. When comparing the FEA-predicted and experimental torque-rotation curves for the solid specimens, good agreement was observed for the elastic-linear part of the curve until yielding. The porous 32R60 specimen also showed good agreement between the experimental and FEA curves, although the porous specimens failed earlier than their solid counterparts, which was not captured by the FEA models. However, significant differences were observed in the post-yield behavior between the FEA simulations and experimental results for the solid R specimens. The stress-strain curve obtained from compression testing showed strain hardening,

which was not observed during torsion testing. Therefore, using compression stress-strain curves as input data for FEA may not be accurate for simulating the post-yield behavior observed in the torsion tests. Comparing the solid upscaled R and solid torsion specimens through FEA, we found that the R exhibits higher torques for all the three sizes, indicating that the inclusion of the additional grippers lowers the torque-rotation curve which is translated into a decrease in the total needed energy to failure. The difference between the experimental and simulation data increased with the degree of rotation, with a smaller difference observed for the 32R torsion specimens as compared to the 8R and 16R torsion specimens. This apparent dependence on the size might be due to the relatively greater added length of the structures in the 8R torsion specimens as compared to the 32R torsion specimens. The shear stress-strain curves were approximated by considering only the cylindrical part of the specimen, as it experiences most of the generated stress and strain due to its smaller diameter as compared to the cubic part. Good agreement between the experimental and FEA-predicted curves was observed in the linear elastic region. Similar to the torque-rotation curves, a trend was observed where the 8R and 16R torsion specimens deviated more from the FEA shear stress-strain curve compared to 32R torsion specimens. The experimentally measured and FEA-predicted strain distribution in both solid and porous torsion specimens presented similar patterns. For the porous 32R torsion specimens, both showed a checkered pattern with higher strain areas corresponding to the inner unit of the lattice structure. The experimental DIC distribution exhibits a similar pattern as the FEA strain distribution, with higher strain areas occurring between the struts of the inner lattice structure. The strain distribution of the Grey resin specimens revealed that the higher strain areas observed in the porous specimens corresponded to the inner unit of the lattice structure, which had a pore size of approximately $1.9 \times 1.9 \times 1.9 \text{ mm}^3$. In the FEA simulations, the higher strain areas within the cylindrical part were located between the struts of the inner lattice structure. Comparing the experimental data obtained for the Grey resin with the FEA models, good agreement was found in the linear-elastic region for both torque-rotation and stress-strain curves, as well as strain distributions. This indicates that Grey resin can be accurately modeled with FEA using compression data as input in the linear-elastic region.

4.4.4. ANALYSIS OF FEA MODELING: GREY RESIN VS. IP-Q

SLA and 2PP are additive manufacturing techniques based on the principle of polymerization. While SLA involves the absorption of a single photon, 2PP requires the absorption of two photons [25, 33]. Due to the similarities in the manufacturing process and mechanical properties of Grey resin (printed with SLA) and IP-Q (printed with 2PP), it is expected that the mechanical behavior of the printed structures would exhibit similar characteristics. The measured Young's moduli of Grey resin and IP-Q were similar (2.50 GPa and 2.78 GPa, respectively). Validation of the FEA model using torsion testing on IP-Q structures was not possible due to the limited size that can be achieved with 2PP printing. However, with Grey resin, sufficiently large specimens were printed using SLA to conduct torsion testing, allowing for experimental validation of the FEA model. The linear regions of both experimental and FEA-predicted data demonstrated good agreement (**Figure 4.6**), enabling the extrapolation of the FEA simulations to predict the linear behavior of the ear implants made from IP-Q. In the FEA simulations, the input data for IP-Q, including the Young's modulus and stress-strain curve, were obtained from compression testing of a solid cylindrical structure made from IP-Q, similar to the process for Grey resin. However, the IP-Q input data was derived from a single compression experiment, unlike Grey resin data which was derived from three compression experiments on distinct pillars. Consequently, the reliability of the IP-Q input data is comparatively lower, but the measured values are in line with the values reported in the literature [30]. Despite their distinct Young's moduli and yield points, the shear stress-shear strain curves predicted by the FEA models for both materials presented similar overall trends. This similarity suggests that the torsional behavior of IP-Q can be accurately simulated using FEA techniques similar to those applied for Grey resin. Utilizing FEA modeling to characterize IP-Q could reduce the reliance on specialized equipment and facilitate the mechanical testing of more complex designs.

4.4.5. FEA OF MECHANICAL BEHAVIOR: R VS. C IMPLANT DESIGNS

In the case of IP-Q, both the R and C cochlear implant designs were simulated using FEA models, considering both porous and non-porous variations. Introducing porosity to the designs resulted in a decreased stiffness and mechanical strength for

each implant. Although the difference in the stiffness and mechanical strength between the identical designs with different pore sizes (*i.e.*, 60 μm and 20 μm) was not substantial, the difference in stiffness and mechanical strength between the different types of implants (*i.e.*, R and C) was notable. At a rotation angle of 15°, the C design exhibited a mere 3% reduction in stiffness and mechanical strength, whereas the R design experienced a more pronounced decrease of 13% (**Figure 4.7**) when compared to their solid versions, respectively. This implies that the porous structure had a greater impact on the mechanical properties of the R as compared to the C. The shear stress-strain distribution of the porous R displayed a distinct pattern for both the 20 and 60-pore size variants, which was absent in the solid R. This pattern suggests the presence of stress concentrations arising from the inner lattice structure of the square unit, particularly near the connections between the struts where sharp transitions occur [1]. Conversely, the porous C did not exhibit such patterns. The shear stress-strain distributions of both solid and porous C implants presented similarities. Notably, the C design exhibited higher stiffness and mechanical strength as compared to R. This verifies our attempt to enhance the mechanical integrity of the R implant at the junction between the drug container and the tip by introducing a tapering angle, which led to the creation of the C-type implant. From a mechanical standpoint, the C implant design is more favorable while preserving the general dimensions found in the existing literature and adhering to the preferences of medical specialists in the field [14].

4.4.6. POLYMERIZATION OF IP-Q AND GREY RESIN DURING 2PP AND SLA PRINTING

Existing studies have established a correlation between the polymerization that occurs during 3D printing and its influence on the mechanical properties of the resulting structures [22,31]. Raman spectroscopy allows for the analysis of distinct peaks associated with different intramolecular bonds, providing insights into the molecular structure changes during polymerization. Therefore, the polymerization process during 2PP printing and SLA printing was investigated by conducting Raman spectroscopy on unpolymerized and polymerized IP-Q and Grey resin. The C=C bond, typically present at 1640 cm^{-1} , showed lower intensity in the polymerized IP-Q and

Grey resin specimens as compared to the unpolymerized specimens. This decrease in the C=C bond peak is expected for photocurable resins undergoing polymerization [20, 26]. Furthermore, the unpolymerized IP-Q resin exhibited a peak at 1590 cm^{-1} , which is associated with the aromatic ring present in IP-Q. This peak is specific to IP-Q and is not observed (at the same intensity) in most other photoresins [8,13,24,26,30]. The decrease in the intensity of the aromatic ring peak after polymerization suggests its potential involvement in the polymerization process of IP-Q, a resin specifically designed for high-speed fabrication. Since the aromatic ring also contains C=C bonds, its contribution may influence the intensity of the C=C bond peak, consequently impacting the calculation of the degree of conversion (DC). Albeit, no parametric study of the 2PP printing parameters that influence polymerization, hence the mechanical properties of IP-Q was performed, IP-Q was chemically characterized for the printing conditions suitable for the fabrication of the cochlear implants. Further investigations on IP-Q resin can provide additional insights into the specific mechanisms of polymerization during the printing of this innovative resin. For the Grey resin, there is a peak at 1715 cm^{-1} that decreases significantly after printing, associating it with the polymerization process. The findings indicated a high DC and a high degree of printing accuracy and are in line with a previous study on commercially available methacrylate-based resins used in SLA printing [7].

4.5. CONCLUSION

In conclusion, in this study, we developed a methodology to characterize the mechanical behavior of cochlear implants of relevant sizes for humans. We used FEA models to validate the results of the experiments. The use of 2PP with the novel resin IP-Q for printing the ear implants along with the scaled-up SLA-printed cochlear implants made from Grey resin enabled us to study their mechanical properties. The FEA simulations accurately captured the linear behavior of the ear implants until the yield point, while only utilizing compression data. This validation enabled us to use these FEA models to study the torsion testing of the real-size implants made from IP-Q using only compression data. Comparing both ear implant designs, the C type exhibited higher stiffness and mechanical strength than the R type. Although the size of the pores (*i.e.*, $20\text{ }\mu\text{m}$ and $60\text{ }\mu\text{m}$) did not have a significant effect on the mechanical

performance of the implant, they could have a major impact on other factors, such as drug storage and diffusion in the final design. From a mechanical perspective, the C design emerges as the preferred option. Characterizing the mechanical properties of these distinct inner ear implant designs using the IP-Q resin represents a novel contribution. Additionally, this study marks the first time such ear implants have been mechanically characterized using this approach. The obtained data will contribute to the assessment of the implants' ability to withstand mechanical stress during implantation, helping to determine whether such types of ear implants are suitable for the potential treatment of inner ear disorders. Future research directions may involve finding alternative methods to model post-yield behavior and exploring various geometries of the inner structures. Overall, this study provides valuable insights into the mechanical behavior of cochlear implants and lays the groundwork for further advancements in this field.

REFERENCES

- [1] Al-Ketan, O., Rezgui, R., Rowshan, R., Du, H., Fang, N. X., and Abu Al-Rub, R. K. (2018). Microarchitected stretching-dominated mechanical metamaterials with minimal surface topologies. *Adv. Eng. Mater* 20 (9), 1800029. <https://doi.org/10.1002/adem.201800029>.
- [2] Arasaratnam, P., Sivakumaran, K. S., and Tait, M. J. (2011). True stress-true strain models for structural steel elements. *ISRN Civ. Eng.* 2011, 1-11. <https://doi.org/10.5402/2011/656401>.
- [3] Aravind Shanmugasundaram, S., Razmi, J., Mian, M. J., and Ladani, L. (2020). Mechanical anisotropy and surface roughness in additively manufactured parts fabricated by stereolithography (SLA) using statistical analysis. *Materials* 13 (11), 2496. <https://doi.org/10.3390/ma13112496>.
- [4] Ast, J., Mohanty, G., Guo, Y., Michler, J., and Maeder, X. (2017). *In situ* micromechanical testing of tungsten micro-cantilevers using HR-EBSD for the assessment of deformation evolution. *Mater Des.* 117, 265-266. <https://doi.org/10.1016/j.matdes.2016.12.052>.
- [5] ASTM International (2019). D695 – 15 standard test method for compressive properties of rigid plastics 1. [10.1520/D0695-15](https://doi.org/10.1520/D0695-15).
- [6] ASTM International (2020). E143 – 20 standard test method for shear modulus at room temperature. [10.1520/E0143-20](https://doi.org/10.1520/E0143-20).
- [7] Băilă, D. I., and Tonoiu, S. (2022). Properties of photo-curable polyurethane resins used in SLA manufacturing. *IOP Conf. Ser. Mater Sci. Eng.* 1268 (1), 012006. [doi:10.1088/1757-899X/1268/1/012006](https://doi.org/10.1088/1757-899X/1268/1/012006).
- [8] Bauer, J., Guell Izard, A., Zhang, Y., Baldacchini, T., and Valdevit, L. (2019). Programmable mechanical properties of two-photon polymerized materials: from nanowires to bulk. *Adv. Mater Technol.* 4 (9), 1900146. <https://doi.org/10.1002/admt.201900146>.
- [9] Chockalingam, K., Jawahar, N., Chandrasekar, U., and Ramanathan, K. N. (2008). Establishment of process model for part strength in stereolithography. *J. Mater Process Technol.* 208 (1-3), 348-365. <https://doi.org/10.1016/j.jmatprotec.2007.12.144>.
- [10] Cosmi, F., and Dal Maso, A. (2020). A mechanical characterization of SLA 3D-printed specimens for low-budget applications. *Mater Today Proc.* 32, 194-201. <https://doi.org/10.1016/j.matpr.2020.04.602>.
- [11] Dizon, J. R. C., Espera, A. H., Chen, Q., and Advincula, R. C. (2018). Mechanical characterization of 3D-printed polymers. *Addit. Manuf.* 20, 44-67. <https://doi.org/10.1016/j.addma.2017.12.002>.
- [12] Dulieu-Barton, J. M., and Fulton, M. C. (2000). Mechanical properties of a typical stereolithography resin. *Strain* 36 (2), 81-87. <https://doi.org/10.1111/j.1475-1305.2000.tb01177.x>.

- [13] Fu, Z., Jiang, L., Wardini, J. L., MacDonald, B. E., Wen, H., Xiong, W., et al. (2018). A high-entropy alloy with hierarchical nanoprecipitates and ultrahigh strength. *Sci. Adv.* 4 (10), eaat8712. <https://www.science.org/doi/10.1126/sciadv.aat8712>.
- [14] Gehrke, M., Sircoglou, J., Gnansia, D., Tourrel, G., Willart, J. F., Danede, F., et al. (2016). Ear Cubes for local controlled drug delivery to the inner ear. *Int. J. Pharm.* 509 (1-2), 85-94. <https://doi.org/10.1016/j.ijpharm.2016.04.003>.
- [15] Hague, R., Mansour, S., Saleh, N., and Harris, R. (2004). Materials analysis of stereolithography resins for use in Rapid Manufacturing. *J. Mater. Sci.* 39 (7), 2457-2464. <https://doi.org/10.1023/B:JMSC.0000020010.73768.4a>.
- [16] Hailu, Y. M., Nazir, A., Lin, S.-C., and Jeng, J.-Y. (2021). The effect of functional gradient material distribution and patterning on torsional properties of lattice structures manufactured using MultiJet fusion Technology. *Materials* 14 (21), 6521. <https://doi.org/10.3390/ma14216521>.
- [17] Hao, J., and Li, S. K. (2019). Inner ear drug delivery: recent advances, challenges, and perspective. *Eur. J. Pharm. Sci.* 126, 82-92. doi:10.1016/j.ejps.2018.05.020
- [18] Hayes, M. D., Edwards, D. B., and Shah, A. R. (2015). "Fractography basics," in *Fractography in failure analysis of polymers* (Elsevier), 48-92. <https://doi.org/10.1016/B978-0-323-24272-1.00004-0>.
- [19] Isaakidou, A., Apachitei, I., Fratila-Apachitei, L. E., and Zadpoor, A. A. (2023). High-precision 3D printing of microporous cochlear implants for personalized local drug delivery. *J. Funct. Biomater.* 14 (10), 494. <https://doi.org/10.3390/jfb14100494>.
- [20] Jiang, L. J., Zhou, Y. S., Xiong, W., Gao, Y., Huang, X., Jiang, L., et al. (2014). Two-photon polymerization: investigation of chemical and mechanical properties of resins using Raman microspectroscopy. *Opt. Lett.* 39, 3034-3037. <https://doi.org/10.1364/OL.39.003034>.
- [21] Jun, T.-S., Sernicola, G., Dunne, F. P. E., and Britton, T. B. (2016). Local deformation mechanisms of two-phase Ti alloy. *Mater. Sci. Eng. A* 649, 39-47. <https://doi.org/10.1016/j.msea.2015.09.016>.
- [22] LaFratta, C., and Baldacchini, T. (2017). Two-photon polymerization metrology: characterization methods of mechanisms and microstructures. *Micromachines* (Basel) 8 (4), 101. <https://doi.org/10.3390/mi8040101>.
- [23] Lin, Z., Novelino, L. S., Wei, H., Alderete, N. A., Paulino, G. H., Espinosa, H. D., et al. (2020). Folding at the microscale: enabling multifunctional 3D origami-architected metamaterials. *Small* 16 (35), 2002229. <https://doi.org/10.1002/smll.202002229>.
- [24] Liu, Y., Campbell, J., Stein, O., Jiang, L., Hund, J., and Lu, Y. (2018). Deformation behavior of foam laser targets fabricated by two-photon polymerization. *Nanomaterials* 8 (7), 498. <https://doi.org/10.3390/nano8070498>.
- [25] Pagac, M., Hajnys, J., Ma, Q. P., Jancar, L., Jansa, J., Stefek, P., et al. (2021). A review of vat photopolymerization Technology: materials, applications, challenges,

- and future trends of 3D printing. *Polym. (Basel)* 13 (4), 598. <https://doi.org/10.3390/polym13040598>.
- [26] Pianelli, C., Devaux, J., Bebelman, S., and Leloup, G. (1999). The micro-Raman spectroscopy, a useful tool to determine the degree of conversion of light-activated composite resins. *J. Biomed. Mater. Res.* 48 (5), 675-681. <https://doi.org/10.1002>.
- [27] Quagliato, L., Yeon Kim, S., and Ryu, S. C. (2022). Quasi-ductile to brittle transitional behavior and material properties gradient for additively manufactured SLA acrylate. *Mater. Lett.* 329, 133121. <https://doi.org/10.1016/j.matlet.2022.133121>.
- [28] Sadaghian, H., Khalilzadehtabrizi, S., Farzam, M., and Dehghan, S. (2022). Behavior of 3D-printed polymers under monotonic torsion - a database of 15 different materials. *Addit. Manuf.* 60, 103251. <https://doi.org/10.1016/j.addma.2022.103251>.
- [29] Saini, J., Dowling, L., Kennedy, J., and Trimble, D. (2020). Investigations of the mechanical properties on different print orientations in SLA 3D printed resin. *Proc. Inst. Mech. Eng. C J. Mech. Eng. Sci.* 234 (11), 2279-2293. <https://doi.org/10.1177/0954406220904106>.
- [30] Saldívar, M. C., Doubrovski, E. L., Mirzaali, M. J., and Zadpoor, A. A. (2022). Nonlinear coarse-graining models for 3D printed multi-material biomimetic composites. *Addit. Manuf.* 58, 103062. <https://doi.org/10.1016/j.addma.2022.103062>
- [31] Schweiger, S., Schulze, T., Schlipf, S., Reinig, P., and Schenk, H. (2022). Characterization of two-photon-polymerization lithography structures via Raman spectroscopy and nanoindentation. *J. Opt. Microsystems* 2 (3), 33501. <https://doi.org/10.1117/1.JOM.2.3.033501>.
- [32] Szeto, B., Chiang, H., Valentini, C., Yu, M., Kysar, J. W., and Lalwani, A. K. (2020). Inner ear delivery: challenges and opportunities. *Laryngoscope Investig. Otolaryngol.* 5 (1), 122-131. <https://doi.org/10.1002/lio2.336>.
- [33] Waheed, S., Cabot, J. M., Macdonald, N. P., Lewis, T., Guijt, R. M., Paull, B., et al. (2016). 3D printed microfluidic devices: enablers and barriers. *Lab. Chip* 16 (11), 1993-2013. <https://doi.org/10.1039/C6LC00284F>.
- [34] Wang, S., Ma, Y., Deng, Z., Zhang, K., and Dai, S. (2020). Implementation of an elastoplastic constitutive model for 3D-printed materials fabricated by stereolithography. *Addit. Manuf.* 33, 101104. <https://doi.org/10.1016/j.addma.2020.101104>.
- [35] Zhang, Z., Li, X., Zhang, W., and Kohane, D. S. (2021). Drug delivery across barriers to the middle and inner ear. *Adv. Funct. Mater.* 31 (44), 2008701. doi:10.1002/adfm.202008701 <https://doi.org/10.1002/adfm.202008701>.
- [36] Zhao, X., Strickland, D. J., Derlet, P. M., He, M. r., Cheng, Y. J., Pu, J., et al. (2015). *In situ* measurements of a homogeneous to heterogeneous transition in the

plastic response of ion-irradiated $\langle 111 \rangle$ Ni microspecimens. *Acta Mater* 88, 121-135. <https://doi.org/10.1016/j.actamat.2015.01.007>.

4.6. SUPPORTING INFORMATION

4.6.1. CONVERGENCE STUDY OF THE FEA TORSION MODEL

Torsion testing was initially modeled on a simple cylinder with a diameter of 10 mm and a length of 20 mm. The output of the FEA simulation was the torque (reaction moment) and the shear stress of the cylinder after rotation. The assigned material properties ($E=2504$ MPa, $\nu=0.45$) were obtained from the conducted compression tests for the Grey resin pillars. Two reference points (RP) were created, at the center of the top and bottom parts of the cylinder, namely RP-1 and RP-2. The top and bottom surfaces of the cylinder were coupled to these reference points to constrain the motion of the coupled nodes to the rigid body motion of the reference point. RP-2 was then encastered (*i.e.*, constraining all translations U or rotations UR) while RP-1 was set to rotate by 0.2 radians. The torsion was modeled in the linear region and the angle of twist (θ) was calculated as:

$$\theta = TL/GJ \quad (\text{Eq. S4.1})$$

where T is the torque, L is the length of the cylinder, G is the shear modulus, and J is the second moment of area.

The shear modulus was calculated from the given material properties as:

$$E = 2G(1 + \nu) \quad (\text{Eq. S4.2})$$

To determine the size of the mesh required for accurate results, a mesh convergence study on three different types of mesh elements, namely on the eight-node brick element (C3D8), the ten-node tetrahedral element (C3D10), and the twenty-node brick element with reduced integration (C3D20R), was performed. The convergence study was performed for both the torque and shear stress. The theoretical values of the torque $T=8.48$ Nm and shear stress $\tau=43.17$ MPa were used as boundary conditions for the simulations. The comparison was made by calculating the respective torque using the resulting rotation angle and **Eq. 4.1-4.6**. We assumed convergence when the relative error with the theoretical values was below 5%. After processing the simulations, shear stress convergence was achieved with only 70 C3D8 elements, while 51414 C3D8 elements were required to converge for torque (**Figure S4.1A-B**). Similarly, 17755 C3D10 and 4500 C3D20R elements were required for shear stress

and 3477 C3D10 and 2420 C3D20R elements for torque, respectively. From these results, the C3D10 element models required the least CPU time (*i.e.*, 663 seconds per simulation), making them the most efficient simulations (**Figure S4.1C**). Therefore, the C3D10 mesh was used to model the torsion tests. The refinement of the number of elements was based on the shear stress convergence with a threshold of 1.0% and resulted in 25000 elements. Therefore, the C3D10 mesh was used to model the torsion tests. The refinement of the number of elements was based on the shear stress convergence with a threshold of 1.0% and resulted in 25000 elements.

4.6.2. FAILURE MODES OF SOLID GREY RESIN TORSION SPECIMENS

The torsion specimens exhibited different fracture angles. Those fracture angles have been either flat or inclined (**Table S4.1**). All torsion specimens failed either very close to the junction between the cubic and the cylindrical shaft or in the cylindrical shaft (**Figure S4.2**).

4.6.3. STATISTICAL EXPLORATION AND ANALYSIS

Shapiro-Wilk normality tests were performed on the datasets for the vertical and horizontal printed pillars in the two different layer thicknesses (25 μm and 50 μm) as part of the statistical exploration of the data before the statistical analysis. The results of the normality test are presented in QQ-normality plots (**Figure S4.3**) and the resulting p-values are presented in **Table S4.2**. The results of the one-way ANOVA statistical test are presented in the **Figure S4.4**.

LIST OF SUPPORTING TABLES

Table S4.1. Fracture angle measurement of the Grey resin torsion specimens in degrees (NM: non-measurable or flat, -: no sample)

Specimen	8R	16R	32R
1	NM	37°	33°
2	NM	36°	NM
3	44°	NM	31°
4	41°	-	-

Table S4.2. Normality test results from the data exploration step of the compression data of vertically and horizontally printed Grey resin pillars in two different layer thicknesses (*i.e.*, 25 μm and 50 μm). Shapiro-Wilk p -value < 0.05 confirms non-normal data distribution, justifying non-parametric analysis.

Shapiro-Wilk test for	p-value		Result
	25 μm	50 μm	
horizontally printed pillars			Passed normality?
E modulus	0.6369	0.4391	yes
Yield strength	0.4037	0.7335	yes
Shapiro-Wilk test for	p-value		Result
	25 μm	50 μm	
vertically printed pillars			Passed normality?
E modulus	0.9082	0.2541	yes
Yield strength	0.7156	0.9050	yes

LIST OF SUPPORTING FIGURES

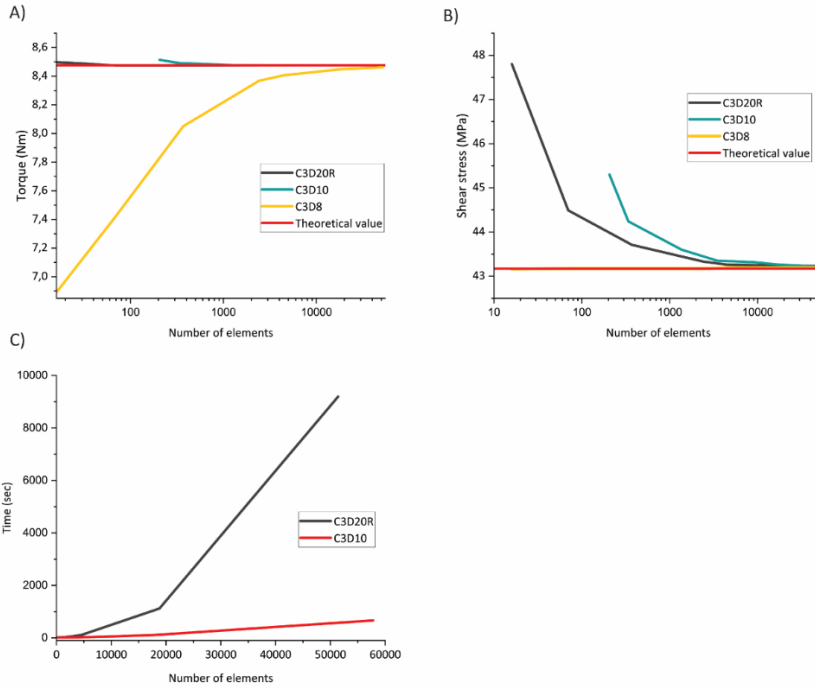


Figure S4.1. A convergence study of the torque and shear stress calculated by the FEA models for a cylinder: **(A)** The torque vs. the number of elements in the mesh for tetrahedral (C3D10) and hexahedral (C3D8, C3D20R) elements. **(B)** The shear stress vs. the number of elements in the mesh for tetrahedral (C3D10) and hexahedral (C3D8, C3D20R) elements. **(C)** The computational time (s) required to compute the model using the C3D10 or C3D20R type of elements.

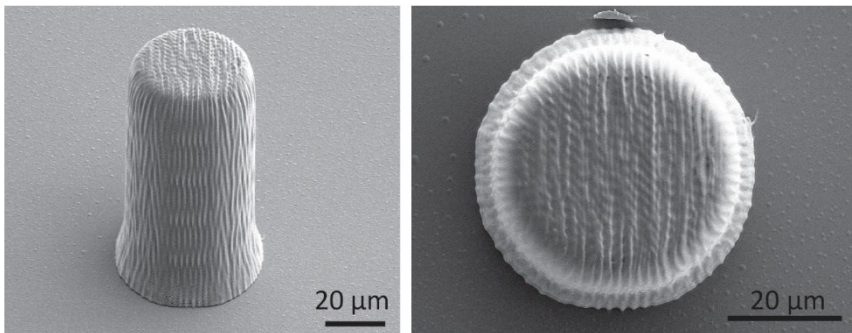


Figure S4.2. Tilted (left) and top (right) SEM image of the 2PP printed micropillars. Tilt angle = 30°. Scalebar = 20 μm.

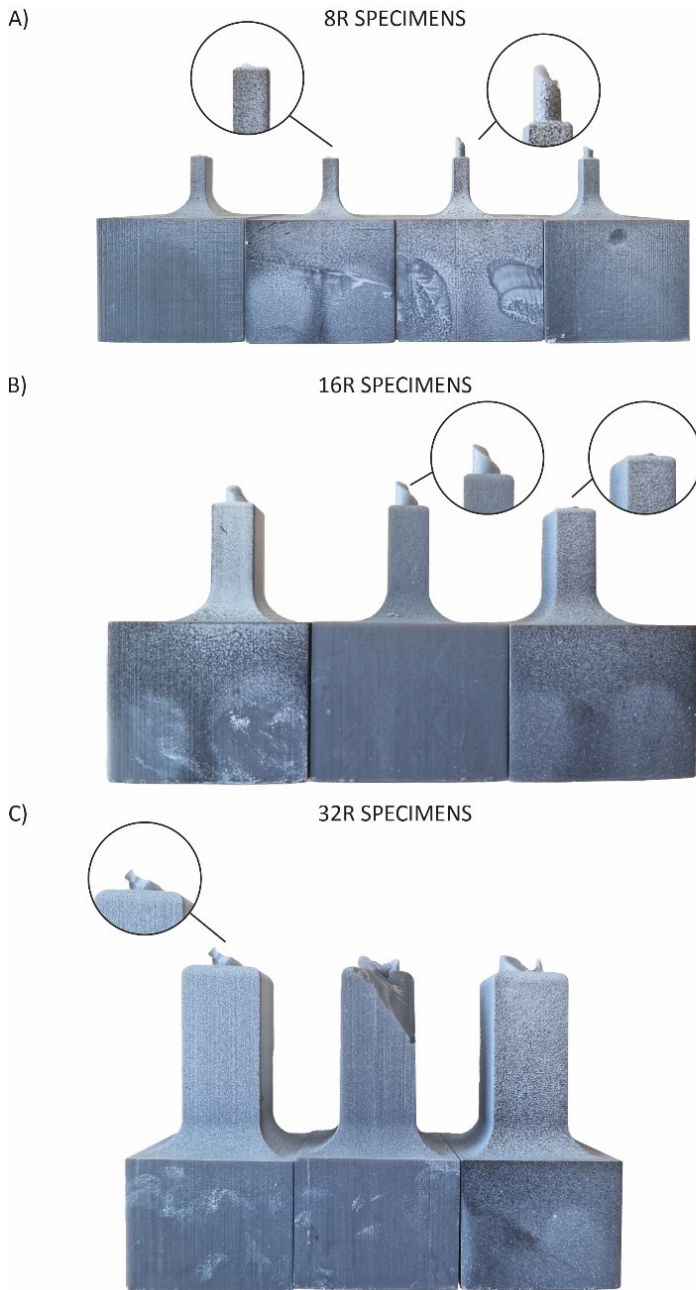


Figure S4.3. The optical images depicting the fracture angles of all solid Grey resin torsion specimens (i.e., 8R, 16R, 32R).

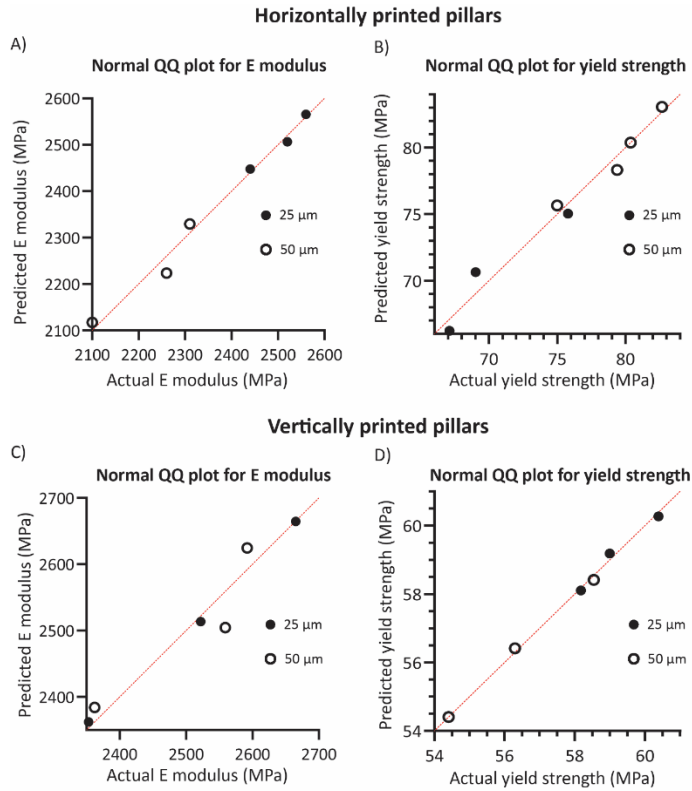


Figure S4.4. QQ normality plots for (A) the E modulus and (B) the yield strength of horizontally printed Grey resin pillars with 25 μm and 50 μm layer thickness, and for (C) the E modulus and (D) the yield strength of vertically printed Grey resin pillars with 25 μm and 50 μm layer thickness.

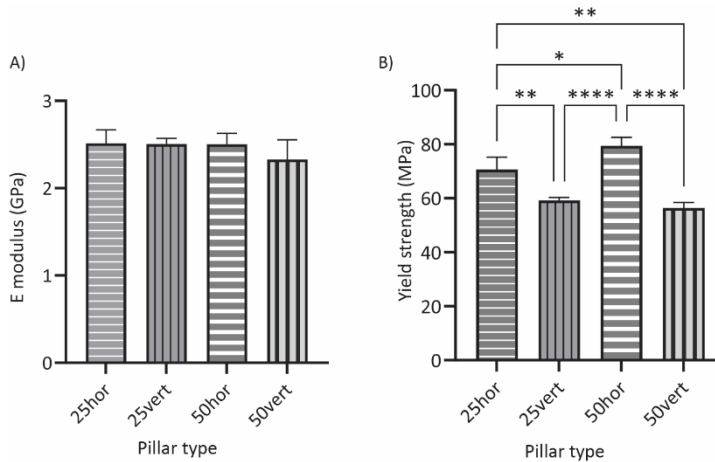
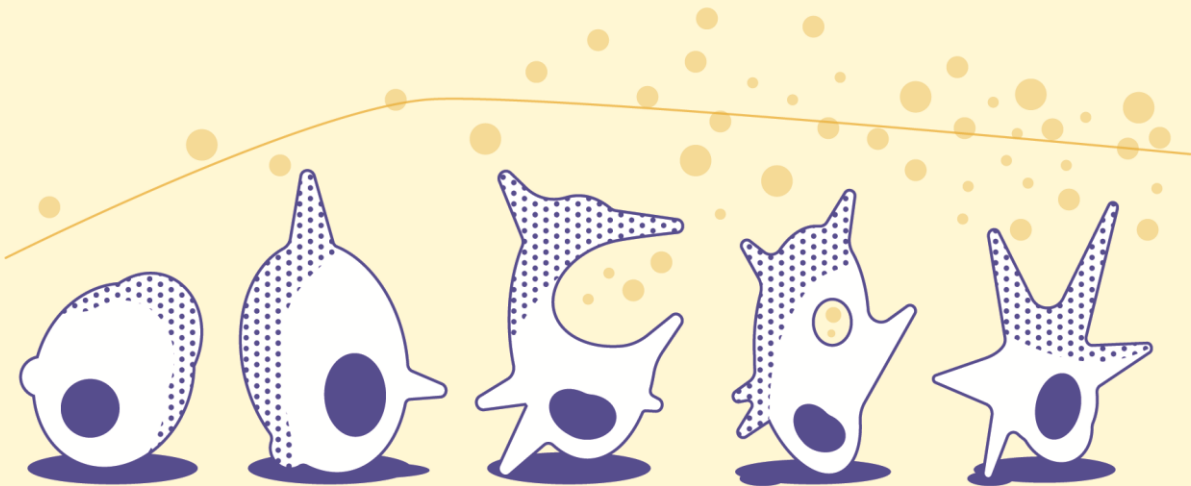


Figure S4.4. ANOVA results for (A) the E modulus and (B) the yield strength of horizontally printed Grey resin pillars with 25 μm and 50 μm layer thickness. The notation for $p < 0.05$ is one asterisk (*), for $p < 0.01$ two asterisks (**), for $p < 0.001$ three asterisks (***), and for $p < 0.0001$ four asterisks (****).

PART III - Chapter 05

Drug Release & Cell Tests



5. COCHLEAR IMPLANT DRUG LOADING AND RELEASE

Abstract

The intricate and vital sensory organ, the inner ear, presents challenges in treating auditory disorders due to the protective blood-labyrinth barrier, which impedes the effective delivery of drugs to the inner ear. Conventional therapeutic methods, including intratympanic and intracochlear injections, have limitations such as invasiveness and inefficient bioavailability. Additionally, treatments for inner ear disorders often lack efficacy due to the systemic administration of drugs and associated side effects. Therefore, cochlear implants offer a promising solution, enabling localized and sustained drug delivery. This paper investigates the release of a model drug from 3D-printed human cochlear implants, focusing on the influence of implant porosity and the pH of the artificial perilymph. A microporous (C60) and a hollow (CH) implant with anatomically relevant sizes for humans were fabricated using two-photon polymerization, loaded with ibuprofen and subjected to release experiments in artificial perilymph at pH 5.5 and pH 7.4. The results showed differences in drug release kinetics, with CH implants at physiological pH demonstrating faster release than the microporous ones. CH implants reached a release plateau around day 40, contrasting the sustained release observed in the porous C60 implants, which continued steadily releasing ibuprofen over the 84-day experimental period. Micro-computed tomography scans (μ -CT) provided insights into the spatial distribution of the drug within the implants, highlighting challenges in achieving uniform drug loading and release. The response of macrophages to the released ibuprofen revealed a dose-dependent upregulation of pro-inflammatory markers (*Il1b*, *Il6*, *Cd86*) and suppression of the anti-inflammatory marker *Cd206*, indicating a shift toward an M1-like phenotype. This study contributes to the development of localized and personalized cochlear drug delivery systems, offering sustained release and biological insight to improve therapeutic outcomes for auditory disorders.

Isaakidou A.*, Bedulho Das Lages Y.*, Bawuah P., Moosabeiki V., Verin J., Willart J.F., Klimopoulou M., Leeflang M.A., Mirzaali M.J., Zeitler A., Siepmann F., Apachitei I., Siepmann J., Fratila-Apachitei L.E. and Zadpoor A.A. Sustained drug release from 3D-printed microporous human cochlear implants fabricated by two-photon polymerization.

5.1. INTRODUCTION

The human inner ear is a complex sensory organ responsible for hearing and balance, safeguarded by the blood-labyrinth barrier (BLB) [1,2]. While the BLB plays a crucial protective role, its selective transport mechanisms pose a significant challenge for treating auditory disorders, as they limit drug penetration into the inner ear fluids [3]. Consequently, conditions such as noise-induced hearing loss, Ménière's disease, and sensorineural hearing loss remain challenging to treat due to inefficient drug delivery, highlighting the need for the development of tailored cochlear drug delivery systems [4–6]. Direct drug delivery strategies, which bypass the BLB, have gained attention for their ability to achieve higher localized drug concentrations while minimizing systemic side effects [7]. Approaches such as intratympanic and intracochlear injections, sometimes combined with hydrogels [8] and nanoparticles [9], have been explored as drug carriers. However, these methods often suffer from limitations, such as poor drug bioavailability [10], invasiveness [11], and slow-release kinetics within the cochlea, which hinder optimal treatment [12]. To address these challenges, innovative drug delivery platforms, such as implants placed through the round window membrane, are being investigated for controlled and sustained drug release [13–15]. Porous drug delivery systems have emerged as a promising alternative due to their ability to regulate the drug release rates [16–18]. These systems offer a promising solution for sustained, long-term drug release into the cochlea, potentially improving treatment outcomes (**Figure 5.1A**). Recently, rectangular and cylindrical cochlear implants with an internal porous structure, designed to conform to the human ear, have been investigated as an alternative to conventional drug delivery methods [19,20]. Fabricated using two-photon polymerization (2PP) process, these implants utilize micropores for drug storage and controlled release [19]. Mechanical assessments indicate that cylindrical implants exhibit superior strength relative to the rectangular ones, making them promising candidates for treating auditory disorders [20]. In this study, we investigated the use of 3D-printed cylindrical cochlear implants with distinct internal architectures for controlled and sustained ibuprofen delivery to the inner ear. Specifically, we examined how implant geometry (microporous versus hollow) influences drug loading efficiency and long-term release

behavior in artificial perilymph under acidic and physiological pH conditions, as pH fluctuations have been shown to contribute to hearing loss [21,22]. Furthermore, we analyzed the spatial distribution and crystallinity of ibuprofen within the implants using micro-computed tomography (μ -CT) and differential scanning calorimetry (DSC). Finally, based on the release profiles obtained from our release study, we assessed how exposure to ibuprofen-rich environments affect macrophage viability and inflammatory gene expression using cell viability assays and quantitative polymerase chain reaction (qPCR), providing insight into potential biological consequences of sustained local drug delivery.

5.2. MATERIALS AND METHODS

5.2.1. IMPLANT DESIGN AND FABRICATION

The implants were designed using SolidWorks (Dassault Systèmes SE, Vélizy-Villacoublay, France) and nTopology (nTopology Inc., New York, NY, US). The outer implant shape was a tapered-tip cylinder (C) with dimensions of $2.4 \times 0.6 \times 0.6 \text{ mm}^3$ ($L \times W \times H$). Two different implant designs were used to investigate the drug release (**Figure 5.1B**): (i) the C60 implant featuring an internal porous network with interconnected square pores of $60 \times 60 \mu\text{m}^2$ and (ii) a hollow implant (CH).

These implants were fabricated using 2PP with the Photonic Professional GT laser lithography system (Nanoscribe GmbH, Eggenstein-Leopoldshafen, Germany) and the IP-Q photoresist (Nanoscribe GmbH, Eggenstein-Leopoldshafen, Germany). This system utilizes a femtosecond fiber laser with a center wavelength of 780 nm, an 80 MHz repetition rate, and a 100 fs pulse duration. The designs were meshed and imported as standard tessellation language (STL) files into the job preparation software (Describe, Nanoscribe GmbH, Eggenstein-Leopoldshafen, Germany) before being transferred to the Photonic Professional GT machine for printing.

Silicon wafer substrates ($25 \times 25 \times 0.725 \text{ mm}^3$) were cleaned using acetone (Sigma-Aldrich, Hamburg, Germany) and isopropyl alcohol (IPA) (Sigma-Aldrich, Hamburg, Germany), then surface-activated with oxygen plasma for 15 minutes. Thereafter, the Si wafers were silanized for 1 hr in a 2% 3-(trimethoxysilyl)propyl methacrylate (MAPTMS, Sigma-Aldrich, Hamburg, Germany) ethanol solution, rinsed with

acetone (Sigma-Aldrich, Hamburg, Germany) and demineralized water, and blow-dried. A droplet of IP-Q photoresist was applied to the Si wafer, and the implants were printed in the galvo writing mode (dip-in configuration, DiLL) using a 10 \times objective with a numerical aperture (NA) of 0.3. The fabrication parameters were as follows: LP (laser power) = 50 mW, v (scanning speed) = 150 mm/s, s (slicing distance) = 5 μ m, and h (hatching distance) = 1 μ m. Following printing, the samples were developed in 1,2-propanediol monomethyl ether acetate (PGMEA, Sigma-Aldrich, Hamburg, Germany) for 25 minutes and methoxy-nonafluorobutane C₄F₉OCH₃ (Novac 7100, Sigma-Aldrich, Hamburg, Germany) for 30 seconds. They were then dried with compressed air before being removed from the Si wafer for further use.

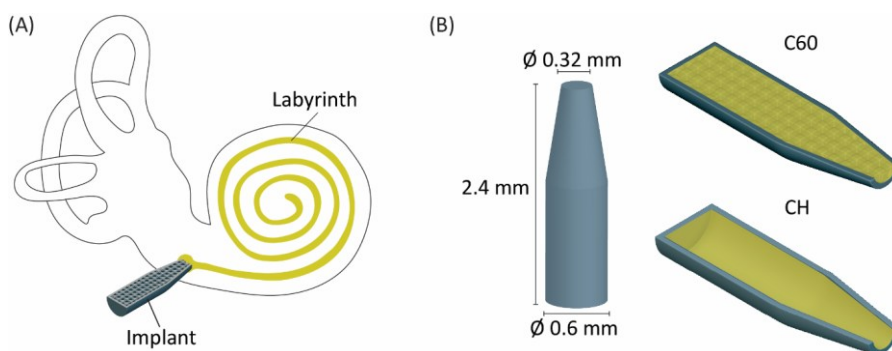


Figure 5.1. (A) Schematic representation of positioning a drug-loaded cochlear implant into the round window. (B) Schematic representation of the proposed geometry for a cochlear implant with dimensions and drug filling.

5.2.2. PREPARATION OF DRUG-LOADED IMPLANTS

To load the implants, 1 mL syringes were filled with ibuprofen powder (BASF, Ludwigshafen, Germany), sealed with flexible syringe caps (B. Braun Medical, Melsungen, Germany), and heated in an oven at 100 °C for 15 minutes to melt the ibuprofen. Each implant was positioned halfway inside a 200 μ L micropipette (Eppendorf, Hamburg, Germany) with its tapered end directed inward. It was connected to a microfluidic system using adapters, unions, and tubing (Figure 5.2A). Melted ibuprofen was injected through the implant under controlled conditions, ensuring consistent drug loading. Each syringe was used to fill a single implant.

A total of seventeen C60 and fourteen CH cochlear implants were loaded with ibuprofen. After loading, the implants were refrigerated overnight at $-20\text{ }^{\circ}\text{C}$, and excess ibuprofen on the exterior was carefully removed using an ethanol-wetted lint-free tissue (**Figure S5.1A**).

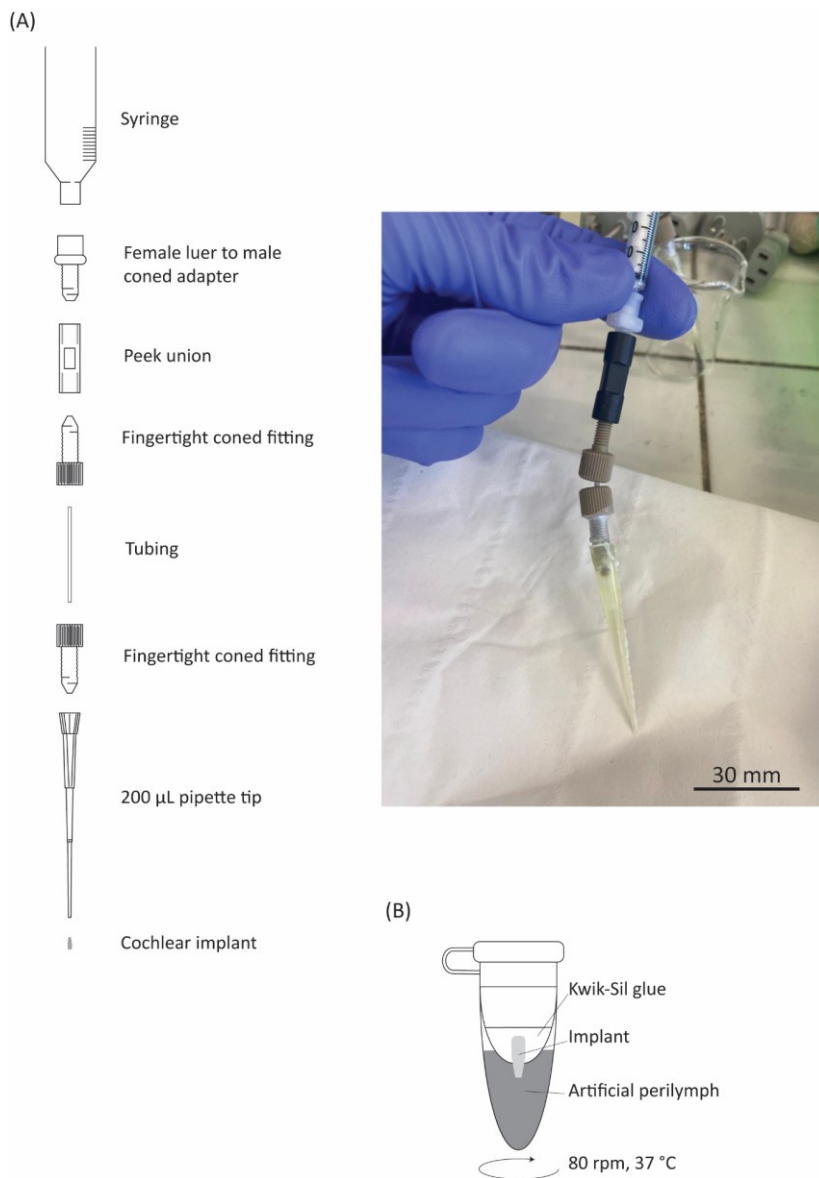


Figure 5.2. (A) Diagram and photo of the individual components in the order of assembly for the drug loading system. (B) Diagram of the experimental setup used for the drug release measurements from the C60 and CH implants.

5.2.3. IBUPROFEN RELEASE MEASUREMENTS

The ibuprofen-loaded implants were exposed to artificial perilymph with two different pH levels, pH 5.5 and pH 7.4 (**Table 5.1**). Fourteen samples from the C60 implants and eleven samples from the CH implants were analyzed for release kinetics. μ -CT imaging was performed on three samples per group (**Figure S5.1B**).

A two-vial system was used for controlled-release measurements, allowing for frequent sampling and refreshing of the artificial perilymph (**Figure 5.2B**). The implant was fixed in a 0.2 mL vial (Eppendorf, Hamburg, Germany) with a hole at the bottom, secured with Kwik-Sil silicone glue (WPI, Sarasota, USA). This inner vial was placed inside another 0.2 mL vial containing 0.12 mL artificial perilymph, ensuring continuous immersion of the implant tip. The setup was incubated at 37 °C, shaken at 80 rpm (GFL 3033 horizontal shaker), and sampled at predefined time points.

High-Performance Liquid Chromatography with Ultraviolet detection (HPLC-UV) analysis was performed using an Alliance e2695 system (Waters Division, Milford, USA) equipped with a UV detector. 20 μ L of release medium was injected into a reverse-phase column C18 (Gemini 3 μ m, 110 Å, 100 \times 4.6 mm, Phenomenex, Le Pecq, France). Ibuprofen detection was conducted with a mobile phase (33% acetonitrile/67% phosphate buffer, with pH 6.8), at a flow rate of 1 mL/min, and a detection wavelength of 225 nm. The retention time was approximately 5 minutes.

Table 5.1. Artificial perilymph composition for pH 5.5 and pH 7.4.

Artificial Perilymph Recipes	
pH 5.5	pH 7.4
1.2 mM calcium chloride dihydrate	136 mM sodium chloride
2.78 mM magnesium sulphate monohydrate	2.7 mM potassium chloride
2.7 mM potassium chloride	8.1 mM disodium phosphate
5 mM HEPES Pufferan	1.47mM monopotassium phosphate
145 mM sodium chloride	

5.2.4. MICRO-COMPUTED TOMOGRAPHY OF THE IMPLANTS

Empty and ibuprofen-loaded implants were analyzed using X-ray μ -CT with a Skyscan 1172 scanner (Bruker, Antwerp, Belgium), employing a source voltage of 34 kV and a current of 210 μ A in a cone-beam configuration, without the use of any

filter. The samples were placed vertically on the sample holder and were rotated 360° in steps of 0.25°, generating about 1440 2D projections at each rotation step with an isotropic voxel resolution of 2.49 μm. Using an exposure time of 1600 ms per image, the total scan duration for each sample was approximately 2 hours. The NRecon software (Version 1.7.4.2, Bruker, Antwerp, Belgium) was used to reconstruct the 2D projection images into a cross-sectional image of the samples. The reconstructed cross-sectional images were aligned using the DataViewer software (Version 1.5.6.2, Bruker, Antwerp, Belgium) and imported into Dragonfly Pro (Version 2022.1 Build 1249) for quantitative segmentation and porosity analysis. Thresholding was achieved using Otsu's method and was applied across samples to segment solid material (polymer and/or drug) from void space. Void fraction (porosity) was computed as the ratio of void voxels to total voxels within the defined implant volume. Fiji/ImageJ and CTvox were used only for visualization and figure/video generation. The pixel size was 2.49 × 2.49 × 2.49 μm³, consistent with the acquisition settings, and it was sufficient to resolve the designed pore architecture (~60 μm), but not sub-micron fabrication features such as the 1 μm hatching distance used during two-photon polymerization.

5.2.5. THERMAL ANALYSIS OF THE DRUG AND IMPLANTS

DSC thermograms of the ibuprofen powder, the IP-Q implant material, and the ibuprofen-loaded implants were recorded using a DSC Q1000 (TA Instruments, Leatherhead, UK). Each sample was placed in the refrigerator for 24 hours before analysis to ensure complete crystallization and maintain consistency with the drug release protocol described in **Section 5.2.3**. Samples of 5 mg of ibuprofen, 2.7 mg of IP-Q, 2.2 mg of ibuprofen-loaded C60, and 0.6 mg of ibuprofen-loaded CH were heated in hermetic aluminum pans from -60 °C to 100 °C at a heating rate of 5 °C/min. During the DSC analysis the samples were flushed with highly pure nitrogen gas. Temperature and enthalpy readings were calibrated using pure indium at the same scan rates used in the experiments.

5.2.6. MACROPHAGE CULTURE WITH IBUPROFEN-RICH MEDIUM

Murine macrophages (J774A.1) (DSMZ, Braunschweig, Germany), at passage 14, were pre-cultured in 75 cm² flasks (Greiner Bio-One GmbH, Alphen aan den Rijn, the Netherlands) at a concentration of 5×10^5 cells per mL with 10 mL of Dulbecco's Modified Eagle's medium (DMEM) (Thermo Fisher Scientific, Landsmeer, the Netherlands) at 37 °C and 5.0% CO₂ for 3 days. To induce M1 polarization, the cells were stimulated with 100 ng/mL lipopolysaccharide (LPS) (Merck Sigma, Zwijndrecht, the Netherlands) and 10 ng/mL interferon-gamma (IFN- γ) (Merck Sigma, Zwijndrecht, the Netherlands) for 24 hours. Following stimulation, the cells were seeded into 48-well plates (Greiner Bio-One GmbH) at a concentration of 3500 cells/mL in 0.5 mL of ibuprofen-enriched medium containing 0.04, 0.10, or 0.30 mg/mL ibuprofen (BASF, Ludwigshafen, Germany). These concentrations were selected based on the ibuprofen release profiles observed from the C60 and CH drug-eluting implants developed in this study. Cells cultured in ibuprofen-free medium served as the untreated control. Cell viability was investigated after 48 h of ibuprofen exposure using live/dead staining (Viability/Cytotoxicity Kit #L3224, Landsmeer, the Netherlands). Fluorescence images were acquired to qualitatively evaluate the presence of viable (green) and non-viable (red) cells under each treatment condition.

After 48 hours of exposure, the RNA was extracted using the RNeasy kit (Qiagen, Venlo, the Netherlands) according to the manufacturer's instructions. Complementary DNA (cDNA) synthesis was performed using the QuantiTect Reverse Transcription kit (Qiagen, Venlo, the Netherlands). Quantitative PCR (qPCR) was conducted using the QuantiNova SYBR Green PCR kit (Qiagen, Venlo, the Netherlands) on a Rotor-Gene Q 2Plex thermal cycler (Qiagen, Venlo, the Netherlands). The expression of M1-associated genes (*Il1b*, *Il6*, *Cd86*) and M2-associated genes (*Il10*, *Tgfb*, *Cd206*) was assessed, and the *Ubc* gene was used as the housekeeping reference (Integrated DNA Technologies, Leuven, Belgium) (**Table S5.1**). Relative gene expression levels were calculated using the $2^{-\Delta\Delta Ct}$ method, where expression was normalized to *Ubc* and expressed relative to the untreated control condition. All experimental conditions were tested in triplicate.

5.2.7. STATISTICAL ANALYSIS

The data are presented as mean \pm standard deviation. A Welch's *t*-test was used to assess differences in the ibuprofen loading amount between the porous C60 and hollow CH implants ($p \leq 0.05$). Gene expression data were analyzed using a non-parametric one-way ANOVA (Kruskal-Wallis test) followed by Dunn's *post-hoc* test to assess differences between treatment groups ($p \leq 0.05$). All statistical analyses were performed using Prism 10 (GraphPad Software, San Diego, CA, USA).

5.3. RESULTS

5.3.1. IBUPROFEN LOADING, CRYSTALLINITY, AND DISTRIBUTION INSIDE THE COCHLEAR IMPLANTS

Ten ibuprofen-loaded implants from each implant type (C60 and CH) were used to assess the amount of loaded ibuprofen. A statistically significant difference was observed between the C60 and CH types (**Figure 5.3A**), with the amount of loaded ibuprofen in the C60 implants being $86 \pm 44 \mu\text{g}$ and in the CH implants being $240 \pm 120 \mu\text{g}$.

The DSC thermogram of ibuprofen showed a melting temperature of 76.41°C for the pure drug. In contrast, the microporous C60 and hollow CH implants loaded with ibuprofen revealed endotherms at approximately 74.17°C and 74.65°C , respectively. Within the range of -60°C to 90°C , the thermoset resin (pure IP-Q) exhibited no thermal events (**Figure 5.3B**).

μ -CT was used to assess the morphology of the C60 and CH implants before drug loading and to evaluate the spatial distribution of voids within the implants after loading (**Figure 5.3C**). The findings revealed that the micropore geometry aligned consistently with the intended design across the entire volume of the C60 implants. Similarly, the overall shape and wall thickness of the CH implants were preserved. Due to the similar X-ray attenuation coefficients of the IP-Q photoresist and ibuprofen, μ -CT does not allow direct distinction between polymer and drug. Consequently, the analysis identifies voids (*i.e.*, regions not occupied by polymer and/or drug), and the reported porosity values reflect the void fraction only. Porosity measurements (**Table 5.2**) revealed a decrease in porosity of the loaded implants, indicating partial filling of

the internal void space following ibuprofen loading. In the case of C60 implants, the porosity decreased from 28% to 18%, suggesting that the microporous network was not fully loaded with the drug (**Figure 5.3C**). By comparison, the hollow CH implants exhibited a porosity of 8% after drug loading, indicating that most of the internal cavity was filled with ibuprofen, albeit some empty zones were observed along the implant's length (**Figure 5.3C**). The μ -CT analysis thus indicates that ibuprofen loading did not result in homogeneous filling of the internal void space in either implant type. Instead, spatial heterogeneities and residual voids were observed along the implant length.

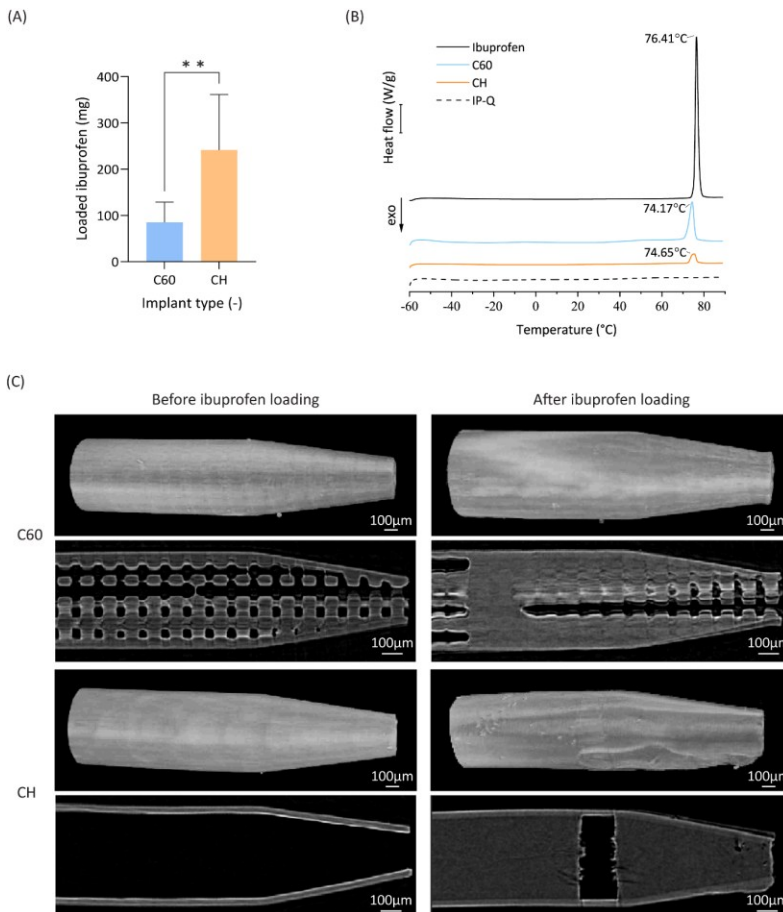


Figure 5.3. (A) Amount of loaded ibuprofen in C60 and CH types of implants ($p^* \leq 0.05$, $p^{**} \leq 0.01$). (B) DSC thermograms of ibuprofen of a drug-free (IP-Q) and an ibuprofen-loaded cochlear implants (C60, CH). (C) μ -CT images of the external and internal geometry of the two types of cochlear implants (*i.e.*, C60 and CH) before and after ibuprofen loading.

Table 5.2. Calculated porosity of C60 and CH cochlear implants before and after ibuprofen loading.

	C60	Loaded C60	Loaded CH
Solid volume (mm ³)	0.44	0.44	0.37
Void volume (mm ³)	0.12	0.08	0.03
Porosity (%)	28	18	8

5.3.2. EFFECT OF IMPLANT ARCHITECTURE AND pH ON THE RELEASE OF IBUPROFEN

The release kinetics of ibuprofen revealed distinct differences between the microporous C60 and the hollow CH implants (**Figure 5.4**). In the perilymph with a pH of 5.5, the cumulative drug release after 84 days from the C60 implants was between 20 and 60 μg (**Figure 5.4A**). In contrast, the CH implants exhibited a cumulative ibuprofen release of 30 and 80 μg over the same period and at the same pH (**Figure 5.4C**). Similarly, in the perilymph with a pH of 7.4, C60 implants released an amount of ibuprofen ranging between 60 and 180 μg after 84 days (**Figure 5.4B**), while CH implants released 100 to 400 μg of ibuprofen, thus approximately four times more at the same pH and over the same period (**Figure 5.4D**). Moreover, at pH 7.4, CH implants exhibited faster release, reaching a plateau around day 40, while porous C60 implants continued to release steadily over the next 44 days.

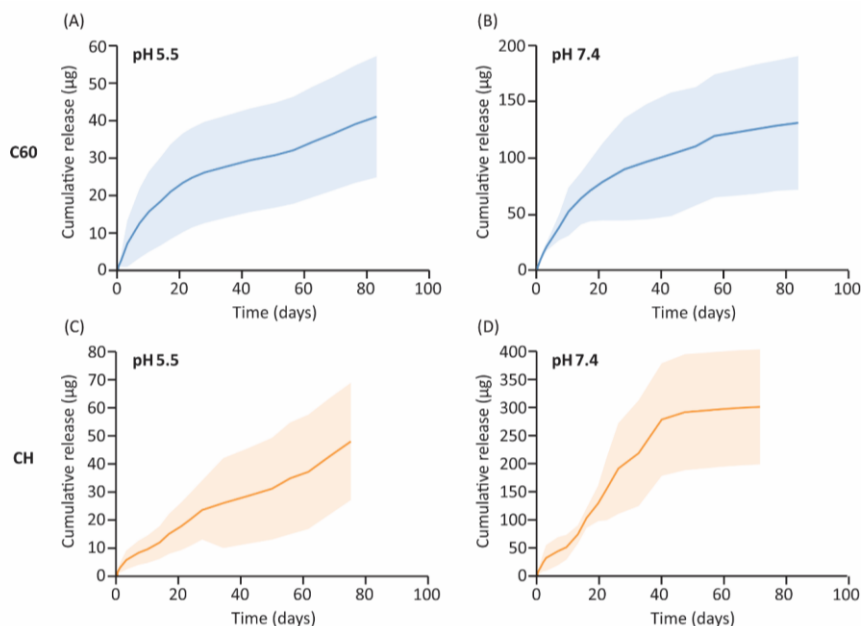


Figure 5.4. Cumulative ibuprofen release profiles from C60 and CH implants under different pH conditions. **(A)** C60 implant at pH 5.5. **(B)** C60 implant at pH 7.4. **(C)** CH implant at pH 5.5. **(D)** CH implant at pH 7.4. Solid lines represent the mean cumulative release, while the shaded areas indicate the standard deviation. Average and standard deviation from a minimum of 5 and a maximum of 7 samples per group (see **Figure S5.2**).

5.3.3. MACROPHAGE VIABILITY AND GENE EXPRESSION PROFILE IN RESPONSE TO IBUPROFEN TREATMENT

Viability of M1-stimulated macrophages following ibuprofen exposure

Live/Dead staining performed after 48 h of exposure showed that macrophage viability was preserved across all ibuprofen concentrations (0.04–0.30 mg/mL), with predominantly viable cells observed in all conditions (**Figure S5.3**). A decrease in the overall cell number was observed with increasing ibuprofen concentration. Data are representative of three independent experiments, each performed in triplicate.

Gene expression of M1-stimulated macrophages following ibuprofen exposure

To assess the immunomodulatory effects of ibuprofen on M1-stimulated macrophages, we analyzed the expression levels of M1-associated (*Il1b*, *Il6*, and *Cd86*) and M2-associated (*Tgfb*, *Il10*, and *Cd206*) genes after a 48-hour exposure to ibuprofen at concentrations of 0.04, 0.10, and 0.30 mg/mL.

The fold-change analysis relative to the untreated controls showed that all the M1-associated genes were upregulated in the presence of ibuprofen. Furthermore, the effects increased with ibuprofen concentration, and more specifically, *Il1b* and *Il6* showed a robust, dose-dependent increase in expression, with several replicates at the highest dose reaching or exceeding a 15-fold upregulation relative to untreated controls (**Figure 5.5A**). *Cd86* was also significantly elevated, particularly at 0.10 and 0.30 mg/mL, indicating an increased pro-inflammatory response.

By comparison, among the M2 genes, *Il10* expression remained low and relatively unchanged across all treatment conditions, with fold changes of less than 1.0 in all replicates (**Figure 5.5B**). *Tgfb* was upregulated in all treated samples, and the *Cd206* surface marker exhibited comparable levels with the control at the lowest ibuprofen concentrations but showed downregulation with increasing ibuprofen concentrations. These findings suggest that ibuprofen exposure of M1-stimulated macrophages at concentrations between 0.04 and 0.30 mg/mL further enhances the M1 polarization of the macrophages.

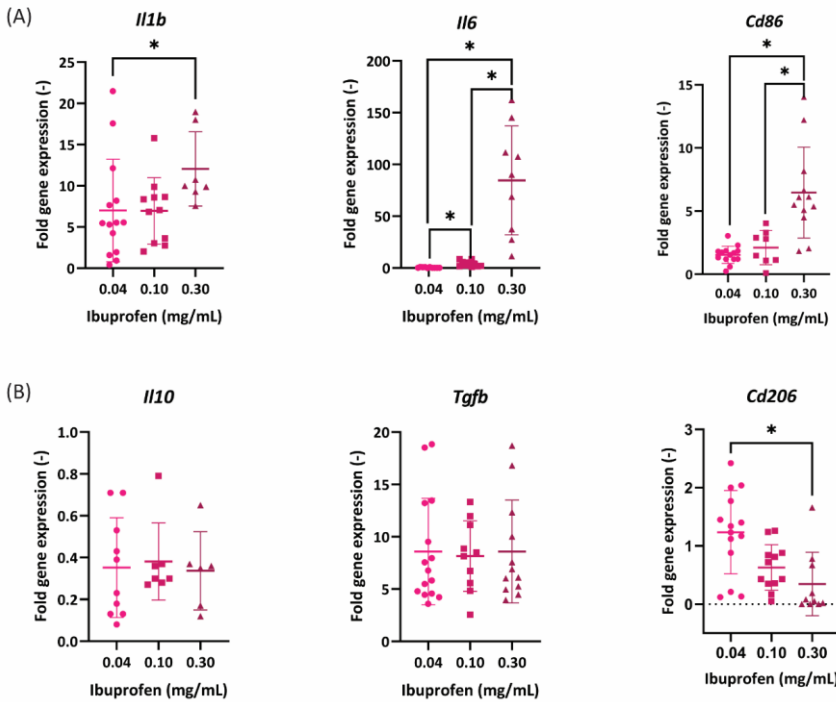


Figure 5.5. Relative expression levels of (A) M1-associated genes and (B) M2-associated genes following 48 h ibuprofen treatment, expressed as fold change relative to untreated controls, after normalization to the *Ubc* housekeeping gene. Data are presented as individual replicates with mean \pm standard deviation. Statistical significance was assessed using Kruskal–Wallis test followed by Dunn’s post-hoc test ($p < 0.05$).

5.4. DISCUSSION

This study investigated the potential of 3D-printed human cochlear implants featuring hollow (CH) and microporous (C60) architectures to enable sustained and localized drug release to the inner ear. The investigation focused on the influence of porosity and pH on drug release kinetics and their consequences on macrophage polarization. Our findings confirm that the implant design greatly influences drug loading, release profiles, and biological indicators, offering a promising direction for localized drug delivery to the human cochlea.

5.4.1. IBUPROFEN LOADING AND RELEASE

A key challenge during the study was achieving consistent and repeatable loading of crystalline ibuprofen into the implants. Although both designs demonstrated

successful loading, inconsistencies arose due to pressure buildup and air entrapment during the filling process. Thermal analysis confirmed that the ibuprofen loaded in the implants retained its crystalline nature, with no detectable glass transition at -46 °C [23] and melting peaks near 76 °C [23,24]. Slight reductions in melting temperature (-2 °C) were observed in both implant types suggesting confinement-induced crystallite size reduction, particularly in C60 implants, where the smaller total drug volume and higher surface-to-volume ratio favored the formation of smaller crystallites. These findings highlight the influence of implant architecture not only on the quantity of drug loaded but also on its physical state.

Release profiles showed notable variability among samples (**Figure S5.2**). This was partly attributable to differences in the positioning of the drug within the implant. The semi-hydrophobic nature of the implant material [19] and the narrow outlet (0.6 mm) likely limited water ingress, especially when the drug was positioned away from the opening or interrupted by air gaps. The hollow CH implants enabled more direct contact between the drug and the release medium, leading to dissolution-based release [25], whereas C60 implants induced a more diffusion-dominated behavior due to their internal porosity. Environmental pH also played a critical role. At pH 7.4, representative of healthy cochlear conditions, the solubility of ibuprofen is high (≈ 3.37 mg/mL), resulting in accelerated release. Conversely, at pH 5.5, which is relevant for inflammatory or pathological states, solubility decreases (≈ 0.084 mg/mL), thereby reducing the dissolution rate and making the process more diffusion-controlled [25]. Under acidic conditions, the influence of geometry on release diminished, suggesting that solubility may become the primary limiting factor.

5.4.2. MACROPHAGE RESPONSE TO THE RELEASED IBUPROFEN

Ibuprofen is classically described as an anti-inflammatory agent through the inhibition of cyclooxygenase (COX) and the consequent reduction of prostaglandin synthesis, particularly PGE₂ [26]. However, the macrophage response observed in this study did not align with these classical anti-inflammatory effects. Instead, we found that ibuprofen exposure further increased the expression of M1-associated markers (*Il1b*, *Il6*, and *Cd86*), in already M1-stimulated macrophages, while M2-associated markers (*Il10*, *Tgfb*, and *Cd206*) were either unchanged or suppressed at higher doses.

These results suggest that ibuprofen may not act as a direct anti-inflammatory stimulus at the macrophage level but rather may skew macrophages toward a pro-inflammatory phenotype. This dose-dependent enhancement of pro-inflammatory gene expression was most pronounced at 0.30 mg/mL, suggesting that macrophage responses may be dependent on the ibuprofen concentration.

Although PGE₂ is commonly associated with pro-inflammatory signaling, it can also exert regulatory or anti-inflammatory effects in macrophages as a negative-feedback regulator that can limit excessive inflammatory activation and promote wound healing [27,28]. When ibuprofen inhibits COX activity, it subsequently reduces PGE₂ synthesis and therefore bypasses this homeostatic component that can lead to an upregulation of the expression levels of pro-inflammatory cytokines.

In addition to PGE₂ suppression, ibuprofen concentrations have been reported to influence macrophage behavior through other pathways. A study showed that ibuprofen alone (10 - 100 μM) could not reduce the oxidative stress induced by stimulation with LPS [29]. Elevated oxidative stress is a known activator of NF-κB, which directly drives transcription of IL-1β, IL-6, and CD86. Another study showed a downregulation of both M1- and M2-associated markers in THP-1-derived macrophages when exposed to 100-800 μM ibuprofen for 2 hours via the PARP-1 and NF-κB signaling pathways [30].

Taken together, the amplified M1-like phenotype observed in our study may arise from the combined effects of reduced PGE₂ signaling, increased oxidative stress, pre-existing M1 polarization, and exposure to higher ibuprofen concentrations than those typically associated with anti-inflammatory effects. Macrophages were first polarized to an M1 phenotype using LPS and IFN-γ before exposure to ibuprofen, which may have predisposed them toward an intensified inflammatory response. Additionally, the ibuprofen concentrations used here (0.04–0.30 mg/mL; 0.19–1.45 mM) exceed those typically applied in studies demonstrating anti-inflammatory effects (10–100 μM), suggesting that higher cumulative exposure may have contributed to the observed gene expression patterns. Moreover, whether the concentrations used in our experiments reflect physiologically relevant levels in the

cochlear microenvironment remains to be determined, especially given that *in vivo* drug concentrations depend heavily on the route of administration.

Live/Dead staining confirmed macrophage viability at all tested ibuprofen concentrations, indicating that the observed upregulation of M1-associated genes was not driven by cytotoxicity but rather by a transcriptional response of viable cells. The overall reduced number of cells observed with increasing ibuprofen concentration could suggest altered proliferation and cell adhesion. Further studies employing quantitative viability and proliferation assays could fully elucidate the concentration-dependent effects of ibuprofen on macrophage behavior.

From a design standpoint, this immune activation highlights the need to refine the implants further. Future work should focus on optimizing the design to control the release kinetics more precisely, as well as on developing loading methods to enhance the uniformity and spatial distribution of the drug. Additionally, testing in complex biological environments, including cochlear cell co-cultures or *in vivo* models, is essential to evaluate whether the observed pro-inflammatory skewing translates to detrimental or beneficial outcomes in the inner ear context.

Despite these uncertainties and the need for further exploration, the implants developed in this study enable the local delivery of drugs, offering the possibility of tailoring the drug dose, spatial distribution inside the implants, and release duration. With continued refinement, these implants may serve as customizable tools for delivering active pharmaceutical ingredients to the cochlea and modulating the immune response, contributing to therapeutic strategies for auditory disorders.

5.5. CONCLUSION

The current research seeks to bridge the gap between conventional drug delivery systems and the need for local and potentially personalized medicine in treating auditory disorders. By exploring the potential of porous cochlear implants fabricated via 2PP as a platform for controlled and sustained ibuprofen release, this study demonstrates that implant porosity significantly impacts drug loading efficiency, spatial distribution and release kinetics. The hollow CH implants exhibited greater drug loading and faster release, whereas the porous C60 implants achieved more controlled and prolonged drug release. The findings highlight the promise of porous

cochlear implants for localized and sustained drug delivery to the inner ear. While challenges remain in optimizing drug loading reproducibility, and immunomodulatory effects, this study paves the way for future investigations into personalized cochlear drug therapies. Further studies should focus on long-term stability, mechanical robustness, and *in vivo* immunological responses to advance this technology toward clinical applications in the treatment of auditory disorders.

REFERENCES

- [1] C. Kämpfe Nordström, N. Danckwardt-Lillieström, G. Laurell, W. Liu, H. Rask-Andersen, The Human Endolymphatic Sac and Inner Ear Immunity: Macrophage Interaction and Molecular Expression, *Front. Immunol.* 9 (2019). <https://doi.org/10.3389/fimmu.2018.03181>.
- [2] H. Liu, J. Hao, K.S. Li, Current strategies for drug delivery to the inner ear, *Acta Pharm. Sin. B* 3 (2013) 86-96. <https://doi.org/10.1016/j.apsb.2013.02.003>.
- [3] S. Dash, J. Zuo, P.S. Steyger, Local Delivery of Therapeutics to the Cochlea Using Nanoparticles and Other Biomaterials, *Pharmaceuticals* 15 (2022) 1115. <https://doi.org/10.3390/ph15091115>.
- [4] G. Altissimi, A. Colizza, G. Cianfrone, M. de Vincentiis, A. Greco, S. Taurone, A. Musacchio, A. Ciofalo, R. Turchetta, D. Angeletti, M. Ralli, Drugs inducing hearing loss, tinnitus, dizziness and vertigo: an updated guide, *Eur Rev Med Pharmacol Sci* 24 (2020) 7946-7952. https://doi.org/10.26355/eurrev_202008_22477.
- [5] F. Piu, K.M. Bishop, Local Drug Delivery for the Treatment of Neurotology Disorders, *Front Cell Neurosci* 13 (2019) 238. <https://doi.org/10.3389/fncel.2019.00238>.
- [6] A.A. McCall, E.E. Swan, J.T. Borenstein, W.F. Sewell, S.G. Kujawa, M.J. McKenna, Drug delivery for treatment of inner ear disease: current state of knowledge, *Ear Hear.* 31 (2010) 156-165. <https://doi.org/10.1097/AUD.0b013e3181c351f2>.
- [7] A.N. Salt, S.K. Plontke, Principles of Local Drug Delivery to the Inner Ear, *Audiology and Neurotology* 14 (2009) 350-360. <https://doi.org/10.1159/000241892>.
- [8] K. Mfoafo, R. Mittal, A. Eshraghi, Y. Omidi, H. Omidian, Improved inner ear drug delivery using hydrogel carriers, *J. Drug Deliv. Sci. Technol.* 79 (2023) 104086. <https://doi.org/10.1016/j.jddst.2022.104086>.
- [9] J. Zou, R. Sood, S. Ranjan, D. Poe, U.A. Ramadan, P.K. Kinnunen, I. Pyykkö, Manufacturing and in vivo inner ear visualization of MRI traceable liposome nanoparticles encapsulating gadolinium, *J. Nanobiotechnology* 8 (2010) 32. <https://doi.org/10.1186/1477-3155-8-32>.
- [10] S. Nyberg, N.J. Abbott, X. Shi, P.S. Steyger, A. Dabdoub, Delivery of therapeutics to the inner ear: The challenge of the blood-labyrinth barrier, *Sci. Transl. Med.* 11 (2019) eaao0935. <https://doi.org/10.1126/scitranslmed.aao0935>.
- [11] E. Lehner, M. Menzel, D. Gündel, S.K. Plontke, K. Mäder, J. Klehm, H. Kielstein, A. Liebau, Microimaging of a novel intracochlear drug delivery device in

- combination with cochlear implants in the human inner ear, *Drug Deliv. Transl. Res.* 12 (2022) 257–266. <https://doi.org/10.1007/s13346-021-00914-9>.
- [12] E.E.L. Swan, M.J. Mescher, W.F. Sewell, S.L. Tao, J.T. Borenstein, Inner ear drug delivery for auditory applications, *Adv. Drug Deliv. Rev.* 60 (2008) 1583–1599. <https://doi.org/10.1016/j.addr.2008.08.001>.
- [13] M. Gehrke, J. Sircoglou, D. Gnansia, G. Tourrel, J.F. Willart, F. Danede, E. Lacante, C. Vincent, F. Siepmann, J. Siepmann, Ear Cubes for local controlled drug delivery to the inner ear, *Int. J. Pharm.* 509 (2016) 85–94. <https://doi.org/10.1016/j.ijpharm.2016.04.003>.
- [14] J. Sircoglou, M. Gehrke, M. Tardivel, F. Siepmann, J. Siepmann, C. Vincent, Trans-Oval-Window Implants, A New Approach for Drug Delivery to the Inner Ear, *Otology & Neurotology* 36 (2015) 1572–1579. <https://doi.org/10.1097/MAO.0000000000000855>.
- [15] M. Gehrke, J. Verin, D. Gnansia, G. Tourrel, M. Risoud, C. Vincent, F. Siepmann, J. Siepmann, Hybrid Ear Cubes for local controlled dexamethasone delivery to the inner ear, *European Journal of Pharmaceutical Sciences* 126 (2019) 23–32. <https://doi.org/10.1016/j.ejps.2018.04.045>.
- [16] F. Huang, S. Yang, H. Wang, P. Zhao, B. Zhou, B. Cheng, S. Dong, J. Yang, B. Li, X. Wang, pH-responsive PLGA/gelatin porous microspheres containing paclitaxel used for inhibition of cancer cell proliferation, *J. Drug Deliv. Sci. Technol.* 86 (2023) 104735. <https://doi.org/10.1016/j.jddst.2023.104735>.
- [17] S. Du, Y. Wei, Y. Tan, Y. Li, J. Li, T. Wu, L. Han, M. Wang, S. Ahmed, W. Zhou, L. Wu, T. Zhang, Self-assembled mesoporous particles of *Antheraea pernyi* silk fibroin for encapsulation and sustained release of 5-fluorouracil, *Colloids Surf. A Physicochem. Eng. Asp.* 673 (2023) 131772. <https://doi.org/10.1016/j.colsurfa.2023.131772>.
- [18] S. Sajjadi, A. Gholizadeh-Hashjin, F. Shafizadeh, S. Marefat, S. Hamidi, A. Farjami, Advancing biomedicine with gel-based materials and composites: A comprehensive review, *J. Appl. Polym. Sci.* (2023). <https://doi.org/10.1002/app.54641>.
- [19] A. Isaakidou, I. Apachitei, L.E. Fratila-Apachitei, A.A. Zadpoor, High-Precision 3D Printing of Microporous Cochlear Implants for Personalized Local Drug Delivery, *J. Funct. Biomater.* 14 (2023) 494. <https://doi.org/10.3390/jfb14100494>.
- [20] A. Isaakidou, M. Ganjian, R. van Hoften, M.C. Saldivar, M.A. Leeflang, A. Groetsch, M. Wątroba, J. Schwiedrzik, M.J. Mirzaali, I. Apachitei, L.E. Fratila-Apachitei, A.A. Zadpoor, Multi-scale in silico and ex silico mechanics of 3D

- printed cochlear implants for local drug delivery, *Front. Bioeng. Biotechnol.* 11 (2024). <https://doi.org/10.3389/fbioe.2023.1289299>.
- [21] V. Paplou, N.M.A. Schubert, S.J. Pyott, Age-Related Changes in the Cochlea and Vestibule: Shared Patterns and Processes, *Front. Neurosci.* 15 (2021). <https://doi.org/10.3389/fnins.2021.680856>.
- [22] A. Maniaci, L. La Via, J.R. Lechien, G. Sangiorgio, G. Iannella, G. Magliulo, A. Pace, Q. Mat, S. Lavallo, M. Lentini, Hearing Loss and Oxidative Stress: A Comprehensive Review, *Antioxidants* 13 (2024) 842. <https://doi.org/10.3390/antiox13070842>.
- [23] K. Grzybowska, A. Grzybowski, J. Knapik-Kowalczyk, K. Chmiel, K. Woyna-Orlewicz, J. Szafraniec-Szczęśny, A. Antosik-Rogóż, R. Jachowicz, K. Kowalska-Szojda, P. Lodowski, M. Paluch, Molecular Dynamics and Physical Stability of Ibuprofen in Binary Mixtures with an Acetylated Derivative of Maltose, *Mol. Pharm.* 17 (2020) 3087-3105. <https://doi.org/10.1021/acs.molpharmaceut.0c00517>.
- [24] J.D. Higgins, T.P. Gilmore, S.A. Martellucci, R.D. Bruce, H.G. Brittain, Ibuprofen, in: 2001: pp. 265-300. [https://doi.org/10.1016/S1075-6280\(01\)27008-6](https://doi.org/10.1016/S1075-6280(01)27008-6).
- [25] V. Friuli, G. Bruni, G. Musitelli, U. Conte, L. Maggi, Influence of Dissolution Media and Presence of Alcohol on the In Vitro Performance of Pharmaceutical Products Containing an Insoluble Drug, *J. Pharm. Sci.* 107 (2018) 507-511. <https://doi.org/10.1016/j.xphs.2017.06.001>.
- [26] K.D. Rainsford, Ibuprofen: pharmacology, efficacy and safety, *Inflammopharmacology* 17 (2009) 275-342. <https://doi.org/10.1007/s10787-009-0016-x>.
- [27] T. Schmid, B. Brüne, Prostanoids and Resolution of Inflammation - Beyond the Lipid-Mediator Class Switch, *Front. Immunol.* 12 (2021). <https://doi.org/10.3389/fimmu.2021.714042>.
- [28] K.E. Gilman, K.H. Limesand, The complex role of prostaglandin E₂ -EP receptor signaling in wound healing, *American Journal of Physiology-Regulatory, Integrative and Comparative Physiology* 320 (2021) R287-R296. <https://doi.org/10.1152/ajpregu.00185.2020>.
- [29] M.S. Álvarez, L. Mazzei, M.B. Hapon, I. Quesada, L. Salvarredi, D. Beltramo, C. Castro, New formulation of ibuprofen-arginate reduces oxidative stress and prevents macrophage polarization toward M1 phenotype, *Biomedicine & Pharmacotherapy* 183 (2025) 117819. <https://doi.org/10.1016/j.biopha.2025.117819>.
- [30] P.-H. Wang, Y. Wang, Y.-Y. Guo, Z.-H. Ma, C. Wu, L. Xing, Ibuprofen modulates macrophage polarization by downregulating poly (ADP-ribose) polymerase 1,

Int. Immunopharmacol. 143 (2024) 113502.
<https://doi.org/10.1016/j.intimp.2024.113502>.

5.6. SUPPORTING INFORMATION

LIST OF SUPPORTING TABLES

Table S5.1. Primer selection for qPCR analysis.

Gene type	Gene	Reverse sequence (5' - 3')	Forward sequence (5' - 3')
M1 phenotype indicator	<i>Il6</i>	AGTGGTATAGACAGGTCTGTTGG	CTGCAAGAGACTTCCATCCAG
	<i>Il1b</i>	AAACTTCTGCCTGACGAGCTT	GCACCTTACACCTACCAGAGT
M2 phenotype indicator	<i>Il10</i>	TTTTACAGGGGAGAAATCG	CCAAGCCTTATCGGAAATGA
	<i>Tgfb</i>	CTGGCGAGCCTTAGTTTGGAC	CCACCTGCAAGACCATCGAC
M1 surface marker	<i>Cd86</i>	TTGAGCCTTTGTAAATGGGCA	TGTTTCCGTGGAGACGCAAG
M2 surface marker	<i>Cd206</i>	CACTTGTTCTGGACTCAGATTA	GTGTCCTCCTGATTGTGATAG
Housekeeping gene	<i>Ubc</i>	ACCCAAGAACAAGCACAAGG	AGCCCAGTGTACCACCAAG

LIST OF SUPPORTING FIGURES

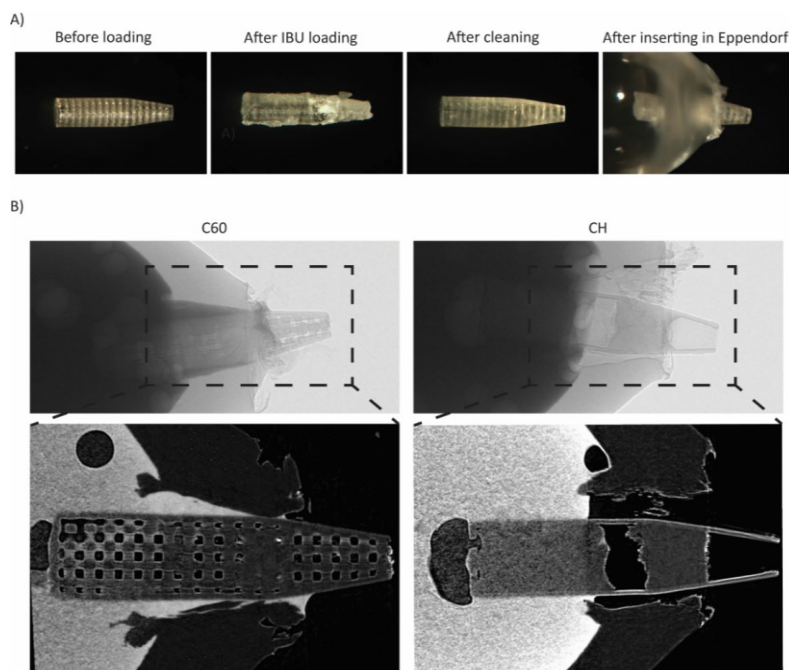


Figure S5.1. (A) Optical images of the C60 type of implant before loading, after loading, after the cleaning step, and after placement in the Eppendorf setup for drug release measurements. (B) μ -CT images of the internal and external geometry of C60 and CH at days 35 and 28 of the release measurements, respectively.

5. COCHLEAR IMPLANT DRUG LOADING AND RELEASE

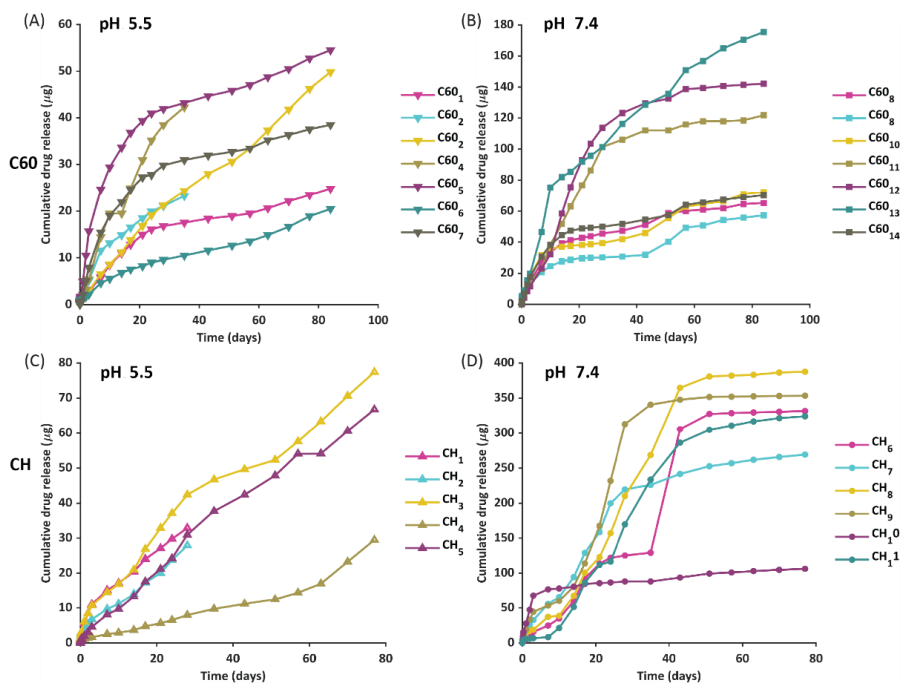


Figure S5.2. Cumulative ibuprofen release from: (A) C60 implants at pH 5.5. (B) C60 implants at pH 7.4. (C) CH implants at pH 5.5. (D) CH implants at pH 7.4.

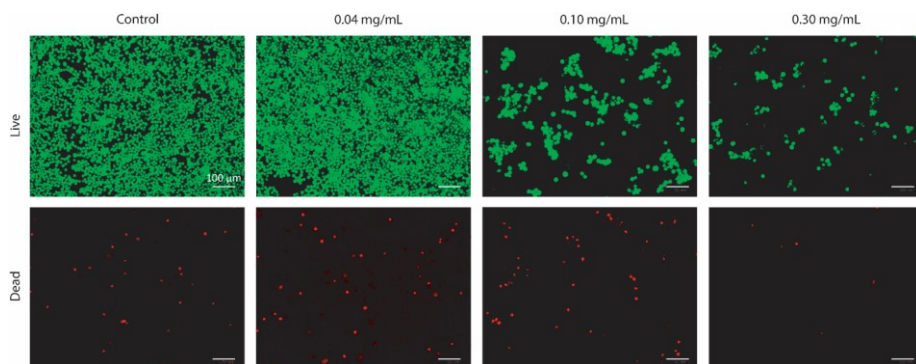
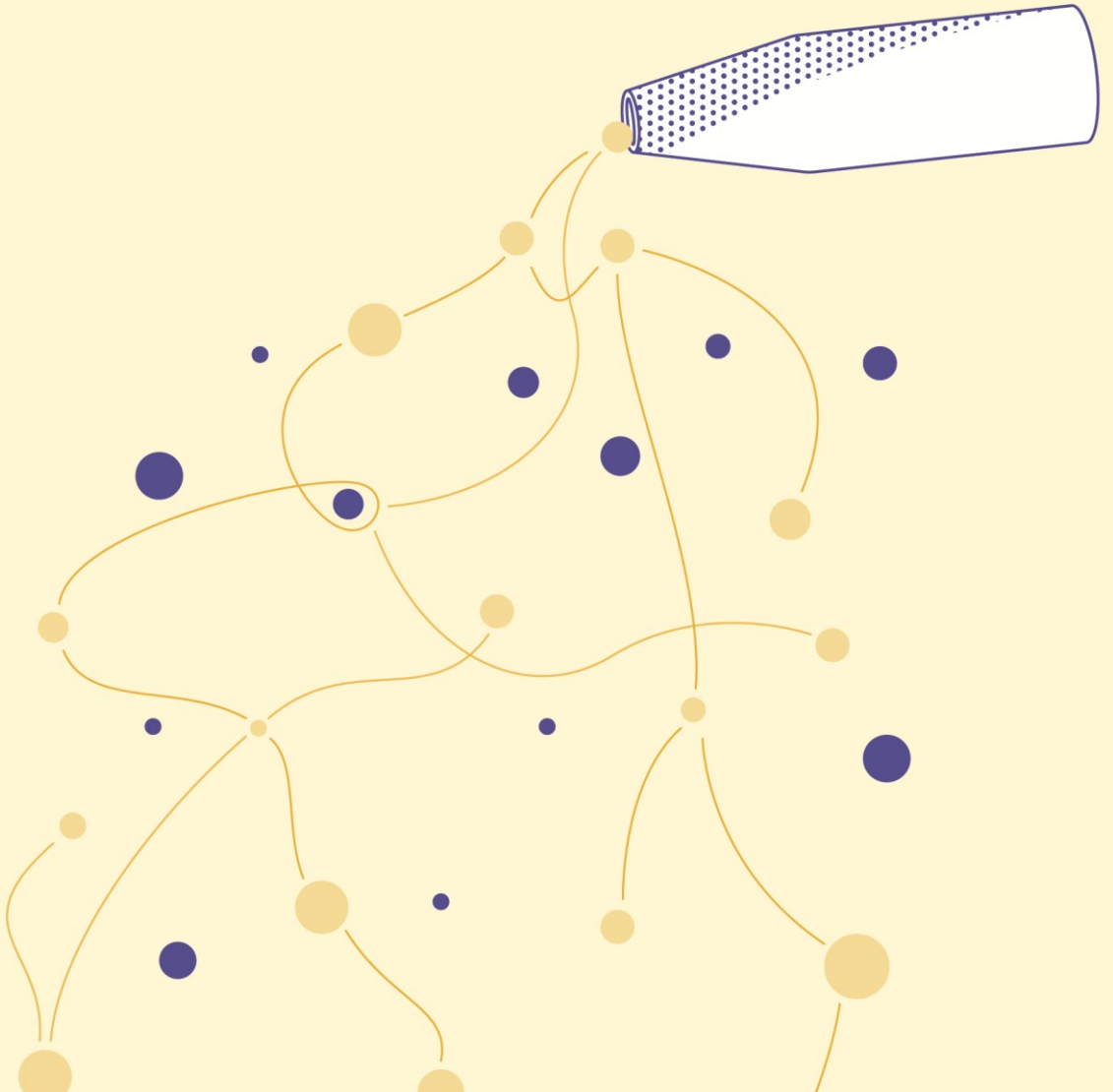


Figure S5.3. Representative Live/Dead fluorescence images of M1-stimulated macrophages after 48 h exposure to ibuprofen (0.04, 0.10, and 0.30 mg/mL). Live cells are shown in green (calcein-AM) and dead cells in red (ethidium homodimer). Scale bar: 100 μm . The experiment was performed in triplicate and repeated in three independent experiments.

Chapter 06

Concluding Remarks



6. CONCLUDING REMARKS

6.1 MAIN FINDINGS

This thesis presents the design, fabrication, and characterization of 3D-printed cochlear implants with internal microporosity as vehicles for localized drug delivery to the inner ear. The work is structured around three main pillars: (1) design and fabrication, (2) mechanical characterization through experimental and computational approaches, and (3) functional and preliminary biological evaluation. The studies in this thesis demonstrate a cohesive strategy to address the anatomical, mechanical and pharmacological challenges of cochlear drug delivery through a two-step approach that combines 3D printing of the implants and subsequent drug loading of them with a model drug.

6.2. GENERAL DISCUSSION

6.2.1. TWO-PHOTON POLYMERIZATION

Two-photon polymerization (2PP) was the primary 3D printing technology used throughout this dissertation, offering a unique combination of sub-micron resolution, design flexibility, and material selectivity [1]. The 3D printing strategies demonstrated the capacity of 2PP to fabricate anatomically relevant cochlear implants with internal porosity and microscale resolution, a combination of features that are not easily achievable with other additive manufacturing techniques. Compared to the most popular ones, such as stereolithography (SLA), fused deposition modeling (FDM), and inkjet printing, 2PP provides very high resolution and control over microscale features. While SLA was effectively used in **Chapter 4** for creating scaled-up models to validate finite element analysis (FEA) simulations, its resolution is not high enough for fabricating implant features in the 10 - 100 μm range, which is relevant for drug release in intracochlear applications. In contrast, 2PP enabled the fabrication of drug reservoirs and microporous structures with pore sizes of 20 and 60 μm . The versatility of 2PP was further underscored in **Chapter 3**, where three resins (IP-Q, IP-S, and IP-PDMS) were processed using variable parameters to fabricate both solid and porous geometries. This flexibility appeared to come at the cost of

process complexity, requiring systematic investigation in the printing parameters for each resin–geometry combination to achieve reproducibility.

6.2.2. MATERIAL PROPERTIES

Across multiple chapters of this thesis, material properties such as stiffness and surface characteristics, together with processing-related parameters influencing the degree of polymerization, were systematically investigated in relation to their relevance for cochlear-specific DDS. IP-Q was the primary material used throughout the study, as it enables the fabrication of large three-dimensional structures via 2PP and had been relatively underexplored in the literature. In contrast, the comparative evaluation of IP-S and IP-PDMS in **Chapter 3** provided additional insight into resin-specific behavior and their potential suitability for other biomedical applications.

IP-Q exhibited a combination of mechanical properties and physical properties that appear more suitable for a permanent cochlear DDS, including a high degree of polymerization, high stiffness and moderate hydrophilicity. In comparison, IP-S showed similar stiffness but is typically employed for the fabrication of smaller-scale microstructures than the cochlear implant dimensions targeted in this study. IP-PDMS, being an elastomer, exhibited higher compliance than IP-Q and IP-S. While this compliance may be advantageous for applications such as microrobotics [2,3], tissue interface devices [4], and cell-instructive biomaterials [5,6], it appears less favorable for applications requiring structural stability and precise positioning, such as cochlear DDS.

Structure–function relationships were also explored through the lens of porosity. In **Chapter 3**, introducing porosity in miniaturized implants reduced the stiffness of structures by 15–20% in IP-Q and IP-S, and by ~50% in IP-PDMS. These reductions emphasized the importance of balancing porosity for drug reservoir function with mechanical performance and underlined the effects of scaling in the 2PP process.

Interestingly, in **Chapter 4**, the simulations revealed that pore size (20 vs. 60 μm) had little influence on implant stiffness compared to the global geometry (cylindrical vs. rectangular), suggesting that macrogeometry governs implant behavior under surgical loading, while microporosity plays a more subtle, yet still relevant, role.

6.2.3. MECHANICAL TESTING CONSTRAINTS

One of the most challenging aspects in the characterization of the cochlear implant was its mechanical testing. The small size of the cochlear implants ($\sim 2.4 \times 0.6 \times 0.6 \text{ mm}^3$) ruled out the possibility of direct torsion or compression testing with standard tools. To overcome this, **Chapter 3** describes how a combination of scaled-up SLA printing, physical testing, and finite element modeling allowed us to make mechanical predictions at the microscale level based on validated macroscale results. This scaling strategy proved particularly useful in distinguishing between the mechanical performance of rectangular and cylindrical implants. Cylindrical implants showed significantly higher resistance to torsional forces, validating their suitability for surgical handling and insertion. Moreover, the mechanical simulations allowed us to analyze the impact of porosity without fabricating every variation at full resolution, thus reducing experimental burden and material usage. Such model-driven design is crucial in a field where iterative physical testing is slow, expensive, and technically constrained.

This computational-experimental workflow presents a translatable framework for future studies. As more sophisticated modeling techniques and micromechanical testing tools become available, combining them will offer even deeper insights into microscale implant mechanics and failure modes.

6

6.2.4. DRUG DELIVERY

The ultimate function of the cochlear implants developed in this work is to serve as vehicles for localized and sustained drug delivery, minimizing systemic side effects and maximizing drug bioavailability in the cochlear fluids. In **Chapter 5**, the implants were loaded with ibuprofen, a non-steroidal anti-inflammatory drug, and were tested under physiological (pH 7.4) and acidic (pH 5.5) conditions.

Hollow implants (CH) exhibited faster release rates and reached a plateau around day 40. In contrast, porous implants (C60) exhibited slower, more sustained release, continuing steadily through the 84-day test period. This outcome aligns with known principles of diffusion and surface area: hollow implants provide a shorter diffusion path and greater drug exposure, whereas porous implants modulate release through tortuosity and matrix retention. Moreover, pH-dependent differences were also

noted: acidic conditions generally slowed drug release [7]. This effect could be attributed to ibuprofen's reduced solubility at lower pH. From a therapeutic perspective, this observation is clinically relevant. Inner ear inflammation can be associated with local acidosis [8-10], meaning that implants could be tuned to respond differently under pathological conditions, introducing an avenue for passive, environment-responsive drug delivery.

Another noteworthy observation was the heterogeneous drug distribution inside implants, as revealed by μ -CT. Non-uniform loading may contribute to burst release or local depletion zones, suggesting that current loading techniques (manual injection of melted ibuprofen) need refinement or automation for consistency and scalability.

6.2.5. TOWARD A MODULAR COCHLEAR DRUG DELIVERY SYSTEM

The four chapters of this thesis converge toward the development of a microfabricated cochlear implant that is anatomically compatible, mechanically resilient, biologically safe, and functionally effective for long-term drug delivery. **Chapters 2 and 3** built the technical foundation, demonstrating that microscale implants can be reproducibly fabricated and characterized across multiple materials. **Chapter 4** introduced a predictive modeling layer that circumvents limitations in mechanical testing at small scales. **Chapter 5** validated the implants' ability to deliver drugs over time, explored environmental tuning as a functional parameter, and touched upon the anti-inflammatory and immunomodulatory effects of ibuprofen as a model drug.

Together, these components constitute a complete development process of a functional cochlear implant. The methodologies and tools developed and described are adaptable and potentially transferable to other therapeutic contexts beyond hearing loss, such as neuromodulation, chronic pain, and inner ear infections.

6.3. FUTURE OUTLOOK

The work presented in this thesis has demonstrated the feasibility of using high-resolution 3D printing to fabricate cochlear implants for localized drug delivery and has raised questions and identified additional research directions that could be

explored to achieve more precise drug delivery in the cochlea and to develop strategies for clinical translation.

6.3.1. COCHLEAR IMPLANT DESIGN AND FABRICATION

First, the 2PP printing technique offers high precision in the fabrication of implants with microscale features, but its limitations in terms of parameterization and defining the exact settings for reproducible results could be addressed in future research. As for the printing technology, 2PP enables the precise fabrication of such structures. However, with the advent of newer platforms and one-photon polymerization or SLA/DLP printing, less demanding 3D printing techniques could emerge as alternative options. Incorporating multiple materials [11] with distinct properties (e.g., biodegradable vs. non-biodegradable, hydrophilic vs. hydrophobic) may allow for spatially programmed degradation or sequential release profiles within a single implant. Recent advances in multi-resin 2PP should be explored for the next generation of drug delivery systems.

In terms of design, this work focused on improving and adjusting an existing design incorporating a container and a tip while studying the effect of a cubic-shaped internal porous network. Simplifying the outer geometry further and adding a different design of the porous networks is still open to investigation. For example, the existence of a tip and a container is creating a weight imbalance in the implant, and that can interfere with the efficiency of implantation. Moreover, the incorporation of a variety of unit designs for the internal porous structure, such as triple minimal surfaces and gradients of those, could be investigated to further extend the possibilities in delivering drugs with customized profiles.

As demonstrated in **Chapter 5**, the current manual method of filling implants with molten ibuprofen can lead to non-uniform drug distribution. Future work should explore the use of microfluidic-based injection systems or vacuum-assisted capillary loading to improve reproducibility and precision of drug distribution within microporous structures.

6.3.2. DRUG LOADING AND RELEASE

Drug loading and release were evaluated using *in vitro* experiments under controlled conditions, providing initial insight into the release kinetics of the porous, cochlea-

specific DDS. While these experiments enabled a first comparative assessment of the release trends across different porosities and highlighted the limitations of the current system, the development of a mechanistic and quantitative modeling framework would enable design optimization strategies for such DDS.

Future work should focus on implementing diffusion-based release models capable of capturing complex release mechanisms arising from variations in pore interconnectivity. Integrating experimentally derived parameters, such as porosity, diffusion coefficients, and pH-dependent drug solubility, would enable the prediction of long-term release profiles.

While ibuprofen served as a stable and well-characterized model drug in this study, extending the system to more clinically relevant and sensitive therapeutics, including corticosteroids, neurotrophins, or nucleic-acid-based agents, remains an important direction for future research. Such studies could also address drug stability during loading, storage, and release, and would benefit from complementary analytical techniques, such as nuclear magnetic resonance spectroscopy or mass spectrometry, for detailed characterization of drug integrity and release mechanisms. Ultimately, coupling experimental release data with predictive modeling would facilitate the rational design of cochlear DDS tailored to specific therapeutic agents and dosing requirements.

6.3.3. BIOLOGICAL STUDIES

The initial cytocompatibility and inflammatory response results are encouraging, but translation to clinical application requires significantly deeper biological validation, including long-term cell interaction studies. Prolonged culture of cochlear or macrophage cells in 3D environments interacting with implants would provide more representative insight into biointegration and immune cell recruitment and response over time.

Employing cochlear animal models, such as guinea pig or mouse models, would enable evaluation of tissue-scale responses, drug diffusion across cochlear compartments, and the biological effects of spatial drug gradients generated by the implant. Such *in vivo* testing would also be necessary to assess pharmacokinetics, drug bioavailability in perilymph and endolymph, implant retention, and potential effects on hearing

preservation or recovery. Furthermore, such studies would allow a more comprehensive assessment of immune responses and the long-term biological impact of implant residence.

6.3.4. CLINICAL TRANSLATION

Beyond biological and mechanical performance, clinical translation requires attention to integration within existing surgical workflows, user-friendliness, and regulatory compliance. This includes the development of implantation toolkits and delivery mechanisms. The final system must consider how the implant will be inserted and secured in the round window niche. The modularity of the system lends itself well to multi-drug loading or patient-specific customization. For instance, drug cocktails targeting inflammation, fibrosis, and oxidative stress could be incorporated to reflect individual patient pathology. Ultimately, for the implants to move toward potential clinical trials, aligning fabrication, sterilization, and validation protocols with ISO 13485, Class III medical device requirements, and GMP standards will be essential.

CONCLUDING REMARK

The findings presented in this thesis establish a proof-of-concept for 3D-printed, porous cochlear implants as vehicles for localized, sustained drug delivery. However, the path to real-world application requires multidisciplinary effort across engineering, biology, pharmacology, and clinical sciences. By expanding fabrication capabilities, modeling approaches, biological validation, and systems-level integration, future research can transform this promising technology from the benchtop of a laboratory to clinical practice in otology and potentially improve therapeutic outcomes for patients with hearing loss.

REFERENCES

- [1] H. Wang, W. Zhang, D. Ladika, H. Yu, D. Gailevičius, H. Wang, C. Pan, P.N.S. Nair, Y. Ke, T. Mori, J.Y.E. Chan, Q. Ruan, M. Farsari, M. Malinauskas, S. Juodkazis, M. Gu, J.K.W. Yang, Two-Photon Polymerization Lithography for Optics and Photonics: Fundamentals, Materials, Technologies, and Applications, *Adv Funct Mater* 33 (2023). <https://doi.org/10.1002/adfm.202214211>.
- [2] T. Stark, D. Kim, Electrode filling using capillary action of 3D printed elastomer microchannels, in: J.D. Madden, I.A. Anderson, H.R. Shea (Eds.), *Electroactive Polymer Actuators and Devices (EAPAD) XXV*, SPIE, 2023: p. 18. <https://doi.org/10.1117/12.2658146>.
- [3] G. Adam, G. Ulliac, C. Clevy, D.J. Cappelleri, 3D printed vision-based micro-force sensors for microrobotic applications, *Journal of Micro and Bio Robotics* 18 (2022) 15–24. <https://doi.org/10.1007/s12213-023-00152-x>.
- [4] Z. Zhang, B. He, Q. Han, R. He, Y. Ding, B. Han, Z.-C. Ma, Femtosecond Laser Direct Writing of Gecko-Inspired Switchable Adhesion Interfaces on a Flexible Substrate, *Micromachines (Basel)* 14 (2023) 1742. <https://doi.org/10.3390/mi14091742>.
- [5] N. Munding, M. Fladung, Y. Chen, M. Hippler, A.D. Ho, M. Wegener, M. Bastmeyer, M. Tanaka, Bio-Metamaterials for Mechano-Regulation of Mesenchymal Stem Cells, *Adv Funct Mater* 34 (2024). <https://doi.org/10.1002/adfm.202301133>.
- [6] A. Sharaf, J.P. Frimat, G.J. Kremers, A. Accardo, Suppression of auto-fluorescence from high-resolution 3D polymeric architectures fabricated via two-photon polymerization for cell biology applications, *Micro and Nano Engineering* 19 (2023) 100188. <https://doi.org/10.1016/j.mne.2023.100188>.
- [7] S. Oh, W.S. Shin, H.T. Kim, Effects of pH, dissolved organic matter, and salinity on ibuprofen sorption on sediment, *Environmental Science and Pollution Research* 23 (2016) 22882–22889. <https://doi.org/10.1007/s11356-016-7503-6>.
- [8] P. Bazard, J. Pinerós, R.D. Frisina, M.A. Bauer, A.A. Acosta, L.R. Paganella, D. Borakiewicz, M. Thivierge, F.L. Mannering, X. Zhu, B. Ding, Cochlear Inflammation in Relation to Ion Channels and Mitochondrial Functions, *Cells* 10 (2021) 2761. <https://doi.org/10.3390/cells10102761>.
- [9] Z. Su, Y. Chen, Y. Liu, J. Cao, J. Cui, H. Chen, Q. Li, Oxidative stress and inflammation combine to exacerbate cochlear damage and sensorineural hearing loss in C57BL/6 mice, *Front Neurosci* 19 (2025). <https://doi.org/10.3389/fnins.2025.1563428>.
- [10] V. Fuentes-Santamaría, J.C. Alvarado, S. Mellado, P. Melgar-Rojas, M.C. Gabaldón-Ull, J.J. Cabanes-Sanchis, J.M. Juiz, Age-Related Inflammation and

Oxidative Stress in the Cochlea Are Exacerbated by Long-Term, Short-Duration Noise Stimulation, *Front Aging Neurosci* 14 (2022). <https://doi.org/10.3389/fnagi.2022.853320>.

- [11] L. Yang, F. Mayer, U.H.F. Bunz, E. Blasco, M. Wegener, Multi-material multi-photon 3D laser micro- and nanoprinting, *Light: Advanced Manufacturing* 2 (2021) 1. <https://doi.org/10.37188/lam.2021.017>.

ACKNOWLEDGEMENTS

On the 20th of April 2017, a warm spring afternoon in my hometown, I was preparing my afternoon coffee when I heard the familiar chime of an email notification on my phone. It was the admission letter to the 2-year Biomedical Engineering MSc programme. I couldn't believe my *freaking* luck to finally be able to do the very thing I had been dreaming of since the beginning of my engineering studies. Up to that day, I was a Production & Management Engineer, and I could not picture myself in that field for the rest of my life. The thought of moving into Biomedical Engineering filled me with indescribable joy. My **Mum** was happy too (and a little sad), but mostly, she was excited for me and sharing in my anticipation. The rest of my **family** felt the same, a mixture of happiness and sadness. In Greek, there is a word for this feeling: *χαρμολύπη*, a bittersweetness that holds both pride and longing. For me, however, there was no bittersweetness, only pure, unrestrained excitement.

Almost three years after that life-changing moment, and having completed my MSc, **Lidy Fratila-Apachitei** asked me whether I would like to begin this very PhD. I am deeply grateful to her for believing in me and giving me this opportunity. The book you are holding in your hands is the culmination of a series of fortunate and less fortunate events, all of which (re)shaped not only the research within, but also my personality. The following pages are dedicated to all the people who, whether they intended to or not, contributed in some way to this journey. So, maybe some of the following lines bring tears to your eyes, maybe they bring a smile upon your face or you just browse quickly through to find your name and read your line, and maybe you do not find your name and you are all upset. Is all part of life!

Lidy, I have great appreciation for your consistent support, insightful feedback, challenging comments, thoughtful advice, and your almost nerve-wrecking attention to detail and storytelling. I have wrestled with some of these aspects at times, but they have kept me moving forward, pushing me to think differently, to think deeper, and to grow. Sincerely, thank you.

I would also like to express my gratitude to my promotor, **Amir Zadpoor**, for your ability to keep things running while always asking the right question; one that could shift my perspective and open new ways of thinking. Your encouragement has left a mark on my development as a researcher.

To **Iulian Apachitei**, I owe deep thanks for your calm yet steady presence, your practical wisdom, patience, and reliability. Thank you for being there during my setbacks, for the long conversations that often drifted into the analysis of historical events, and for your consistent reminder that "*it is going to be alright*".

I am deeply thankful to **Sander Leeftang** and **Maria Klimopoulou**, the most fashionable laboratory duo. Without you, my PhD would have been practically

impossible. Thank you for the countless hours spent next to me in the lab, imaging, pipetting, or troubleshooting. I am truly happy not only for having worked alongside you, but for having learned to ride platform truck carts and for never coming to the laboratory underdressed or without skincare.

I owe a big part of this trajectory to **Yanis Bedhulo van Lages**, for his unwavering support and friendship throughout this journey. None of this would have been possible without the invaluable aid of **Florence Siepmann** and **Juergen Siepmann**. Thank you for the opportunity to work in your laboratory and to spend a month in the beautiful city of Lille and to experience such a stimulating research environment. A warm thank you also goes to **Nina, Liseanne, Charline, Fabiana, and Jeremy**, for your hospitality, kindness, help, and the many moments that made my time in Lille memorable. Some of my days after coming back from Lille to Delft I was missing the routine of passing by the bakery to bring pastries for the office and to get coffee in exchange ☺.

I am also very grateful to **Prince Bawuah** and **Axel Zeitel**, for the smooth collaboration and the discussions we shared during the project. Your positivity have made even the most challenging of the times enjoyable. Thank you for your openness, insights and humor.

To my *pulchritudinous* fish **Mauricio, Pier, Chung-Fen, Jonathan, Judith, Ylenia, Linda, and Bogdan**, thank you for always being a safety net. For the hours we spent dissecting the “meaning of a PhD”, for the COVID times that remained unforgettable because of you and for constantly reminding me to become a better scientist to deserve a place in the same office with you.

To the youngest generation of fish, that fit so well into the Fishtank-way of doing research, **Giannis, Jamie, Nianlei, Janne, Koen, Matthew, and Vikash**, you brought laughter and more sugar highs in the office.

To the *Italian* crew, **Ludovica, Sara, Beatrice, Federica, Giacomo, Alessia, Sara, Gabrielle** and **Viola**, and to the *almost-Italian* crew, **Kasra, Rogier, Daniel, Gavin, and Konstantinos**, thank you for all the vibrant lunch breaks, beers, and spontaneous chats. Whether we were discussing science, life, or what to cook for dinner, you brought a sense of joy and chaos that made everything better.

Hey, *Captains of the CaribBME*, **Jette** and **Suzanne!** Thank you for being part of my very first collaborative project during the PhD which turned out to be an absolute blast! Our sailing trip to the IJsselmeer remains for me one of the best memories of this PhD journey.

The lab wouldn't have been the same without **Khashayar, Monika, Lennart, Jelle, Indra, Jinlai, Dirk, Lorenzo, Sahar, and Vicky**. From figuring things out together, learning new techniques (sometimes the hard way), sharing the occasional

ACKNOWLEDGEMENTS

frustration but also first-time successes, you have been a very essential part of my growth.

Vahid, Mahya, and Roos, I'm truly grateful for your enormous contributions to my research and, by extension, to this book. This thesis would not have been the same without the many hours you spent working alongside me and your shared curiosity throughout.

To the BME secretaries, **Amanda, Marjolijn, and Angelique**, thank you for handling all the bureaucracy that came my way with a smile and the necessary amount of sarcasm.

To **Kirsten, Constanza, Vera, Karin, Edwin, Christoph, Benjamin, Karien, Anton, Hassan, Jenna, Jonathan, Nynke, Guiomar, Nasim, Pascal, Jules, and Martijn**, thank you for the sports days, lunches, walks, coffees, ice-skating, participating in experiments and discussing local and international politics and habits.

To my glorious paranymphs **Pier** and **Niko**, who are like the two sides of the same coin. I could not have reached this moment without the wonderfully contradictory aspects of your characters. I needed both the calmness and the excitement, the stoicity and the impulsivity, the wisdom and the stupidity. You standing beside me at the finish line means more than I can describe.

Momo, thank you that you took your role seriously and dragged me to the gym when I needed it most. Off to more training sessions together!

To the Nanoscribe crew **Ahmed, Pieter** and **Ebrahim**, I owe you the hours of ranting and support over printing issues, which were always dealt with such graceful frustration. In the end, if it weren't for you all, I wouldn't have learned how to navigate that 3D printing monster or come to actually enjoy the process.

Samantha, you are an incredibly talented graphic designer and without you this beautiful book and presentation would not have been possible. You've been one of the most silent and powerful supporters and I'm deeply grateful for everything you've done behind the scenes to bring this vision to life.

To the Works Council members, **Nanette, Marianne, Diana, Herman Arjan, Olaf, Roy, Cornel, Eveline, Winke, Koen, Marion, Robert, Ronald, Maaïke, Stephan, Claudia, Erna, Ivan, Erwin** and **Minke** and to the first-time members of the Young Researcher's Impact: **Stephanie, Wo, Rebekka, Bob** and **Jiwon** thank you for reminding me that impact goes beyond research. It was a privilege to work with you and to contribute to initiatives that assist the people behind education and research. Your commitment to the needs of employees and students, beyond performance standards, made a deep impression on me. A special and heartfelt mention goes to our Works Council member **Marc**, who is no longer with us. You

ACKNOWLEDGEMENTS

deserved to celebrate your promotion and if I could, I would trade a piece of my own just to have you around.

To the *dutch-speaking* crew, **Elisabeth, Franziska** and **Bert**, thank you for creating a safe space for me to dare speak Dutch. I'm definitely more confident in that because of you even if it is still broken 😊.

To the random nights simply hanging out and to the weird but wonderful "brotherhood" that formed with **Rosa, Kostas, Kevin, Mike, Margarita, Leonard, Renato, Micah, Gabriel**, and **Alexandra**. I love our spontaneous conversations and the chaotic energy all over.

To the friendships of adulthood with **Anastasis, Ilias, Vasilis** and **Nikos**. From the first days of our Master's to today, your jokes, teasing, and solid support that helped carry me through. I hope this never ends. Cheers!

Annie, Georgia, and Kalypso, thank you for being there through the frantic thesis writing, the trip planning, the last-minute girls' nights and lazy brunches, the dog walks and the deep talks.

Qais and **Damla**, thank you for our culinary adventures, our endless gossiping, and our belly laughs. Our trio kept joy on the menu, no matter the circumstances, and we faced a couple tough ones ♣.

Mauro, thank you for your presence during a significant part of this PhD, and for the shared moments and deep discussions.

Aggelina and **Elli**, you have been my emotional home base, the people to share and discuss absolutely anything and everything and achieving laughs and cries, often in the same sentence. You deserve nothing but the best!

Maria and **Ioanna**, I feel honored you still choose to travel to meet up, that you care for me from the bottom of your hearts and that meeting each other in Xanthi was only the beginning of our life experiences together.

To my *dutch* family **Stavroula, Dimitris, Nikos, Tanja, Sakis, Soula, Joost, Aldona, Marilena, Alexandra, Elvita, Valentijn, Heleentje**, and **Dimis**, I owe the smoothest transition I could have imagined to life in a foreign country. You made the Netherlands feel like home.

To my little brothers...in crime, **Periklis and Lefteris**, I have nothing more to say other than I love you. You are the sweetest boys on earth ♥.

Any attempt to thank you, **Mum** and **Dad**, feels incomplete. I think the best way to tell you is by being happy and content with my life. To live fully, work hard, and feel proud of my own path. So, now, a small part of this long journey ends and I owe it to you too. Because I lived it fully, I worked hard for it and I definitely feel proud of it. Let's enjoy this together!

Katerina Isaakidou, Delft 2026

CURRICULUM VITAE

Aikaterini Isaakidou, born 12-08-1992 in Kavala, Greece

Employment

- | | |
|-----------------------|--|
| Oct. 2025 - present | Postdoctoral researcher
Biomechanical Engineering, TU Delft, Delft |
| Feb. 2020 - Sep. 2024 | PhD researcher
Biomechanical Engineering, TU Delft, Delft |
| Feb. 2019 - Aug. 2019 | Clinical researcher
Dental Robotics, Delft |
| Sep. 2018 - Dec. 2018 | Innovation & science intern
CAM Bioceramics B.V. |

Education

- | | |
|-----------------------|---|
| Sep. 2017 - Dec. 2019 | Master Biomedical Engineering
Faculty of Mechanical Engineering, TU Delft, Delft |
| Sep. 2010 - Jul. 2017 | Integrated Bachelor & Master Production Management & Engineering
School of Engineering, Democritus University of Thrace, Xanthi |

LIST OF PUBLICATIONS

Publications part of this thesis

Isaakidou A.*, Bedulho Das Lages Y.*, Bawuah P., Moosabeiki V., Verin J., Willart J.F., Klimopoulou M., Leeflang M.A., Mirzaali M.J., Zeitler A., Siepmann F., Apachitei I., Siepmann J., Fratila-Apachitei L.E. and Zadpoor A.A. Sustained drug release from 3D-printed microporous human cochlear implants fabricated by two-photon polymerization. Submitted for publication. *Both authors contributed equally.

Isaakidou A.*, Ganjian M.*, Moosabeiki V., Leeflang M.A., Goushki M.N., Boukany P.E., Wątroba M., Groetsch A., Schwiedrzik J., Mirzaali M.J., Apachitei I., Fratila-Apachitei L.E. and Zadpoor A.A. Advanced Engineering Materials. 2025. 000: e202500977. <https://doi.org/10.1002/adem.202500977>. *Both authors contributed equally.

Isaakidou A.*, Ganjian M.*, van Hoften R., Saldívar M.C., Leeflang M.A., Groetsch A., Wątroba M., Schwiedrzik J., Mirzaali M.J., Apachitei I., Fratila-Apachitei L.E. and Zadpoor A.A. Multi-scale *in silico* and *ex silico* mechanics of 3D printed cochlear implants for local drug delivery. Frontiers in Bioengineering Biotechnology. 2024. 11:1289299. <https://doi.org/10.3389/fbioe.2023.1289299>. *Both authors contributed equally.

Isaakidou A., Apachitei I., Fratila-Apachitei L.E. and Zadpoor A.A. High-precision 3D printing of microporous cochlear implants for personalized local drug delivery. Journal of Functional Biomaterials 2023. 14(10): 494. [10.3390/jfb14100494](https://doi.org/10.3390/jfb14100494)

Other publications

Li J., **Isaakidou A.**, van Zanten L.J., Tas R.P., Mirzaali M.J., Fratila-Apachitei L.E., Zadpoor A.A. (2025). Multi-scale additive manufacturing of 3D porous networks integrated with hydrogel for sustained *in vitro* tissue growth. Acta Biomaterialia. 196: 198-212. <https://doi.org/10.1016/j.actbio.2025.03.005>

Saldívar M.C., Tay E., **Isaakidou A.**, Moosabeiki V., Fratila-Apachitei L.E., Doubrovski E.L., Mirzaali M.J., Zadpoor A.A. (2023). Bioinspired rational design of bi-material 3D printed soft-hard interfaces. Nature Communications. 14: 7919. [10.1038/s41467-023-43422-9](https://doi.org/10.1038/s41467-023-43422-9)

Nouri-Goushki M.*, **Isaakidou A.***, Eijkel B.I.M., Minneboo M., Liu Q., Boukany P.E., Mirzaali M.J., Fratila-Apachitei L.E., Zadpoor A.A. (2021). 3D printed submicron patterns orchestrate the response of macrophages. Nanoscale. 13: 14304-14315. [10.1039/D1NR01557E](https://doi.org/10.1039/D1NR01557E). *Both authors contributed equally.

